A selective RIPK1 PROTAC degrader suppresses inflammation and achieves potent anti-tumor activity

Jonathan Mannion[1,11], Valentina Gifford[1,11], Benjamin Bellenie[2,11], Winnie Fernando[1,11,], Laura Ramos Garcia[1], Rebecca Wilson[1], Sidonie Wicky John[1], Savita Udainiya[1], Emmanuel C. Patin[3], Crescens Tiu[1], Angel Smith[1], Maria Goicoechea[1], Andrew Craxton[4], Nathalia Moraes de Vasconcelos[1], Naomi Guppy[1], Kwai-Ming J Cheung[2], Nicholas J. Cundy[2], Olivier Pierrat[2], Alfie Brennan[2], Theodoros I. Roumeliotis[5], Graeme Benstead-Hume[5], John Alexander[1], Gareth Muirhead[1], Scott Layzell[6], Wenxin Lyu[7], Victoria Roulstone[3], Mark Allen[8], Holly Baldock[8], Arnaud Legrand[1], Florian Gabel[2], Natalia Serrano-Aparicio[2], Chris Starling[1], Hongyan Guo[9], Jason Upton[10], Mads Gyrd-Hansen[7], Marion MacFarlane[4], Benedict Seddon[6], Florence Raynaud[2], Ioannis Roxanis[1], Kevin Harrington[3], Syed Haider[1], Jyoti S. Choudhary[5], Swen Hoelder[2], Tencho Tenev[1*] and Pascal Meier[1,12*]

[1]The Breast Cancer Now Toby Robins Research Centre, The Institute of Cancer Research, Fulham Road, London, SW3 6JB, UK.
[2]Centre for Cancer Drug Discovery at the Institute of Cancer Research, London, SM2 5NG, UK.
[3]Division of Radiotherapy and Imaging, The Institute of Cancer Research, London, SW3 6JB, UK.
[4]MRC Toxicology Unit, University of Cambridge, Gleeson Building, Tennis Court Road, Cambridge, CB2 1QR
[5]Functional Proteomics Group, The Institute of Cancer Research, London, SW3 6JB, UK.
[6]Institute of Immunity and Transplantation, The Pears Building, University College London, London, NW3 2PP, UK.
[7]Department of Immunology and Microbiology, LEO Foundation Skin Immunology Research Center, University of Copenhagen, Copenhagen, Denmark
[8]Biological Services Unit, The Institute of Cancer Research, London, SW3 6JB, UK.
[9]Department of Microbiology and Immunology, LSU Health Shreveport, LA, USA.
[10]Department of Biological Sciences, Auburn University, Auburn, AL, USA.
[11]These authors contributed equally.
[12]Lead contact.

***Correspondence**: Tencho Tenev (Tencho.Tenev@icr.ac.uk) and Pascal Meier (pmeier@icr.ac.uk)

Key words: RIPK1, cell death, necroptosis, inflammation

ABSTRACT

Receptor Interacting Protein Kinase 1 (RIPK1) acts as a key mediator of inflammation and cell death. However, dysregulated RIPK1 signaling can lead to excessive tissue damage and contribute to the development and progression of inflammatory diseases. Moreover, cancer cells can exploit RIPK1's scaffolding function to evade cell death and immunity. Therefore, targeting RIPK1 via PROTAC-mediated protein degradation may limit RIPK1-dependent pathologies and sensitize cancer cells to anti-cancer therapies. Here we describe a RIPK1-specific PROTAC degrader, specifically targeting murine and human RIPK1, that boosts anti-tumor therapy. Acute depletion of RIPK1 deregulates innate immune signaling and concurrent activation of RIPK3-mediated necroptosis. We further demonstrate that RIPK1 degradation enhances the immunostimulatory effects of radio- and immunotherapy, in-turn boosting anti-tumor immunity and response to therapy. Additionally, PROTAC-mediated depletion of RIPK1 suppresses RIPK1-driven skin disease. Therefore, targeting RIPK1 with PROTACs offers a novel strategy to enhance anti-cancer therapies and alleviate RIPK1-driven pathologies.

Highlights

- RIPK1's scaffolding function protects cancer cells from immune detection and death
- RIPK1-specific PROTAC degraders enhance innate immune signalling and necroptosis
- RIPK1 PROTACs boost the immunostimulatory and anti-tumour effects of RT and ICB
- PROTAC-mediated RIPK1 depletion suppresses skin inflammation

eTOC blurb

Tumour cells frequently hijack RIPK1's scaffolding function to resist cell death and avoid immune detection. Mannion et al. describe the development of a RIPK1-selective PROTAC degrader that boosts the immunostimulatory and anti-tumour activity of radiotherapy (RT) and immune checkpoint blockade (ICB), heating up tumours and driving long-lasting anti-tumour immunity.

INTRODUCTION

Cell death and inflammation are closely linked arms of the innate immune response to combat infection and drive anti-tumor responses. While the ability to sense danger is central to any organism's strategy for maintaining tissue function[1], uncontrolled or excessive inflammatory responses can cause tissue damage and contribute to the pathogenesis of chronic inflammatory diseases, including psoriasis, neurodegenerative diseases, inflammatory bowel disease and asthma[2]. Further, tumor cells frequently evade immune detection and elimination by suppressing innate immune responses[3]. Advancements in our understanding of the intricate signals originating from dying cells suggest that cell death serves as more than just an endpoint. It facilitates the exchange of information between the dying cell and cells of the tissue micro-environment, particularly immune cells, alerting and recruiting them to the site of disturbance. Receptor-interacting serine/threonine-protein kinase 1 (RIPK1) is emerging as a critical stress sentinel that functions as a molecular switch, governing cellular survival, inflammatory responses and immunogenic cell death signaling. Its tight regulation involves multiple layers of post-translational modifications [4]. Located downstream of many cytokine receptors and pattern recognition receptors (PRRs), RIPK1 plays a crucial role in determining the outcome between pro-survival NF-κB signaling and cell death[5-8]. RIPK1 can positively and negatively regulate cell death, innate immunity, and inflammation [9,10]. While the catalytic function of RIPK1 is required to trigger cell death, the non-catalytic scaffold function of RIPK1 is essential to regulate pro-inflammatory and pro-survival signaling[11-17]. Accordingly, controlled activation of RIPK1 contributes to tissue repair and immune surveillance. However, when deregulated, through mutations in RIPK1 itself or as a consequence of mutations in genes encoding proteins that negatively regulate RIPK1, such as *TBK1, A20* (also known as *TNFAIP3*), *ABIN1* (also known as *TNIP1*), *NEMO, OTULIN* and members of the *LUBAC* complex, over-exuberant activation of RIPK1 can lead to many immune and autoinflammatory diseases[18-23]. Consistently, targeting RIPK1 kinase activity suppresses the pathology induced by loss of A20 in a mouse model of arthritis[21,22] and inflammatory bowel disease (IBD)[24]. Similarly, deletion of *Nemo* in intestinal epithelial cells causes colitis because of chronic activation of RIPK1. Again, deregulated RIPK1 kinase-mediated cell death is likely the underlying mechanism causing inflammatory disease[20]. Thus, deregulation of RIPK1 is a common feature in chronic inflammatory disease[4,8,25]. Hence, RIPK1 has emerged as a promising therapeutic target[25].

While chronic, deregulated activation of RIPK1 is associated with inflammatory disease[4,8,25], data demonstrate that cancer cells often hijack RIPK1 to promote cell survival, insensitivity to TNF and resistance to immunotherapy[26]. This is because the scaffolding function of RIPK1 drives NF-κB signaling and NF-κB-dependent induction of pro-survival gene products (e.g. Bcl2, Bcl-xL, IAPs and cFLIP)[27,28]. Further, chronic NF-κB signaling by RIPK1 can contribute to the production of an immunosuppressive chemokine program, ultimately resulting in decreased infiltration of $CD8^+$ T cells and NK cells, reducing local TNF super family (TNFSF) ligands (TNF, TRAIL and FasL) and profound ICB resistance[26,29,30]. Additionally, RIPK1's scaffold function can also trigger sub-lethal activation of caspase-8, which in turn cleaves and inactivates RIPK3, CYLD and RIPK1 itself, effectively blocking necroptosis[31-34].

Given that RIPK1 suppresses necroptosis signaling in response to activation of TLR3/4 and ZBP1[11,12,14-17,25,32,35-45], targeting RIPK1 has the potential to overcome apoptosis-resistance and trigger more immunogenic forms of cell death[7,46,47]. At present, most anti-cancer drugs kill cancer cells *via* caspase-mediated apoptosis, which is generally immunologically silent. Necroptosis is a caspase-independent, lytic form of cell death that is often linked to pathogen infection[48,49] and, therefore, is potent in initiating strong immune responses[2,50]. It is thought that the core origin of necroptosis' immunogenicity comes from the ability of death receptors or PRR to activate NF-κB and/or interferon signaling while the cell is dying by necroptosis [46,47,50-53]. Both interferon signaling and NF-κB activation, ultimately drive the production of inducible DAMPs that act as potent danger signals to the immune system[54], ensuring that the antigen-presenting dendritic cells not only take up dead cells to sample cancer epitopes but also become activated simultaneously to promote $CD8^+$ T cell cross-priming[5]. Therefore, developing therapies that drive necroptosis could not only kill tumor cells directly but also ultimately (re)activate the immune system of a patient to target cancer cells.

Although RIPK1 has emerged as a therapeutic target, its disease-associated activity cannot easily be neutralized by kinase inhibitors alone[26]. Therefore, alternative strategies, such as the use of PROTAC (proteolysis-targeting chimera) degraders, that can specifically target RIPK1's scaffolding function, may be more effective in treating RIPK1-driven disease. To improve RIPK1 targeting, we generated a series of bifunctional PROTAC molecules. We found that these pharmacological compounds degrade RIPK1

at nanomolar concentrations in human and mouse. We found that acute depletion of RIPK1 primes TNFR1- and TLR3/4-signaling hubs to 'overheat', driving accentuated activation of NF-κB, MAPK, and IFN signaling. While acute deletion of RIPK1 resulted in enhanced NF-κB, MAPK, and interferon signaling, it also simultaneously deregulated RIPK3 activation and necroptosis, in a cell and tissue-type dependent manner. We demonstrate that RIPK1-PROTAC degraders synergized with immunostimulatory therapies, such as radiotherapy (RT) and immune checkpoint blockade (ICB), in a mouse model of triple-negative breast cancer. Mechanistically, we found that depletion of RIPK1 sensitized cancer cells to RT-induced TNF and interferons, in turn promoting immunogenic cell death (necroptosis) to 'heat up' tumors and drive long-lasting anti-tumor immunity. Moreover, acute depletion of RIPK1 in the skin protects animals from RIPK1-driven cell death and skin inflammation. Consequently, targeting RIPK1 by PROTACs emerges as a promising approach to alleviate RIPK1-driven pathologies.

RESULTS

A RIPK1 PROTAC achieves selective and potent degradation of RIPK1

Although RIPK1 is a major therapeutic target, its disease-associated activity cannot easily be neutralized by kinase inhibitors alone[26]. Moreover, while RIPK1 kinase inhibitors are highly effective in mice[11-17], we found that the selective RIPK1 kinase inhibitors PK68 (IC50 of ~22 nM)[55] and GSK'963 (IC50 of ~29 nM)[56] only partially suppressed RIPK1-induced cell death in human cells as they were less effective to block RIPK1-induced apoptosis (**Suppl. Fig. S1A,B**), yet efficiently blocked necroptosis (**Suppl. Fig. S1C**). To improve RIPK1 targeting, we explored a proteolysis-targeting chimera (PROTAC) approach[57]. To this end, we generated a series of bifunctional small molecules composed of a RIPK1-binding warhead, a linker and a ligand for the von Hippel-Lindau (VHL) E3 ligase (**Fig. 1A and Suppl. Fig. S1D**). We used the cell-active RIPK1 kinase inhibitor PK68 as a RIPK1-binding entity[55], which was fused to a VHL ligand[58] via linkers of various lengths. Treatment with these RIPK1 PROTACs showed a dose dependent decrease in RIPK1 levels in a panel of human and murine cell lines and primary cells (**Fig. 1B-E** and **Suppl. Fig. S1E-J)**. The RIPK1-PROTAC with a 10-atom linker, subsequently referred to as R1-ICR-5, was consistently the most efficient among these RIPK1 degraders, depleting RIPK1 at nanomolar range in human and murine cells. RIPK1 degradation by R1-ICR-5 was VHL-mediated as the control compound R1-ICR-5S, which has inverted stereochemistry at the proline 4-position that precludes VHL binding[59], failed to deplete RIPK1 levels in a similar manner (**Fig. 1F**). Moreover,

treatment with the parent RIPK1 ligand PK68 alone had no effect on RIPK1 protein levels (**Suppl. Fig. S1E,F**). Together, these data suggest that the ability of the R1-ICR-5 compound to bring RIPK1 and VHL into proximity is critical for the observed efficacy.

At concentrations at which the active RIPK1 PROTACs reduced RIPK1 levels, we noticed no apparent changes in protein levels of related kinases, such as RIPK2, RIPK3, BRAF and TrkA, a potential 'off target' binder of PK68 (**Fig. 1G and Suppl. Fig. S2A-E**)[55]. Co-treatment with PK68 effectively competed with the RIPK1 PROTAC and suppressed degradation of RIPK1 (**Suppl. Fig. S2F,G**). R1-ICR-5-mediated degradation of RIPK1 was observed as early as 2 hrs after treatment and was nearly complete at 6 hrs (**Fig. 1G**). Whole proteome analysis demonstrated that only RIPK1 was significantly degraded by the RIPK1 PROTACs in BMDMs and U937 following 5 hours treatment **(Fig. 1H, Suppl. Fig. S2H)**. Other kinases were not degraded under these conditions, corroborating the specificity and selectivity of PROTAC-mediated targeting of RIPK1. By pre-treating cells with a VHL or proteasome inhibitor (bortezomib), we confirmed the requirement for VHL-binding and proteasomal dependence of the degradation **(Fig. 1G, Suppl. Fig. S2A-G)**. Washout experiments indicated that RIPK1 has a low re-synthesis rate, taking more than 72 hrs to reach pre-treatment levels (**Fig. 1I and Suppl. Fig. S2I**). Although R1-ICR-5's lipophilicity is currently unfavorable for systemic treatments in animals, local administration of R1-ICR-5 was effective in depleting RIPK1 levels *in vivo* (**Suppl. Fig. S2J**). As such, we have developed and characterized a RIPK1 PROTAC, R1-ICR-5, that enables the acute and specific degradation of RIPK1 in both human and mouse.

RIPK1 degraders deregulate innate immune signaling

Next, we evaluated whether acute depletion of RIPK1 compromised TNF or TLR3 signaling[60,61]. Unexpectedly, we found that treatment with R1-ICR-5 deregulated the response to TNF stimulation in primary BMDMs, as well as in triple negative breast cancer (TNBC) EO771 cells, enhancing TNF-induced expression of chemokines and cytokines compared to control treatment (**Fig. 2A-C and Suppl. Fig. S3A-C**). Most notable among the affected genes upon TNF stimulation were *Tnf*, *Il-6* and *A20 (Tnfaip3)*. While acute loss of RIPK1 accentuated NF-κB signaling in response to TNF, we noticed that mere depletion of RIPK1 in resting BMDMs induced the production of *Tnf*, *A20* and *Sod2* (**Fig. 2C and Suppl. Fig. S3C**). R1-ICR-5-mediated production of TNF was dependent on MK2-mediated production

of autocrine TNF and subsequent TNF-mediated innate immune signaling (**Fig. 2D**). Consistent with deregulation of TNF signaling, we noticed enhanced recruitment of the E3 adaptor TRADD to TNFR1 when RIPK1 was depleted (**Fig. 2D** and **Suppl. Fig. S3D**), likely due to the competitive dynamics for TNFR1 binding between TRADD and RIPK1[62]. Enhanced recruitment of TRADD was accompanied with accentuated ubiquitylation of TRADD, TRAF2, cIAP1 and HOIP (**Fig. 2E**). Since ubiquitylation of components of complex I mediates NF-κB activation, it is likely that enhanced ubiquitylation of complex I results in deregulated TNF signaling in BMDMs, L929, EO771 and human LIM1215 and HT29 cells (**Fig. 2F** and **Suppl. Fig. S3B,C,E,F,G**). Concordantly, we observed deregulated activation of MAPK and NF-κB signaling following acute depletion of RIPK1.

PROTAC-mediated depletion of RIPK1 also caused deregulated TLR3 signaling, leading to enhanced induction of *Il-6*, *Tnf*, *Ccl2*, *Cxcl9*, *Cxcl10* and *Ifnβ* in BMDMs and EO771 TNBC cells (**Fig. 2G and Suppl. Fig. S3H,I**). Deregulated innate immune signaling in response to R1-ICR-5 was not due to an off-target effect as genetic acute removal of RIPK1, using BMDMs$^{LysM\text{-}Cre;Ripk1fl/fl}$ cells, also exhibited accentuated innate immune signaling (NF-κB and interferon) in response to TLR3 stimulation (**Suppl. Fig. S3J**). Moreover, while R1-ICR-5 caused accentuated innate immune signaling in WT EO771 cells, no such effect was seen in EO771 *Ripk1*-KO cells, in which RIPK1 was deleted long-term (**Suppl. Table. S1 and S2**). These data suggest that RIPK1 is required for fine-tuned activation of TNF and TLR3 signaling, preventing hyper-activation of these pathways.

RIPK1 PROTACs facilitate non-canonical activation of RIPK3 by TNFR1 and TLR3/4

Acute depletion of RIPK1 not only caused deregulated TNF-signaling, but also sensitized cells to cell death, which was accompanied by enhanced phosphorylation and activation of RIPK3 and MLKL (**Fig. 3A-C**). Likewise, acute depletion of RIPK1 also caused enhanced TLR3- and TLR4-induced necroptosis that was mediated by TRIF (Also known as *Ticam1*), independent of TNFR1 and ZBP1 (**Fig. 3D,E and Suppl. Fig. S3K,L**). TLR3- and TLR4-mediated necroptosis also required the contribution of IFNAR1, as IFNAR1 deficiency suppressed this death (**Suppl. Fig. S3K,L**). Thus, our data suggest that acute depletion of RIPK1, not only causes hyper-activation of innate immune signaling pathways (e.g. TNFR1 and TLR3), but also triggers unhindered activation of cell death.

Next, we evaluated the selectivity and specificity of R1-ICR-5. To this end, we tested whether acute, genetic depletion of RIPK1 phenocopied the effect of R1-ICR-5. We used Doxycycline (Dox)-*Cre;Ripk1fl/fl* MDFs and *LysM-Cre;Ripk1fl/fl* BMDMs to genetically and conditionally delete RIPK1. Like treatment with R1-ICR-5, Dox-induced deletion of *Ripk1* in MDFs$^{Dox\text{-}Cre;Ripk1fl/fl}$ triggered cell death in a RIPK3-dependent manner (**Suppl. Fig. S3M**). RNAi-mediated depletion of *Ripk1* did not further accentuate cell death caused by genetic deletion of RIPK1. Yet, in RIPK1-proficient, non-Dox treated MDFs, RNAi-mediated depletion of RIPK1 did indeed trigger cell death. Likewise, BMDMs$^{LysM\text{-}Cre;Ripk1fl/fl}$ were more sensitive to TNF and TLR3/4 induced necroptosis than WT, Cre-deficient control BMDMs$^{Ripk1fl/fl}$ (Suppl. **Fig. S3N**). Additionally, the triple negative breast cancer cell line EO771$^{Dox\text{-}shRNAi}$, which harbors a Dox-inducible shRNA against *Ripk1*, also became acutely sensitive to TNF-induced necroptosis upon shRNA-mediated depletion of RIPK1 (**Suppl. Fig. S3O**). Together, these data demonstrate that genetic, acute deletion of RIPK1 fully recapitulates the phenotypes caused by R1-ICR-5.

TNFR1 but not TNFR2 was required for TNF-induced cell death following depletion of RIPK1, because treatment with human TNF (hTNF), which only binds to murine TNFR1, was fully capable of inducing necroptosis in BMDMs when RIPK1 was depleted (**Fig. 3F**). As expected, TNF/R1-ICR-5-induced cell death was entirely RIPK1-independent because co-treatment with 3 different RIPK1 kinase inhibitors did not block this death (**Fig. 3G**). However, in the presence of RIPK1, these RIPK1 kinase inhibitors potently blocked TNF-induced cell death, suggesting that the scaffold function of RIPK1 blocks the ability of TNFR1 to trigger RIPK1-independent cell death.

Depletion of RIPK1 not only sensitized cells to exogenous TNF, but also to autocrine-produced TNF. Accordingly, primary BMDMs, which produce TNF, were sensitive to RIPK1-PROTAC treatment alone, and this effect was prevented by genetic deletion of *Tnfr1* or co-treatment with Enbrel, a TNF-neutralizing biologic (**Fig. 3H,I and Suppl. Fig. S3P**). Inhibition of MK2, a key mediator of autocrine TNF biosynthesis[63] also suppressed R1-ICR-5-mediated cell death in primary BMDMs. The inactive control compound R1-ICR-5S, or engagement of VHL using a RIPK2-targeting PROTAC, had no effect on cell viability (**Fig. 3B,I,J**), indicating that the cytotoxicity was specific to RIPK1 depletion and relied on engagement of the TNFR1 pathway.

The cytotoxicity of the PROTACs in BMDMs correlated with their ability to degrade RIPK1, with R1-ICR-5 being the most potent (**Suppl. Fig. S3Q and S1G**). In addition to primary BMDMs, treatment with R1-ICR-5 also killed other cell types, such as mouse dermal fibroblasts and peritoneal macrophages (**Suppl. Fig. S3R,S**), expanding this observation to other cell types. Treatment with PROTAC alone predominantly caused necroptosis in sensitive cells (**Fig. 3J,K and Suppl. Fig. S3S,T**), indicating that TNFR1 signaling can trigger activation of RIPK3 when RIPK1 is acutely depleted, subsequently referred to as 'non-canonical' activation of RIPK3. This suggests that TNF can activate RIPK3 independently of RIPK1 via an unknown mechanism, an observation that has been noted previously[64-67]. Although non-canonical activation of RIPK3 occurs in a range of cell types, we noticed that the response to acute depletion of RIPK1 is cell type specific, with some cell and tissue types not being able to drive TNF-mediated activation of RIPK3 in the absence of RIPK1. For example, naïve $CD8^+$ T cells, $CD4^+$ T cells and keratinocytes[11,16] are resistant to cell death triggered by acute depletion of RIPK1 (**Suppl. Fig. S3U**). Thus, RIPK1 degraders represent a novel means of therapeutically activating non-canonical necroptosis, as is desirable in cancer, where RIPK1 fuels resistance to TNF-induced cell death and immunotherapy[26]. Together these data suggest that RIPK1 suppresses 'over-heating' of TNFR1 and TLR3/4 signaling, thereby licensing tuned activation of immunostimulatory signaling and cell survival.

TNF-induced non-canonical activation of RIPK3 occurs independent of TRIF and ZBP1

Next, we evaluated the mechanism through which TNF drives RIPK3 activation. The current dogma states that RIPK3 activation and necroptosis signaling critically depend on RIPK3's recruitment to proteins containing a RIP Homotypic Interaction Motif (RHIM). RHIMs are conserved protein sequences that facilitate the formation of RHIM:RHIM amyloid fibrils[68]. In humans and mice, the only RHIM-containing proteins are RIPK1, TRIF, ZBP1 and RIPK3[69]. The recruitment of RIPK3 to the RHIM of either RIPK1, TRIF, or ZBP1 through RHIM-dependent interactions can trigger RIPK3 activation and necroptosis. To evaluate the significance of the RHIM of RIPK3, we reconstituted RIPK3-deficient cells with either wild-type (WT) RIPK3 or a mutant form of RIPK3 carrying a defective RHIM ($RIPK3^{RHIMm}$)[70]. While $RIPK3^{WT}$ readily reconstituted TNF-induced necroptosis in the absence of RIPK1, the $RIPK3^{RHIMm}$ failed to do so (**Fig. 3L**), demonstrating the indispensable role of the RHIM of RIPK3, in its activation.

As TRIF and ZBP1 are the only other RHIM containing proteins, we investigated whether TRIF and/or ZBP1 mediate TNFR1-induced non-canonical activation of RIPK3. Double deficiency of TRIF and ZBP1 in primary lung fibroblast (LF) had no impact on TNF-induced cell death upon R1-ICR-5 treatment (**Fig. 3M,N**), ruling out any involvement of these two RHIM-containing proteins. While TRIF deficiency partially reduced R1-ICR-5-induced cell death in primary BMDMs, it did not prevent it entirely (**Fig. 3N**). ZBP1 deficiency did not affect R1-ICR-5-induced cell death. Under more potent cell death conditions, such as in the presence of the pan-caspase inhibitor Emricasan (E) or upon treatment with TNF/SM/E or TNF/cycloheximide (CHX), we observed that TRIF and ZBP1 deficiency had little or no effect on TNF-induced necroptosis in RIPK1-depleted BMDMs (**Fig. 3N and Suppl. Fig. S3V,W**). Our findings are unexpected because whole body or skin-specific deletion or RHIM mutation of RIPK1 in mice, leads to necroptosis in the skin and lethality mediated by ZBP1 and, to a lesser extent, TRIF[11,12,16,71]. However, we did not observe a change in ZBP1 levels upon acute removal of RIPK1 in primary LFs and BMDMs (**Fig. 3M,N**), which contrasts with the *in vivo* situation where expression of ZBP1 is prominently induced at the age of P28[16]. This suggests that the ZBP1-dependent *in vivo* phenotype of *Ripk1*$^{E\text{-}KO}$ and *Ripk1*$^{mRHIM/E\text{-}KO}$ mice might be an indirect, tissue-integrated response to long-term inactivation of RIPK1 function, rather than a direct cell-intrinsic response to loss of RIPK1. Accordingly, enhanced compensatory expression of ZBP1 only occurs 28 days after birth (P28), which subsequently mediates the skin phenotypes observed in *Ripk1*$^{E\text{-}KO}$ and *Ripk1*$^{mRHIM/E\text{-}KO}$ mice[16]. We noticed that *Trif*$^{-/-}$ BMDMs had lower basal expression levels of interferon-responsive genes, such as ISG15, MLKL, and ZBP1 (**Fig. 3N**), suggesting that loss of TRIF might reduce the sensitivity to TNF indirectly by reducing interferon signaling and the expression of interferon-dependent target genes, such as MLKL and TNF[72]. Consistently, we found that IFNAR1 deficiency reduced TNFR1- and TLR3/4-induced cell death in RIPK1-depleted BMDMs (**Fig. 3O and Suppl. Fig. S3K,L**). Taken together, while we find that the RHIM domain of RIPK3 is required for non-canonical necroptosis, other RHIM-containing proteins, such as TRIF and ZBP1, appear to be dispensable for this process.

The death domain of RIPK1 limits TRADD fibrillation and non-canonical RIPK3 activation

Next, we functionally tested the involvement of complex I components in RIPK3 activation. Depletion of TRADD fully protected cells from TNF-induced necroptosis upon PROTAC or genetic depletion of RIPK1 (**Fig. 4A**). While genetic deletion and RNAi-mediated depletion of *Spata2* and *Cyld* partially

protected cells under these conditions, respectively, depletion or pharmacological inhibition of no other signaling component downstream of TNFR1, such as TRAFs, IAPs, LUBAC, TAK1 or IKKs, was capable of suppressing TNFR1-mediated RIPK3 activation (**Fig. 4B,C** and **Suppl. Fig. S4A,B)**. This indicates that TRADD plays a critical role in driving non-canonical activation of RIPK3, independent of other components of TNFR1 complex-I.

TRADD is an adaptor protein with a C-terminal death domain (DD), comprising of two super-secondary structures, an all-helix Greek key motif and a β-hairpin motif flanked by two α-helices, which makes it unique among all known DD structures[73]. RIPK1 not only suppressed the recruitment of TRADD to TNFR1 complex I (**Fig. 2D**), but also prevented its association with RIPK3 in the death-inducing complex II (**Fig. 4D**). Enhanced recruitment of RIPK3 to TRADD correlated with enhanced activation of RIPK3 and MLKL (**Fig. 4D,E**) and cell death (**Fig.4F** and **Suppl. Fig. S4C**). Consistent with the notion that RIPK1 suppresses the binding of TRADD to RIPK3, proximity ligation assay (PLA) and confocal co-localization analysis indicated that TRADD and RIPK3 come into close proximity when RIPK1 is acutely diminished by R1-ICR-5 (**Suppl. Fig. S4D,E**). Since RIPK3 also interacted with TRADD in RIPK1-deficient cells (**Suppl. Fig. S4F**), we next evaluated whether TRADD can directly bind to RIPK3. However, reciprocal *in vitro* binding assays established that recombinant TRADD did not directly bind to RIPK3, suggesting that the interaction between TRADD and RIPK3 is indirect, or might require post-translational modifications (**Suppl. Fig. S4F-I**).

We found that RIPK1 suppressed TRADD aggregation and fibrillation in response to TNF (**Fig. 4G**). Accordingly, treatment with TNF caused the time-dependent accumulation of TRADD aggregates, however only when RIPK1 was depleted. Depletion of RIPK1 by RNAi similarly caused TRADD fibrillation in response to TNF (**Suppl. Fig. S4J,K**). These data are consistent with a model whereby the recruitment of RIPK3 to TRADD fibrils causes a conformational change of RIPK3 that allows RHIM-mediated homo-oligomerization, ubiquitylation and auto-activation. Consistently, TNF stimulation markedly enhanced the oligomerization, ubiquitylation and activation of RIPK3 and MLKL, which was preceded by TRADD ubiquitylation and oligomerization (**Fig. 4H**).

To elucidate how TRADD initiates RIPK3 activation following rapid depletion of RIPK1 by R1-ICR-5, we created several TRADD variants and assessed their capacity to restore TNF-induced RIPK3 activation in TRADD-deficient cells (**Fig. 4I**). While Dox-induced expression (2 h) of TRADD-WT or -DD alone had no effect on the viability of L929 cells, such cells became acutely sensitive to TNF and Emricasan (TE) when RIPK1 was depleted, demonstrating that the DD of TRADD is sufficient to drive TNF-induced activation of necroptosis (**Fig 4I,J and Suppl. Fig. S4L**). Next, we assessed the requirement of TRADD oligomerisation for RIPK3 activation. We noticed that TRADD readily formed higher order oligomers (**Suppl. Fig. S4I)** that were destabilised by reducing agents (**Fig. 4H**), suggesting that di-sulphide bridges might contribute to the formation of TRADD oligomers. To test this, we generated TRADD C>S mutants with substitution mutations on surface exposed Cysteines (Cys) (**Fig. 4I**). We also included a TRADD mutant that no longer binds to TRAFs[74]. While such mutants were still recruited to TNFR1 complex I, they were severely impaired in driving RIPK3-mediated necroptosis upon R1-ICR-5 treatment (**Fig 4I,K** and **Suppl. Fig. S4M**). Particularly, $TRADD^{CallS}$, in which all surface exposed Cys were substituted to Ser, was strongly impaired in driving RIPK3 activation, even though this mutant was recruited to TNFR1 as efficiently as the TRAF-binding mutant ($TRADD^{Y16A/F18A}$) (**Suppl. Fig. S4M**). While the $TRADD^{CallS}$ and $TRADD^{Y16A/F18A}$ mutants failed to recruit TRAF2, cIAPs and LUBAC to complex I, $TRADD^{Y16A/F18A}$ was proficient in activating RIPK3 when RIPK1 was depleted by R1-ICR-5. Under the same conditions, however, $TRADD^{CallS}$ was unable to drive RIPK3-mediated necroptosis. Together, these data are consistent with the notion that di-sulphide bridges are required for TRADD oligomerisation and RIPK3 activation.

Next, we mapped the domain of RIPK1 that suppresses TRADD fibrillation. We found that TRADD-mediated activation of RIPK3 was suppressed by the death domain (DD) of RIPK1 (**Fig. 4L**). Accordingly, Dox-induced expression of RIPK1 truncation mutants ($RIPK1^{\Delta KD\Delta RHIM}$ and $RIPK1^{DD\text{-}only}$), carrying the DD but lacking the RHIM, suppressed TNF-mediated non-canonical activation of necroptosis. As expected, induced expression of RIPK1's DD had no effect on TLR3-mediated activation of necroptosis (**Fig. 4L**). Together, our data suggest that RIPK1 regulates TRADD by competing for TNFR1 occupancy in complex-I. Additionally, RIPK1 might suppress TRADD:TRADD oligomerisation, thereby preventing further accumulation and fibrillation of TRADD and RIPK3 activation (**Fig. 4M**).

PROTAC-mediated degradation of RIPK1 achieves anti-tumor activity

The coordinated exposure to iDAMPs and dead cells can activate immune cells to trigger anti-tumor immunity[46,50]. Since depletion of RIPK1 concomitantly enhances NF-κB/interferon signaling and responsiveness to necroptosis, we explored the potential of using PROTAC-mediated degradation of RIPK1 to trigger immunogenic cell death (ICD) and boost anti-cancer therapies. First, we tested the effects of R1-ICR-5 treatment on several different cancer cell lines. Upon R1-ICR-5 treatment, we found that triple-negative breast cancer (EO771), colon adenocarcinoma (MC38), and fibrosarcoma (MCA-205) cells were fully capable of driving necroptosis in a TNFR1-, TLR3 and IFNR-dependent manner (**Fig. 5A-C**, **Suppl. Fig. S5A**). We also tested the sensitivity of established *Ripk1* deficient EO771 cells, which we generated using CRISPR technology. While most cells died upon genetic deletion of RIPK1, we selected out viable *Ripk1* knockout (KO) EO771 pools, which we found to be resistant to TNF-induced necroptosis upon R1-ICR-5 treatment (**Suppl. Fig. S5B**). The observation that cells become vulnerable to TNF-induced necroptosis following acute pharmacological or genetic removal of RIPK1, yet are resistant to the same stimulus when RIPK1 is permanently deleted, implies that cells ultimately adapt to long-term absence of RIPK1. Further, these data suggest that R1-ICR-5 does not cause any apparent RIPK1-independent cytotoxic off-target effects. We also noticed that treatment with R1-ICR-5 rendered cancer cells acutely sensitive to IFN-induced necroptosis (**Fig. 5C**), which agrees with a previous report using RIPK1-deficient MEFs[12]. Further, we found that R1-ICR-5 also increased the sensitivity of human colorectal adenocarcinoma (HT-29 and Lim-1215) and acute monocytic leukemia cells (THP-1) to TNF-induced necroptosis, following IFNβ priming (**Fig. 5D**). Further, we found that TRADD efficiently associated with activated RIPK3 following the rapid depletion of RIPK1 by R1-ICR-5 in TNBC cells (EO771), leading to increased activation of RIPK3 and necroptosis (**Fig. 5E-G**). Similar to L929 cells, we found that RIPK1's DD effectively suppressed TNF-mediated necroptosis, but not TLR3-induced necroptosis, in EO771 TNBC cells, corroborating the notion that these cancer cells are similarly wired (**Suppl. Fig. S5C**).

Since PROTAC-mediated depletion of RIPK1 sensitized cancer cells to TNF and IFNβ (**Fig. 5A-D**), we hypothesized that R1-ICR-5 could be effectively combined with treatments that generate a tumor micro-environment rich in TNF and IFN, which can be achieved by radiotherapy (RT) and immune checkpoint

blockade (ICB). To this end, we focused on TNBC, which is a heterogenous subset of breast cancer lacking receptors for estrogen, progesterone, and human epidermal growth factor receptor 2 (HER2); consequently, there is currently no standardized treatment regimen, which makes TNBC particularly difficult to treat. Moreover, RT is often used as an adjuvant treatment following surgery, reducing the risk of local recurrence. To test the ability of R1-ICR-5 to improve the therapeutic response of RT, we used the EO771 TNBC cells. Exposure of these cells to RT caused dose-dependent DNA damage (**Suppl. Fig. S5D**), which in turn markedly induced NF-κB and IFN-responsive genes, including genes associated with immunogenic cell death (*Cxcl10* & *Ifnβ*)[75] and TNFRSF signaling (*Tnf* & *Tnfsf10* (*Trail*)) (**Fig. 5H, Suppl. Fig. S5E,F**). RT-induced cytokine production was entirely dependent on TRIF, as Dox-induced depletion of *Trif* abrogated NF-κB- and IFN-dependent target gene expression, in response to RT (**Suppl. Fig. S5G**). RT not only stimulated the production of cytokine and chemokines, but also caused necroptosis in EO771 and MC38 cells that was blocked by MLKL deficiency and enhanced by RIPK1-PROTAC-treatment (**Fig. 5I,J**). Together, this indicates that RIPK1 acts as a survival factor, suppressing RT-mediated cell death. RT-induced and R1-ICR-5 enhanced necroptosis of EO771 was efficiently blocked by MLKL deficiency. RT-induced necroptosis was mediated, at least in part, by TNF because treatment with Enbrel or *Tnfr1* deficiency suppressed the treatment response (**Fig. 5K,L**). We also noticed that TRIF contributed to the treatment response, because RNAi-mediated depletion of *Trif* suppressed RT-induced necroptosis, which was further reduced by concomitantly blocking TNF signaling (**Fig. 5M**). In contrast, depletion of *Zbp1* had a relatively minor impact on RT-induced necroptosis (**Suppl. Fig. S5H**). Together, these observations suggest that cancer cells can hijack RIPK1 to suppress the cellular response to RT.

Next, we tested whether targeting RIPK1 could boost the ability of radiotherapy to 'heat up' tumors *in vivo*. To this end, EO771 TNBC cells were injected orthotopically into the mammary fat pad of immune competent C57BL/6J mice. When tumors reached 50 – 100 mm^3, image-guided RT was administered (8 Gy), followed by three intra-tumoral injections of R1-ICR-5, in 3-day intervals (**Fig. 6A and Suppl. Fig. S6A,B,E**). While RT or R1-ICR-5 had little or no effect on tumor growth and survival as monotherapies (**Fig. 6B-D and Suppl. Fig. S6C,D**), the combination of RT/R1-ICR-5 synergised, achieving therapeutic responses in 50% of treated mice. While 3 out of 10 mice were tumor free beyond 70 days, one mouse relapsed at day 76 (**Fig. 6B-D**). Profiling of treated tumors at early time points, and

before any noticeable differences in response (13 days post-irradiation), revealed a re-shaping of the tumor immune microenvironment by RT/R1-ICR-5, which promoted the infiltration of $TNF^+IFN\gamma^+$ lymphocytes, without affecting the proportion of TNF^+ myeloid cells (**Fig. 6E-G and Suppl. Fig. S6F,O and Suppl. Data S1**). Additionally, this combination favored the recruitment of adaptive and innate lymphocytes, exhibiting key features of activation ($CD69^+$, $CD44^+$, $CD62L^-$) (**Suppl. Fig. S6G-J**) and anti-tumor function (TNF^+, $IFN\gamma^+$, Granzyme B^+ and $CD107a^+$) (**Fig. 6E,F and Suppl. Fig. S6K-N**). The emergence of $CD8^+$ and $CD4^+$ effector memory ($CD4^+$ and $CD8^+$ T_{EM}; $CD44^{hi}CD62L^-$) populations (at early time points (**Suppl. Fig. S6G,H**), suggested that RIPK1 degradation enhanced the RT-induced generation of immunological memory, which was confirmed by cured animals from (**Fig. 6C,D**) being fully resistant to tumor re-challenge (**Fig. 6H,I**). Together, these data indicate that R1-ICR-5 enhances the RT-induced recruitment of activated adaptive and innate lymphocytes in the tumor microenvironment. The increased influx of TNF^+IFNy^+ lymphocytes, along with the enhanced vulnerability of EO771 cancer cells to TNF/IFNy-induced cell death, may contribute to the extended survival of tumor-bearing mice, after treatment with RT/R1-ICR-5.

Next, we evaluated the potential of R1-ICR-5 to boost RT/ICB combination therapy. To test this, we used a lower dose of RT (4 Gy) followed by α-CTLA-4 ± R1-ICR-5 treatment (**Fig 6J-N**). While RT, α-CTLA-4, and RT/α-CTLA-4 had no significant impact in the first 30 days, combining RT/α-CTLA-4 with R1-ICR-5 strongly inhibited tumor growth during the same time period (**Fig. 6K,L**), with 9 out of 10 tumor-bearing mice responding to therapy and 8 being completely cured (**Fig. 6M,N**).

We also determined whether R1-ICR-5 could enhance the anti-tumor efficacy of anti-PD1 treatment, in the absence of RT. While neither R1-ICR-5 or anti-PD1 blockade proved efficacious as single agents, their combination significantly slowed the growth kinetics of treated tumors (**Fig. 7A-D)**. Combination-treated mice benefitted from improved response rates (60% response) and overall survival, with 1/3 of treated mice being completely cured of their tumors (**Fig. 7E**).

Our data indicate that RIPK1 confers resistance to innate immune signaling and immunogenic cell death, to function as a protective factor for cancer cells. This resistance hampers the immunostimulatory

effects of RT, impeding the conversion of immunologically 'cold' tumors into 'hot' tumors. Consistent with our observations, pan-cancer analyses of The Cancer Genome Atlas (TCGA) revealed a strong positive correlation between increased RIPK1 copy number alterations (CNA) and poor disease-free survival (**Fig. 7F**). Moreover, stratifying TNBC patients (SCAN-B dataset) based on RIPK1 and NK cell infiltration (RIPK1-low/NK cell-high or RIPK1-high/NK cell-low), we found that lower RIPK1 and higher NK cell-associated gene expression, were associated with a better overall survival (**Fig. 7G**). Correspondingly, RIPK1-low/NK-high TNBC patients differentially induced genes relating to Type-I and Type-II IFN, regulated cell death and inflammatory responses (**Fig. 7H and Suppl. Fig. S6P**). Consequently, targeting RIPK1 by PROTACs emerges as a promising approach to heat up tumors and overcome resistance to immunostimulatory therapies, such as ICB, RT and combinations thereof.

Acute depletion of RIPK1 in the skin suppresses RIPK1-driven inflammation

Previous work established that aberrant TNF-induced and RIPK1-mediated cell death of keratinocytes can lead to skin pathologies[23]. Since keratinocytes are refractory to non-canonical activation of RIPK3[11,16], we evaluated whether targeted protein degradation of RIPK1 could be achieved with R1-ICR-5 PROTACs *in vivo* (**Suppl. Fig. S7A**), to suppress RIPK1-induced skin inflammation. We found that subcutaneous injection of R1-ICR-3 or R1-ICR-5 on its own did not cause skin toxicity (**Suppl. Fig. S7B,C**), indicating that non-canonical activation of RIPK3 does not operate in the skin. Further, this suggests that short-term depletion of RIPK1 is well tolerated in the skin. Consistently, we found that conditional deletion of *Ripk1* in the skin had little effect in 7-11 weeks old mice, whereas deletion of *Caspase-8* caused deep ulceration and epidermal loss, which was rescued by co-deletion of *Ripk1* (**Suppl. Fig. 7D,E**). To test whether RIPK1-mediated inflammatory phenotypes could be suppressed by RIPK1-PROTAC treatment, we used two skin models. First, we caused RIPK1-dependent cell death and tissue injury by subcutaneous injection of SMAC mimetic and E (SM/E), which was previously shown to mimic inflammatory diseases seen in genetic models of IAP loss[76,77]. While subcutaneous injection of SM/E caused significant ulceration of the skin of control animals at 72 hrs[77], co-injection of R1-ICR-3 and R1-ICR-5 protected animals from SM/E-induced tissue injury (**Suppl. Fig. S7B,C**). The control group treated with SM/E achieved the highest Histological multivariant Lesion Score (HLS) of mean 214 (range 175-257), while the R1-ICR-3 or R1-ICR-5 treated animals reached an HLS mean 49 (range 39-58) and 55 (range 30-70), respectively (**Suppl. Fig. S7C**). Single injections of SM or E on its

own had no effect[77]. In contrast, subcutaneous injection of SM/E caused deep ulceration of the epidermis and subepidermal layer of dermis and showed formation of dense collagenous fibrotic tissue (**Suppl. Fig. 7B,C**), as previously shown[77]. Animals also showed clear evidence of cellular necrosis, including the presence of nuclear dust mostly at superficial or mid dermis. In contrast to SM/E injected animals, co-treatment with R1-ICR-3 or R1-ICR-5 blocked the appearance of the aforementioned features. Accordingly, SM/E/R1-ICR-3 and SM/E/R1-ICR-5 treated animals exhibited an epidermal layer without ulceration (Suppl. **Fig. 7B,C**). Moreover, there was no evidence of necrosis in SM/E/R1-ICR-3 or SM/E/R1-ICR-5 treated animals.

We also tested whether PROTAC-mediated degradation of RIPK1 suppressed the inflammatory pathology driven by TBK1 inactivation. Human TBK1 deficiency leads to severe inflammation that is driven by TNF-induced RIPK1-dependent cell death[78-80]. Since biallelic loss of TBK1 is embryonically lethal in mice[78,81], we developed a pharmacological model for localized loss of TBK1 in mature skin. Subcutaneous injection of the TBK1/IKKε-specific inhibitor MRT67307[82] (subsequently referred to as TBK1i), in combination with TNF, caused deep ulceration and tissue injury (**Suppl. Fig. 7F,G**). Co-treatment with R1-ICR-5 fully protected these animals, suppressing any skin reaction after TNF/TBK1i injection. Treatment with the less potent R1-ICR-3 had an intermediate effect. Together these data demonstrate that RIPK1-mediated inflammatory skin disease can be suppressed effectively by treatments with RIPK1-PROTACs. Unlike RIPK1 kinase inhibitors, which only efficiently block necroptosis in human cells, RIPK1-PROTACs may be effective for the treatment of human pathologies that are driven by RIPK1-induced apoptosis and/or necroptosis. Accordingly, we found that R1-ICR-5 potently suppressed RIPK1-induced caspase activation and apoptosis in a panel of human cell lines (**Suppl. Fig. 7H,I**). In contrast, the RIPK1 kinase inhibitor PK68 and GSK'963 were ineffective to do so in human cells (**Suppl. Fig. S1A,B and S7H,I**). Therefore, PROTACs present a strategy to neutralise inflammo-pathologies caused by RIPK1 activation, particularly in tissues inherently devoid of non-canonical RIPK3 activation.

DISCUSSION

Although multicellular organisms do not rely on a single master regulator of the immune system, there are some key proteins that control the switch between stress sensing and cell death triggering, and for which back-up systems exist to thwart infringements by pathogens. Located downstream of many

cytokine receptors and PRRs, RIPK1 functions as such a signaling regulator[83,84]. RIPK1 can simultaneously coordinate transcriptional inflammatory gene expression (and DAMP production) and cell death pathways. Alterations in RIPK1 signaling are recognized to contribute to inflammatory diseases[25] and cancer[26]. Although RIPK1 has emerged as a drug target, its successful targeting by selective kinase inhibitors has proved to be difficult. This may be due, at least in part, to its bifunctional signaling properties as a scaffold and kinase. Here we report the development of R1-ICR-5 as the first highly selective and efficacious degrader of both human and murine RIPK1. While R1-ICR-5 degrades RIPK1 within a few hours, it has no significant effect on the protein levels of related kinases, such as RIPK2, RIPK3, BRAF or TrkA. The slow resynthesis rate of RIPK1 makes the PROTAC approach a particularly powerful tool for studying the involvement of RIPK1, in various biological processes and diseases.

PROTAC compounds offer unique advantages as they provide a means to degrade disease-associated proteins that were previously considered 'undruggable', such as the scaffolding function of kinases[57]. Furthermore, these observations can unveil alternative signaling pathways that are not easily discernible through genetic deletion of a gene, especially when the gene serves as a protective mechanism against pathogens, and its disruption triggers cell death. Unexpectedly, our data reveal that the acute depletion of RIPK1 leads to the deregulation of innate immune signaling in primary bone marrow derived macrophages and some cancer cells, triggering abnormal activation of NF-κB/IRF signaling and simultaneous induction of necroptosis. This contrasts with previous work demonstrating that RIPK1 is indispensable for TNF & TLR3-induced activation of NF-kB and MAPK signaling[60,85]. Our observation that acute depletion of RIPK1 results in significant rewiring of TNFR1 signaling complex I may help to explain why it has been challenging to identify TNF-dependent but RIPK1-independent activation of RIPK3. We find that in the absence of RIPK1, TRADD unexpectedly accumulates in a stimulus (TNF) and time-dependent fashion. Given that TRADD is the main anchor point for the TRAF2/cIAP ubiquitin-E3 ligase in TNFR1 complex I, an increase in TRADD levels in complex I concurrently causes enhanced recruitment of TRAF2, cIAPs and LUBAC. This, in turn, results in heightened Ub-mediated activation of NF-κB/MAPK signaling and cytokine production. Increased accumulation of TRADD, however, not only alters NF-κB/MAPK activation, but also triggers lethal activation of RIPK3. Although this process requires RIPK3's RHIM domain, it seems to operate

independent of RIPK1, TRIF and ZBP1. However, while our experiments cannot categorically rule out a role for 'residual' RIPK1, our data clearly demonstrate that TNF-induced non-canonical activation of RIPK3 occurs independent of the kinase function of 'residual' RIPK1. This is evident as treatment with highly selective RIPK1 kinase inhibitors have no impact on TNF-induced necroptosis following R1-ICR-5 treatment. Further, RNAi-mediated depletion of RIPK1 in addition to R1-ICR-5 treatment fails to ameliorate TRADD-mediated activation of RIPK3 (**Suppl Fig. S4a**), which is similar to *Ripk1* siRNA in *Cre;Ripk1fl/fl* MDFs in which *Ripk1* was acutely deleted. Therefore, if indeed residual RIPK1 contributes to TNF-mediated activation of RIPK3, then it does so in a non-conventional manner. While more work is needed to identify the exact molecular mechanism of non-canonical activation of RIPK3, we note that many innate immune responses, such as cell death and inflammatory signaling, feature 'prion-like' self-templating and polymerization of one or more signaling protein(s), into large macromolecular condensates/aggregates. Thus, upon acute PROTAC-mediated RIPK1 depletion, TRADD's nucleation capacity seems to become de-repressed, leading to the formation of TRADD aggregates/polymers that in turn can drive RIPK3 activation and necroptosis (**Fig. 4M**). Therefore, in the context of TNFR1, RIPK1 seems to promote cell survival by preventing TRADD accumulation and contributing to fine-tuned activation of NF-κB signaling and NF-κB-dependent induction of pro-survival gene products. Therefore, acute loss of RIPK1 causes both heightened inflammatory signaling and necroptosis induction. These concurrent effects, heightened inflammatory signaling and necroptosis induction following acute RIPK1 depletion, suggest that the actual importance of RIPK1's role may have been underestimated in studies utilizing genetic deletion. Since surviving cells undergo selection, it is probable that they suppress innate immune signaling to evade cell death, as evidenced by primary *Ripk1*$^{-/-}$ MEFs being resistant to TNF-induced necroptosis[12]. As a result, the functional implications of RIPK1 may not be entirely comprehended, as the cells selected during genetic knockout might not accurately portray the full extent of RIPK1's functions. Taken together, RIPK1 licenses tuned activation of TNFR1 and TLRs signaling (e.g. TLR3 and TLR4) by functioning as a nucleation barrier for self-templating polymerization of TRADD and TRIF, thereby preventing these signaling hubs from 'overheating' (**Fig. 2A**). As a consequence, RIPK1 functions as a universal suppressor of necroptosis triggered by death receptors (this study and[64-67]) and PRRs[16,17,64-67,86,87], at least in the cell types herein.

The combination of enhanced immunostimulatory signaling and necroptosis upon RIPK1 depletion, are hallmark features associated with "immunogenic cell death". Targeting immunogenic cell death has emerged as a promising strategy in cancer therapy, as it not only can kill apoptosis-resistant cancer cells, but also stimulate an immune response against tumor cells, potentially enhancing the efficacy and durability of treatments[47]. While RIPK1-PROTACs might be useful to enhance immunogenic cell death, removal of RIPK1 alone is not sufficient since RIPK1 functions as a brake, suppressing immunogenic pathways. Therefore, ligands will be required to engage these pathways, which can be provided by immunostimulatory treatment modalities, such as radiotherapy (RT) or immune checkpoint blockade (ICB). RT and ICB-treatment inherently cause the production and release of DAMPs and cytokines (such as TNF, and IFNβ), which sensitises cells to necroptosis when RIPK1 is depleted. Additionally, RT also stimulates the production of CXCL10, an immunostimulatory chemokine that triggers efficient recruitment and cross-priming of cytotoxic lymphocytes[88,89]. Accordingly, we find that treatment with R1-ICR-5 combines well with radiotherapy and ICB, presumably because these treatment approaches create a tumor microenvironment that is rich in TNF and IFNs, which sensitize cancer cells to non-canonical activation of RIPK3, when RIPK1 is depleted. Consistently, we find that RT/R1-ICR-5 reshapes the tumor immune microenvironment, by favoring the recruitment of $TNF^{+}IFN\gamma^{+}$ lymphocytes, exhibiting key features of activation ($CD69^{+}$, $CD44^{+}$ and $CD62L^{-}$) and anti-tumor function (enhanced degranulation and Granzyme-B^{+}). Accordingly, RT/R1-ICR-5 achieved durable treatment responses, rendering cured mice resistant to tumor-rechallenge.

While loss of sensitivity to TNF/IFN cytotoxicity perpetuates immune evasion and resistance to immunotherapy[26,90-92], we find that acute depletion of RIPK1 re-sensitizes cancer cells to the effect of TNF/IFN, and in combination with RT, promotes the influx of $TNF^{+}IFNy^{+}$ lymphocytes. Correspondingly, stratifying TNBC patients based on tumor RIPK1 and TNF/IFNy-secreting lymphocytes (NK cells) status, revealed that RIPK1-low/NK-high TNBC patients exhibited prolonged overall survival and differentially expressed genes associated with IFN, TNF and regulated cell death signaling, when compared to RIPK1-high/NK-low patients. RT is currently employed to treat around 50% of all cancer patients, and done so with curative intent for head and neck, prostate and lung cancers[93]. RT is usually not an effective treatment for TNBC patients, which are known to face the worst prognosis, when compared to other breast cancer sub-types[94]. However, our findings provide potential new therapeutic

strategies to improve the effectiveness of RT in the context of TNBC and other cancer types, where RT is not used with curative intent. While the use of immunotherapies has revolutionized the treatment of some cancers, most patients remain refractory to treatment[95]. In concordance with R1-ICR-5's ability to restore sensitivity to TNF/IFNs, we also provide evidence that RIPK1 PROTACs enhance the efficiency of anti-cancer immunotherapy (ICB). As such, RIPK1 PROTACs could offer a means of boosting the number of patients that are eligible for such therapies, while also improving the durability of responses.

Uncontrolled excessive inflammatory responses can cause tissue damage and contribute to the pathogenesis of chronic inflammatory diseases[2]. Evidence indicates that aberrant activation of RIPK1 and RIPK1-mediated cell death may be a key mediator of many immune and autoinflammatory diseases, including psoriasis and inflammatory bowel disease, making it a promising therapeutic target[18-23]. Moreover, it contributes to graft versus host disease[96]. However, the clinical use of RIPK1 kinase-specific inhibitors remains a challenge, partly due to RIPK1's distinct scaffolding and kinase functions. The therapeutic approach is hindered by the challenge of kinase inhibitors inadequately suppressing RIPK1's scaffold function in humans, which plays a crucial role not only in kinase-driven necroptosis but also in apoptosis. In contrast to kinase inhibitors, RIPK1 PROTACs are effective in blocking RIPK1-mediated apoptosis and suppress RIPK1-driven skin inflammation. As such, PROTACs offer a novel solution to block RIPK1-driven inflammation, particularly in tissues devoid of non-canonical RIPK3 activation, such as the skin and intestinal epithelial cells.

In summary, we report a RIPK1 PROTAC degrader and provide pharmacological proof-of-concept experiments, which demonstrate that acute depletion of RIPK1 can help to boost anti-cancer immune responses of RT and ICB. We envisage that targeting RIPK1 with PROTACs may become even more important in the future as improved PROTAC molecules are advanced into the clinic.

Limitation of the study

In this study, we demonstrate the enhanced immunostimulatory and anti-tumor effects of RIPK1-selective PROTACs when used in combination with radiotherapy (RT) and immune checkpoint blockade (ICB). Further, we show that local injection of RIPK1 PROTACs can effectively reduce inflammatory skin lesions. However, to further evaluate RIPK1 degraders as potential therapeutic agents and to assess their systemic tolerability, a tool compound that can sufficiently degrade RIPK1 on systemic dosing is needed. Encouraging results from IHC studies of tumor slices, intra-tumorally treated with R1-ICR-5, show that the degradation of RIPK1 within tumors is localized and incomplete, yet associated with inhibited tumor growth, improved survival, and increased immune cell infiltration when combined with radiotherapy. Moreover, our data indicate that the effects of RIPK1 degradation persist for at least 24 hours post compound removal, suggesting that a complete and continuous degradation of RIPK1 may not be essential to initiate an immune response. Nonetheless, a thorough toxicological assessment using a systemically dosed compound in preclinical mouse models will be essential to advance the development of RIPK1 degraders for therapeutic use.

Acknowledgements

The authors are indebted to Clare Isacke, John Silke, Henning Walczak, Geert van Loo, Ulrich Maurer, B.C. Bornhauser, John Caldwell, Angela Hayes, Kai Betteridge, Queenie Lai, Ross Scrimgeour, Jin Wang and the ICR Flow cytometry core facility, who provided materials, technical support and helpful discussions. *Zbp1*$^{-/-}$, *Trif*$^{-/-}$ *and Trif*$^{-/-}$*Zbp1*$^{-/-}$ BMDMs and *Zbp1*$^{-/-}$, *Trif*$^{-/-}$ LF were kind gifts from Manolis Pasparakis. We would like to thank Daniel Glynn and Tom Pesnot at Concept Life Sciences, and Philip Clarke and James Krupa at Charnwood Molecular. We would like to thank all members of the Meier laboratory for support and discussions. Additionally, we would like to thank Peter John-Baptiste and Steven Lumbard for technical support. The tumor and nucleus graphics in Fig.2A and the graphic abstract were created with BioRender.com. Work in the Guo lab is supported by the NIH R21 R21AI175590. Work in the Meier lab is funded by Breast Cancer Now as part of Program Funding to the Breast Cancer Now Toby Robins Research Centre (CTR-QR14-007), CRUK program funding (C26866/A24399), and postgraduate studentships from Cancer Research UK (CRUK) (CRM089X). We acknowledge NHS funding to the NIHR Biomedical Research Centre.

Author contributions

P.M., T.T. and B.B. conceived the study and J.M., P.M. and T.T. designed the research, wrote the paper and generated the figures. J.M. designed, performed, and analyzed experiments in Figs. 1-6 and Suppl. Figs. S1-7. T.T. designed, performed, and analyzed experiments in Figs. 3,4,7 and Suppl. Figs. S1,3,6 and 7. P.M. and T.T. supervised the study. A.B. and designed R1-ICR-3 and B.B. designed R1-ICR-5, -6 and -7. B.B., A.B., K.J.C., N.J.C., O.P., F.R. and F.G. participated in the development of all RIPK1 PROTACs. B.B. and S.H. supervised the design and development of the RIPK1 PROTACs. V.G. performed *in vitro* and *in vivo* radiation experiments, in addition to Fig. 2B, 5A, S1A,B, S3A,O and S7H,I. W.F. performed all *in vivo* experiments. C.T., M.A. and H.B. helped with *in vivo* experiments. L.R., R.W., S.W.J., A.S., N.M.V., S.L., W.L., V.R., H.G., J.U. and A.L., performed *in vitro* experiments. J.S.C supervised the mass spectrometry experiments. S.U., T.I.R. and G.B.H. conducted the mass spec. E.P. performed and analyzed flow cytometry experiments. K.H. supervised the flow cytometry experiments. A.C. and M.M performed and analysed *in vitro* binding assays and SEC experiments. N.G. performed IHC of skin and tumor sections, while C.S. and I.R. analyzed and performed histopathological assessment of these sections. S.H., J.A. and G.M. analyzed and visualized bulk RNA-seq data. M.G. performed survival and GSEA analyses. N.S.A. created the model of TRADD in Fig. 4I. B.B., S.H., V.G., W.F., R.W., S.W.J, A.S. and M.G. provided comments on the manuscript.

Declaration of interests

The authors declare no competing interests.

Figure 1. Development of selective RIPK1 PROTAC degraders

(A) Schematic representation of VHL-based RIPK1 degraders.

(B) Human fibrosarcoma cells (HT1080), conditionally (Dox-inducible) expressing RIPK1-HiBiT fusion proteins, were treated with Dox (100 ng/mL) and the indicated PROTACs for 24 h. RIPK1-HiBiT measurements are shown. RLU, relative light unit.

(C) Western blot analysis evaluating RIPK1 degradation. Human (U937) and mouse (BMDMs) cells were incubated with the indicated concentrations of R1-ICR-5 for 6 h.

(D) The indicated human and mouse cells were treated with the indicated PROTACs for 20 h, before fixation and staining with the indicated antibodies. Endogenous RIPK1 degradation was measured (mean number speckles/cell per well) (Phenix system). Scale bars: 100 μm (HT1080/HT29) and 50 μm (EMT6/L929).

(E) Quantification of endogenous RIPK1 levels from (D).

(F) Human (U937) and mouse (BMDMs) cells were treated with non-VHL binder R1-ICR-5S control or R1-ICR-5 for 6 h, and RIPK1 degradation was analysed by western blot.

(G) Time course analysis of R1-ICR-5 (1 μM) in primary BMDMs, treated for the indicated time points. Where indicated, cells were pre-treated with VH298 (1 μM) or bortezomib (100 nM) for 1 h before R1-ICR-5 exposure. Degradation of the indicated kinases was assessed by western blot analysis. RIPK1 degradation was quantified by densitometry (right panel),

(H) Volcano plot depicting whole proteome of BMDMs treated with R1-ICR-5 (1 μM, 5 h) vs non-treated controls. Log_2 fold change and $-log_{10}$ adjusted *P* values (Benjamin-Hochberg procedure) are shown along the x- and y-axis, respectively.

(I) *Mlkl*$^{-/-}$ BMDMs were treated with DMSO or R1-ICR-5 (1 μM) for 24 h before washout. *Mlkl*$^{-/-}$ cells were used to avoid any effects due to loss of cellular material caused by cell death. Samples were harvested at the indicated time points, and RIPK1 resynthesis was assessed by western blot (left panel) and quantified by densitometry (right panel). Data shown are technical replicates and are representative of 3 independent biological repeats.

Data show ± SD and are representative of $\geq$2 independent biological repeats. Statistical analysis (E,I) was calculated by two-way ANOVA with Sidak's multiple comparison test and (G) one-way ANOVA with Bonferroni's multiple comparison test.

Figure 2. Acute degradation of RIPK1 deregulates TNFR1 and TLR3 signaling

(A) Schematic representation depicting RIPK1's regulation of TNFR1 and TLR3/4-induced signaling and cell death. Ligation of TNF to TNFR1, or engagement of Toll-like receptor TLR4 and TLR3 can lead to innate immune activation and cell death that is regulated by RIPK1. After binding of TNF to TNFR1, or after engagement of TLR3 by double-stranded RNA (dsRNA) or of TLR4 by lipopolysaccharide (LPS), the death domain of TNFR1 or the receptor-interacting protein homotypic interaction motif (RHIM) of TIR-domain-containing adapter-inducing interferon-β (TRIF) interact with the equivalent domain of RIP kinase 1 (RIPK1), which serves as a scaffold to license tuned activation of innate immune signaling and cell death. Under certain conditions, TRADD and TRIF can trigger necroptosis by driving RIPK3 auto-phosphorylation and activation. Once active, RIPK3 phosphorylates and activates mixed-lineage kinase domain-like pseudokinase (MLKL), causing necroptosis. DD, Death Domain; iDAMPs, inducible DAMPs.

(B) Relative mRNA expression of NF-κB target genes, in BMDMs pre-treated with DMSO or R1-ICR-5 for 4 h, followed by indicated TNF treatment.

(C) Relative *Tnf* mRNA expression in BMDMs treated for 4 h with the indicated conditions. MK2i refers to an MK2 inhibitor.

(D) TNFR1 signaling complex I, purified from L929 cells treated with DMSO or R1-ICR-5 (overnight) before treatment with 3xFLAG-TNF for the indicated time points. Lysates were subjected to anti-FLAG IP before western blot analysis with the indicated antibodies.

(E) L929 cells were treated as in (D) before anti-GST-TUBE pulldown to isolate the ubiquitylated proteome. *Indicates non-specific signal.

(F) Western blot analysis of BMDMs pre-treated with DMSO or R1-ICR-5 for 4 h, followed by TNF exposure for the indicated time points.

(G) Relative mRNA expression of NF-κB or IFN target genes. BMDMs were pre-treated with DMSO or R1-ICR-5 for 4 h, followed by stimulation with Poly(I:C).

Data show mean ± SD and are representative of (C,E) two, (B,G) three, (F) four or (D) five independent biological repeats. *P* values were calculated using (B) two-way ANOVA (Sidak's multiple comparison test) or (C,G) one-way ANOVA (Bonferroni's multiple comparison test).

Figure 3. RIPK1 degraders induce TNF- and TLR3/4-driven necroptosis, independent of TRIF and ZBP1

(A, B) Quantification of propidium iodide positive (PI^+) cells, treated with the indicated conditions. The indicated cells were pre-treated with DMSO, R1-ICR-5 or RIPK2 degrader (A,18 h and B,5 h), before stimulation with the indicated conditions (A, 5 h and B, 7 h).

(C) Western blot analysis of RIPK3 and MLKL activation in L929 cells, pre-treated with DMSO or R1-ICR-5 (18 h), before exposure to TNF and Emricasan (TE) for the indicated time points. *Indicates non-specific signal.

(D, E) Quantification of PI^+ of the indicated BMDMs. Cells were pre-treated with DMSO, R1-ICR-3 or R1-ICR-5 for 4 h, followed by the indicated treatments (3 h).

(F) Quantification of PI^+ BMDMs. Cells were pre-treated with DMSO or R1-ICR-5 for 4 h, followed by the indicated treatment.

(G) Quantification of PI^+ L929 cells. Cells were untreated or pre-treated with R1-ICR-5 for 12 h, followed by treatment with the indicated RIPK1 kinase inhibitors and TE. The RIPK1 kinase inhibitors were added 30 min prior to TE (6.5 h).

(H-K) Quantification of PI^+ cells. The indicated cells were treated with R1-ICR-5, R1-ICR-5S (Non-VHL-binding control compound), or MK2 inhibitor for 24 h.

(L) Quantification of PI^+ *Ripk3*$^{-/-}$ LFs. Cells were reconstituted with Dox-inducible WT or RHIM-mutant RIPK3 (*RHIMm*). Cells were induced with Dox and incubated with R1-ICR-5 for 12 h, before treatment with TE for 2.5h.

(M) Quantification of PI^+ LF of the indicated genotypes. Cells were pre-treated with DMSO or R1-ICR-5 for 18 h, following treatment with TE (5 h). *Trif and Zbp1* deficiency was confirmed by western blot analysis. As a positive control for their inability to drive innate immune signaling (induction of ZBP1, which is an interferon-inducible gene), cells were treated with IFNγ (100 ng/mL) over night.

(N) Quantification of PI^+ BMDMs. Cells were treated with the indicated agents for 24 h (left panel). Right panel: western blot analysis of BMDMs following treatment with DMSO or R1-ICR-5 for 6 h.

(O) Quantification of PI^+ BMDMs. The indicated cells were treated with R1-ICR-5 for 24 h.

Data show ± SD and are representative of three (A,D-O), four (B) or two (C) independent biological repeats. *P* values were calculated using (F,H,K,O) one-way ANOVA (Bonferroni multiple comparison test) or (A,B,D,E,G,I,J,L-N) two-way ANOVA (Sidak's multiple comparison test).

Figure 4. RIPK1 degradation facilitates TRADD fibrillation and TRADD-RIPK3 interaction

(A, B) Quantification of PI^+ L929s. Cells were depleted of the indicated genes by RNAi for 48 h, followed by treatment with control or R1-ICR-5 for 24 h. Subsequently, cells were treated with TE for 2 h.

(C) Quantification of PI^+ *Wt* or *Spata2*$^{-/-}$ BMDMs. Cells were pre-treated with DMSO or R1-ICR-5 for 4 h, followed by treatment with TNF with zVAD-fmk (TZ) or Emricasan (TE). Data represent 2 biological replicates (triplicate technical replicate wells per mouse) and are representative of three independent experiments.

(D) TNFR1 complex II analysis using L929$^{Dox\text{-}Flag\text{-}TRADD}$ cells, harbouring a Dox-inducible FLAG-tagged TRADD transgene. Cells were pre-treated with DMSO or R1-ICR-5 overnight. FLAG-TRADD was induced for 1 h (Dox), followed by treatment with TE (1 h). Lysates were subjected to anti-FLAG IP before western blot and densitometry analyses.

(E) Western blot analysis of RIPK3 and MLKL activation in L929$^{Dox\text{-}Flag\text{-}TRADD}$. Cells were pre-treated with DMSO or R1-ICR-5 for 18 h, followed by 1 h induction of FLAG-TRADD (Dox). Subsequently, cells were treated with TE for the indicated time points. *Indicates non-specific signal.

(F) Quantification of PI^+ L929$^{Dox\text{-}Flag\text{-}TRADD}$ cells. Cells were pre-treated with DMSO or R1-ICR-5 for 18 h, followed by 1 h induction of TRADD (Dox). Subsequently, cells were treated with TE (2 h).

(G) Confocal microscopy images of TRADD fibrils using L929$^{Dox\text{-}Flag\text{-}TRADD}$. Cells were treated with DMSO or R1-ICR-5 overnight, followed by 1 h Dox-induced expression of FLAG-TRADD (in the presence of E). Subsequently, cells were treated with TNF for 10 minutes. i) and ii) indicate magnifications of the indicated areas. The right panel indicates the quantification of the number of TRADD aggregates per cell (~70 cells/condition). Scale bars indicate 50 μm and 10 μm in i) and ii), respectively.

(H) Analysis of the ubiquitylated proteome. L929 were pre-treated with DMSO or R1-ICR-5 overnight, followed by treatment with TE for the indicated time points. Cells were subjected to TUBE pull-down. Samples were split into two and boiled with or without β-mercaptoethanol (reducing or non-reducing) to visualize higher-order assemblies by western blotting. *Indicates non-specific signal.

(I) Predicted AlphaFold structure of mTRADD's N- and C-terminal domains (AF-Q3U0V2-F1, left panel)[97]. C198 has a confidence of 45-58 %, whereas all other cysteines have a >85 % confidence. Right panel indicates schematic representations of mTRADD constructs used to reconstitute L929 *Tradd*$^{-/-}$ cells in (j,k). DD, Death Domain.

(J,K) Quantification of PI^+ of the indicated L929 *Tradd*$^{-/-}$ cells, reconstituted with the indicated Dox-inducible TRADD transgenes (see i). Cells were treated with DMSO or R1-ICR-5 overnight, prior to treatment with Dox/E for 2 h. Subsequently, cells were treated with TNF for 3h.

(L) Quantification of PI^+ L929 cells, stably expressing Dox-inducible RIPK1 constructs. Cells were treated with DMSO or R1-ICR-5 overnight, before incubation with Dox/E for 3 h. Subsequently, cells were treated with TNF or Poly(I:C).

(M) Schematic diagram depicting rewiring of TNFR1-mediated activation of RIPK3 when RIPK1 is acutely depleted by R1-ICR-5. RIPK1, through its DD (Death domain), competes with TRADD for the binding of TNFR1. Upon depletion of RIPK1, TRADD is enriched at the TNFR1 signaling complex I, ultimately leading to accentuated formation of complex II, RIPK3 activation and induction of necroptosis. Data show ± SD and are representative of (a-c,f-h,j-l) three or (d,e) two independent biological repeats. *P* values were calculated using (d,k) one-way ANOVA (Bonferroni multiple comparison test) or (a-c,f,j,m) two-way ANOVA (Sidak's multiple comparison test) or (g) unpaired t-tests.

Figure 5. RIPK1 protects cancer cells from TNF and IFN-induced cell death

(A,B) Quantification of PI^+ of the indicated murine cancer cell lines. Cells were pre-incubated with DMSO or R1-ICR-5 for 4 h. Subsequently cells were left untreated or stimulated with TNF or TE in the presence and absence of RIPK3 inhibitors (6, 48 and 24 h for EO771, MC38 and MCA-205, respectively).

(C) Quantification of PI^+ of the indicated murine cancer cell lines. EO771 cells were pre-treated with DMSO or R1-ICR-5 (4 h), before 24 h of IFNβ or IFNγ. MCA-205 and MC38 were pre-treated overnight with IFNγ before incubation with DMSO or R1-ICR-5 for 24 h (MCA-205) or 48 h (MC38).

(D) Quantification of PI^+ human cell lines. Cells were pre-treatment with IFNβ in the presence of E overnight. Subsequently, cells were treated with R1-ICR-5 for 5 h, before TNF treatment (24 h).

(E) Purification of TNFR1 complex II from $EO771^{Dox\text{-}FLAG\text{-}TRADD}$ cells. Cells were treated with DMSO or R1- ICR-5 for 2 h, before induction of TRADD for 2 h (Dox). Cells were subsequently treated as indicated. Lysates and complex II were analyzed by western blotting. Densitometry was used to quantify P-RIPK3. P-RIPK3 signal was normalized to purified TRADD.

(F) Western blot analysis of the indicated proteins in $EO771^{Dox\text{-}FLAG\text{-}TRADD}$. Cells were pre-treated with DMSO or R1-ICR-5 for 4 h. Subsequently, TRADD was induced with Dox and cells were treated with TE for the indicated time points.

(G) Quantification of PI^+ $EO771^{Dox\text{-}FLAG\text{-}TRADD}$, treated as in (F). Data are triplicate technical repeats and are representative of two independent biological repeats.

(H) IFNβ and TNF gene expression analysis of EO771 cells left untreated or exposed to 8 Gy irradiation (single fraction). Data show mean ± SD and are representative of three biological repeats. Statistical analysis was performed by unpaired t test.

(I-L) Quantification of PI^+ of the indicated cells, subjected to the indicated dose of irradiation. 24 h after treatment, cells were incubated with DMSO or R1-ICR-5 for 24 h. (K) Enbrel was added 30 minutes prior to irradiation.

(m) Quantification of PI^+ EO771 cells, stably expressing the indicated *shRNA* constructs, treated as in (K) in the presence of Dox.

Data show ± SD and are representative of (A-D,F,H-M) three, (E) two or (G) four independent biological repeats. *P* values were calculated using two-way ANOVA (Sidak's multiple comparison).

Figure 6. RIPK1 functions as a protective factor for cancer cells against the effects of RT

(A) Schematic depicting the treatment regimen of EO771 tumor bearing mice. I.T, Intratumoral injection.

(B) Tumor growth curves of EO771 tumor-bearing mice treated as depicted in (A): sham (n = 8), RT (n = 11), RT/R1-ICR-5 (n = 10). Thick lines represent average tumor growth. Curves represent two independent experiments.

(C) Survival curves of EO771 tumor bearing mice treated as depicted in (A,B). Curves represent two independent experiments. R1-ICR-5 provides significant survival advantage to RT-treated mice: median survival (RT = 24 days; RT/R1-ICR-5 = 35 days) (Logrank (Mantel-cox) *P*=0.0290).

(D) Pie-charts depicting the response of treated mice from (A,C). R1-ICR-5 enhances the therapeutic response to RT (Chi-square test – Sham Vs RT/R1-ICR-5, *P*=0.0186; RT Vs RT/R1-ICR-5, *P*=0.0382).

(E-G) Flow cytometry analysis of tumors treated as in (A) and harvested on day 13 post-RT. Sham (n=10), RT (n=9) and RT/R1-ICR-5 (n=8). Data are representative of two independent experiments.

(E) The number of TNFα^+IFNγ^+ immune (CD45$^+$) and non-immune cells (CD45$^-$) per gram of tumor.

(F) The number of TNFα^+IFNγ^+ lymphocytes per gram of tumor.

(G) The number of CD45$^+$, CD8$^+$ T, CD4$^+$ conventional T (CD4$_{cv}$), γδ T, NK and NK T cells per gram of tumor.

(H) Tumor rechallenge experiment. Data show the growth curves of EO771 mammary tumors, in naïve mice (n=7, black lines) or RT/R1-ICR-5-treated tumor-free mice from (A-D) (100 days post-treatment (n=2, red lines). Each line represents 1 animal, thick lines denote average tumor growth. I.P, intraperitoneal injection; I.T, intratumoral injection.

(I) Pie-charts depicting the proportion of mice bearing tumors, 42-days after re-challenge with EO771 cells (H). Mice treated with RT/R1-ICR-5 showed greater resistance to tumor growth than naïve mice (Chi-square test, *P*=0.0027).

(J) Schematic depicting the treatment regimen of EO771 tumor bearing mice.

(K) Tumor growth curves of mice treated as in (J). Thick lines represent average tumor growth. Treated mice: IgG (n = 5), anti-CTLA4 (n = 7), RT (n = 10), RT/R1-ICR-5 (n=10), RT/anti-CTLA-4 (n=10) and RT/anti-CTLA-4/R1-ICR-5 (n=10).

(L) Tumor growth kinetics (day 0-30) of mice treated as in (J-K), measured by area under the curve (AUC). Each point represents the AUC of individual mice, from (K).

(M) Survival curves of C57BL/6J mice treated as in (J,K). Curves are representative of one biological replicate. R1-ICR-5 provided survival advantage to mice treated with RT/anti-CTLA-4 (median survival RT/anti-CTLA-4 = 70.5 days; RT/anti-CTLA-4/R1-ICR-5) = undefined).

(N) Pie-charts depicting the response of tumor-bearing mice treated as in (i-m).

Data show ± SD. *P* values were calculated using (C,M) Log-rank (Mantel-Cox), (D,I,N) Chi-square test (Comparing progression Vs complete response), (E-G) or Kruskal Wallis test or (L) one-way ANOVA (Bonferroni's multiple comparison test).

Figure 7. RIPK1 PROTACs enhance response to immune checkpoint blockade

(A) Schematic depicting the treatment regimen of EO771 tumor bearing mice. I.P, intraperitoneal injection; I.T, intratumoral injection.

(B) Tumor growth curves of EO771 tumor bearing mice treated as in (A). Thick lines represent average tumor growth. Treated mice: IgG (n = 8), R1-ICR-5 (n = 9), anti-PD-1 (n = 8), R1-ICR-5/anti-PD-1 (n=10).

(C) Tumor growth kinetics (day 0-21) of mice treated as in (A), measured by area under the curve (AUC). Each point represents the AUC of individual mice, from (B).

(D) Survival curves of tumor bearing mice treated as in (A). Curves are representative of one independent experiment. R1-ICR-5 improves the median survival of mice treated with anti-PD-1 (median survival: anti-PD-1 = 28.5 days; R1-ICR-5/anti-PD-1 = 36.5 days).

(E) Pie-charts depicting the response of tumor-bearing mice treated as in (A-D). R1-ICR-5 improved the response of PD-1-treated mice (Chi-square test – Captisol/IgG Vs PD-1, P=0.0209; Captisol/IgG Vs PD-1/R1-ICR-5, P=0.0073).

(F) Association of RIPK1 copy number alterations (CNA) with disease free survival in TCGA patients (n=2,601) across multiple tumor types.

(G) Overall survival in RIPK1-low and NK-high versus RIPK1-high and NK-low patient groups from SCAN-B TNBC dataset (n=148).

(H) Gene set enrichment analysis (GSEA) of indicated gene sets in RIPK1-low and NK-high versus RIPK1-high and NK-low TNBC patients (n=148). FDR, False discovery rate q-value; NES, Normalised enrichment score.

Data show ± SD. P values were calculated using (C) one-way ANOVA (Bonferroni's multiple comparison test), (D,F,G) Logrank (Mantel-Cox) or (E) Chi-square test (Comparing progression Vs complete response).

STAR METHODS

Detailed methods are provided in the online version of this paper and include the following:

Key resources table

Resource availability

Lead contact

Further information and reasonable requests for resources and reagents should be directed to and will be fulfilled by the lead contact, Pascal Meier (pmeier@icr.ac.uk).

Materials availability

Materials generated in this study are available upon reasonable request and will be fulfilled under a material transfer agreement (MTA).

Data and code availability

- Raw RNA-Seq data for the mammary tumor cell line (EO771) have been deposited in the Sequence Read Archive under the accession number **PRJNA1094427**. The mass spectrometry proteomics data have been deposited to the ProteomeXchange Consortium via the PRIDE[98] partner repository with the dataset identifier **PXD043560**.
- Original immunohistochemistry, microscopy and western blot images have been deposited at Mendeley and are publicly available (**DOI: 10.17632/822syk52yw.1**). All other raw data reported in this paper will be shared by the lead contact upon reasonable request.
- This paper analyses existing, publicly available data. These accession numbers for the datasets are listed in the key resources table.
- This paper does not report original code.
- Any additional information required to reanalyse the data reported in this paper is available from the lead contact upon request.

Experimental model and subject details

Cell lines

293T, HT1080, U937, HT29, MDA-MB-231, MDA-MB-361, MDA-MB-468, HaCaT, LLC, L929, THP-1 and EMT6 were from ATCC. F3II cells (kindly provided by Daniel Alonso), D2A1 cells (kindly provided by Clare Isacke), Kym-1 (kindly provided by John Silke), immortalised MDFs (generated in house) and MC38 (Kerafast). Aforementioned cell lines were cultured in DMEM. E0771 cells (CH3 BioSystems™) and MCA-205 (Sigma) were cultured in RPMI 1640 medium (Thermo Fisher Scientific). Culture media were supplemented with 10% FBS (Sigma Aldrich, #A2153) and 1% penicillin/streptomycin.MCA-205 were additionally cultured with 2-mercaptoethanol (50 µm) and MC38s and EO771s were additionally cultured in the presence of Hepes (5mM). All cell lines were maintained at 37°C, in 10% CO_2.

Primary cells

Primary bone marrow-derived macrophages (BMDMs) and mouse dermal fibroblasts (MDFs) of indicated genotypes were isolated as previously described[7776]. In brief, bone marrows were isolated form tibia and femur of 8-12-week-old mice and plated in non-coated Petri dishes and cultured for 6 days in DMEM (+10% FCS and Penicillin and Streptomycin) supplemented with recombinant M-CSF (20 ng/mL) or L929 mouse fibroblast conditioned medium (20%, v/v). Primary MDFs were isolated from the tail of adult 2 months old mice (Laura's paper). In brief the skin of the tail was cut in small pieces and digested with 3ml of trypsin for 45min at 37°C. Medium was added and digested skin pieces were filtered through a 100µm strainer. The strained medium was placed in 10cm dish and incubated at

37°C/5% CO2 for 2-3 days. Next MDFs were immortalized with pBABE SV40 (large T antigen Δ89-97-missing Bub1[99]). Lung fibroblasts (LFs) were obtained by homogenizing lungs of 8-12-week-old mice in neat DMEM and 1X Gentle Collagenase/Hyaluronidase, before shaking (2000 rpm) for 45 min at 37°C. Suspensions were filtered (70 µm cell strainer), before pelleting (250G). Suspensions were cultured in DMEM (+10% FBS and 1% Penicillin/Streptomycin). Indicated LFs were immortalized as above with pBABE SV 40. All cells were cultured in DMEM supplemented with 10% FBS (Sigma Aldrich, #A2153) and 1% penicillin/streptomycin and maintained at 37°C, in 10% CO_2. Primary naïve T-cells ($CD4^+$ and $CD8^+$) cells were [100].

Mice

C57BL/6 *Wt* (Charles River), *UBC-Cre-ER^{T2}* (referred to as *CreER^{T2}*), *Casp8$^{fl/fl}$*, *Tnfr1$^{-/-}$* and *Ifnar1$^{-/-}$* were from The Jackson Laboratory, *Mlkl$^{-/-}$* and *Casp8$^{-/-}$Ripk3$^{-/-}$* (Kind gifts from Prof. Henning Walczak) and *Ripk1$^{fl/fl}$* (Kind gifts from Prof. Manolis Pasparakis) (See key resources table for more information). All mice were maintained on C57BL/6 background. For tumor treatments, 5 – 6 weeks old female C57BL/6 mice were purchased from Charles River and were enrolled in the study post an acclimatization period of at least one week. Mice were randomly assigned to treatment groups and studies were performed in a blinded fashion. All animal procedures were conducted within the guidelines of UK Home Office in accordance with Animals (Scientific Procedure) Act (ASPA) 1986, amended 2012 and the institutional guidelines of the Institute of Cancer Research. The Animal Welfare Ethical Review Body (AWERB) reviewed the protocols within the project license.

Method details

PROTAC degrader chemical synthesis

Synthesis of R1-ICR-3 [cyclohexyl (5-(2-((S)-15-((2S,4R)-4-hydroxy-2-((4-(4-methylthiazol-5-yl)benzyl)carbamoyl)pyrrolidine-1-carbonyl)-16,16-dimethyl-13-oxo-4,7,10-trioxa-14-azaheptadecanamido)benzo[d]thiazol-6-yl)-2-methylpyridin-3-yl)carbamate]

To a solution of cyclohexyl (5-(2-aminobenzo[*d*]thiazol-6-yl)-2-methylpyridin-3-yl)carbamate (115 mg, 0.30 mmol) and (S)-15-((2S,4R)-4-hydroxy-2-((4-(4-methylthiazol-5-yl)benzyl)carbamoyl)pyrrolidine-1-carbonyl)-16,16-dimethyl-13-oxo-4,7,10-trioxa-14-azaheptadecanoic acid (50 mg, 0.075 mmol) in DMF (5 mL), was added DIPEA (0.039 mL, 0.226 mmol) followed by COMU (64.6 mg, 0.151 mmol). The reaction was heated to 50 °C for 18 hours then purified via HPLC (C18, 35-55% acetonitrile in 10mM ammonium bicarbonate, 0.1% ammonia) to give the title compound as an off white solid (37.7 mg, 0.037 mmol, 48.6%; m/z 1027.4422, expected 1027.4416 for $C_{52}H_{66}N_8O_{10}S_2$ $[M+H]^+$).

Synthesis of R1-ICR-5: cyclohexyl (5-(2-(12-(((S)-1-((2S,4R)-4-hydroxy-2-((4-(4-methylthiazol-5-yl)benzyl)carbamoyl)pyrrolidin-1-yl)-3,3-dimethyl-1-oxobutan-2-yl)amino)-12-oxododecanamido)benzo[d]thiazol-6-yl)-2-methylpyridin-3-yl)carbamate

Step 1: cyclohexyl (5-(2-aminobenzo[*d*]thiazol-6-yl)-2-methylpyridin-3-yl)carbamate (0.4 g, 1.05 mmol), 12-(tert-butoxy)-12-oxododecanoic acid (0.31 g, 1.1 mmol) and TCFH (0.88 g, 3.14 mmol) was dissolved in DMF (10 mL) then diluted with acetonitrile (60 mL). 1-Methylimidazole (0.74 mL, 9.4 mmol) was then added and the resulting solution was stirred at 23 °C for 17 h. Volatiles were removed by evaporation under reduced pressure. The resulting mixture was quenched with water (20 mL) and precipitate collected via suction filtration. The solid was redissolved in DCM, dried, filtered and concentrated to yield tert-butyl 12-((6-(5-(((cyclohexyloxy)carbonyl)amino)-6-methylpyridin-3-yl)benzo[d]thiazol-2-yl)amino)-12-oxododecanoate (R1-ICR-5a, 680 mg, 100%, 1.05 mmol; m/z: 651.4).

Step 2: Trifluoroacetic acid (4 mL, 52 mmol) was added to a solution of R1-ICR-5a (680 mg, 1.05 mmol) in DCM (10mL) and the resulting solution was stirred at 23 °C for 1h then concentrated under reduced pressure to yield 12-((6-(5-(((cyclohexyloxy)carbonyl)amino)-6-methylpyridin-3-yl)benzo[d]thiazol-2-yl)amino)-12-oxododecanoic acid (R1-ICR-5b, 621 mg, 100%, 1.04 mmol; m/z: 595.3).

Step 3: HATU (1.19 g, 3.13 mmol) was added to a 0 °C solution of R1-ICR-5b (0.62 g, 1.04 mmol) and DIPEA (1.82 mL, 10.4 mmol) in DMF (10mL) and the resulting mixture was maintained at 0 °C. After 15 min (2S,4R)-1-((S)-2-amino-3,3-dimethylbutanoyl)-4-hydroxy-N-(4-(4-methylthiazol-5-yl)benzyl)pyrrolidine-2-carboxamide (0.49 g, 1.15 mmol) was added and the resulting solution was

stirred at 23 °C for 17 h, then cooled to 0 °C before water (50 mL) was added to precipitate the product. The white solid was collected via suction filtration and the filter cake was washed with water (3 x 50 mL), then dissolved in DCM, dried over magnesium sulfate, filtered and concentrated. Sequential purification using Isolute-NH_2 column, reverse phase chromatography (C18, 40-100% methanol in water, 0.1% formic acid) then SCX column gave R1-ICR-5 as a white solid (887 mg, 83%, 0.87 mmol, m/z 1007.4894, expected 1007.4887 for $C_{54}H_{71}N_8O_7S_2$ $[M+H]^+$).

Synthesis of R1-ICR-6 [cyclohexyl (5-(2-(3-(3-(3-(((S)-1-((2S,4R)-4-hydroxy-2-((4-(4-methylthiazol-5-yl)benzyl)carbamoyl)pyrrolidin-1-yl)-3,3-dimethyl-1-oxobutan-2-yl)amino)-3-oxopropoxy)propoxy)propanamido)benzo[d]thiazol-6-yl)-2-methylpyridin-3-yl)carbamate]

Step 1: To 3-(3-(3-ethoxy-3-oxopropoxy)propoxy)propanoic acid (33 mg, 0.13 mmol) in DMF (0.5 mL) was added sequentially DIPEA (35 µL, 0.20 mmol) then HATU (55 mg, 0.15 mmol). After 15 minutes cyclohexyl (5-(2-aminobenzo[d]thiazol-6-yl)-2-methylpyridin-3-yl)carbamate (45 mg, 0.12 mmol) in DMF (0.7 mL) was added. The resulting mixture was stirred at room temperature for 5 days. Added water (0.5mL) and evaporated under reduced pressure at 50 °C, then purified by reverse-phase flash chromatography (C18, 70-100% methanol in water, 0.1% formic acid) to give 3-(3-(3-((6-(5-(((cyclohexyloxy)carbonyl)amino)-6-methylpyridin-3-yl)benzo[d]thiazol-2-yl)amino)-3-oxopropoxy)propoxy)propanoic acid (R1-ICR-6a, 13.6 mg, 20%, 0.0233 mmol; m/z 585.2375 expected 585.2377 for $C_{29}H_{37}N_4O_7S$ $[M+H]^+$)

Step 2: To a mixture of R1-ICR-6a (5 mg, 0.0086 mmol), (2*S*,4*R*)-1-((*S*)-2-amino-3,3-dimethylbutanoyl)-4-hydroxy-*N*-(4-(4-methylthiazol-5-yl)benzyl)pyrrolidine-2-carboxamide hydrochloride (4 mg, 0.0086 mmol) in DMF (0.3 mL) at 0 °C under nitrogen was added DIPEA (3 µL, 0.017 mmol) then COMU (4 mg, 0.0093 mmol) in DMF (0.2 mL). The mixture was stirred for 2 days at rt. Additional DIPEA (0.01 mL) and COMU (4 mg) was added and stirred for 3 hours then purified by reverse phase flash chromatography (C18, 10-100% methanol in water, 0.1% formic acid) to give R1-ICR-6 (4 mg, 47%, 0.004 mmol; m/z 997.4341 expected 997.4310 for $C_{51}H_{65}N_8O_9S_2$ $[M+H]^+$)

Synthesis of R1-ICR-7 [cyclohexyl (5-(2-((S)-16-((2S,4R)-4-hydroxy-2-((4-(4-methylthiazol-5-yl)benzyl)carbamoyl)pyrrolidine-1-carbonyl)-17,17-dimethyl-14-oxo-3,6,9,12-tetraoxa-15-azaoctadecanamido)benzo[d]thiazol-6-yl)-2-methylpyridin-3-yl)carbamate]

Step 1: To 3,6,9,12-tetraoxatetradecanedioic acid (120 mg, 0.45 mmol) in DMF (0.5 mL) was added sequentially DIPEA (35 µl, 0.20 mmol) then HATU (65 mg, 0.17 mmol). After 15 minutes cyclohexyl (5-(2-aminobenzo[d]thiazol-6-yl)-2-methylpyridin-3-yl)carbamate (45 mg, 0.12 mmol) in DMF (0.7 mL) was added. The resulting mixture was stirred at room temperature for 5 days, and was then purified by reverse-phase flash chromatography (C18, 10-100% methanol in water, 0.1% formic acid) to give 14-((6-(5-(((cyclohexyloxy)carbonyl)amino)-6-methylpyridin-3-yl)benzo[d]thiazol-2-yl)amino)-14-oxo-3,6,9,12-tetraoxatetradecanoic acid (R1-ICR-7a, 21.5 mg, 29%, 0.0341 mmol, m/z 631.2434 expected 631.2432 for $C_{30}H_{39}N_4O_9S$ $[M+H]^+$).

Step 2: Starting from R1-ICR-7a (5.4mg, 0.0086 mmol), followed method used for synthesis of R1-ICR-6 to obtain R1-ICR-7 (5 mg, 56%, 0.0048 mmol; m/z 1043.4432 expected 1043.4370 for $C_{52}H_{67}N_8O_{11}S_2$ $[M+H]^+$.)

Synthesis of R1-ICR-5S [cyclohexyl (5-(2-(12-(((S)-1-((2S,4S)-4-hydroxy-2-((4-(4-methylthiazol-5-yl)benzyl)carbamoyl)pyrrolidin-1-yl)-3,3-dimethyl-1-oxobutan-2-yl)amino)-12-oxododecanamido)benzo[d]thiazol-6-yl)-2-methylpyridin-3-yl)carbamate]

Prepared from R1-ICR-5b (36 mg, 0.06 mmol) using the same method as for R1-ICR-5, except purified by HPLC (C18, 40-100% methanol in water, 0.1% formic acid) to obtain R1-ICR-5S (24 mg, 39%, 0.0236 mmol; m/z 1007.4899, expected 1007.4887 for $C_{54}H_{71}N_8O_7S_2$ $[M+H]^+$).

Generation of lentiviral particles

To generate lentiviral particles, HEK293T cells were transfected with packaging construct psPAX, pMD2.G and the relevant lentiviral plasmid employing the Effectene transfection kit (301427, Qiagen). Viral supernatants were harvested, passed through a 0.45 µm filter, concentrated with the Lenti-X concentrator (621231, Clontech Takara) and supplemented with Polybrene (10 µg/ml).

Constructs

SMART vector inducible lentiviral shRNAs targeting *Trif* (Also known as *Ticam1*, V3SM11253-235355483), *Zbp1* (V3SM11253-235538171, *Ripk1* (V3SM11253-237881699) and non-targeting (NT) shRNA control (VSC11502) were purchased from Dharmacon. Cells were infected and stable cells were selected with Puromycin (1 µg/ml). Mouse Flag-TRADD constructs were cloned into Dox-inducible lentiviral pTIBZ vector and pool of stable cells was generated after selection with Blasticidin (10 µg/ml). Mouse RIPK3 and RHIM domain mutant of RIPK3 were cloned into the lentiviral vector pTIBZ and stable cell lines were created after infection of transformed LF-*Ripk3*$^{-/-}$ and selection with Blasticidin (10 µg/ml). For generation of inducible Ripk1 deletion, immortalized MDFs-*Ripk1*$^{fl/fl}$ were infected with lentivirus expressing inducible CRE (pTIBZ-*Cre*) and stable clones were isolated after Blasticidin (10 µg/ml) selection. Human RIPK1$^{\Delta RHIM\Delta DD}$-HiBiT construct was generated by PCR and cloned in lentiviral vector (pTIPZ) and expressed under a Dox-inducible promoter. Stable HT1080 cells were isolated after infection and selection with Puromycin (1 µg/ml). Mouse cDNAs of *Ripk1*, *Ripk3*, *Tradd*, *Trif* (also known as *ticam1*) and *Zbp1* were cloned in mammalian expression vector pcDNA3 with corresponding tags and sequence verified. Mouse RIPK3 was generated by coupled *in vitro* transcription/translation reactions using HeLa extracts following synthesis of a PCR fragment which included a 5' T7 promoter, IRES and kozak sequence and a 3' poly A tail according to the application notes of the manufacturer's protocol (Thermofisher Inc.). For bacterial expression, mouse Flag-TRADD was cloned into pTYB1 vector (NEB).

CRISPR gene targeting

Guide RNAs were designed using *crispr.mit.edu* portal (sequence can be obtained upon request). sgRNA for mouse genes *Mlkl, Tnfr1, Tradd and Ripk1* were cloned into pLC-GFP plasmid (plasmid expressing Cas9 and GFP, kind gift from B.C. Bornhauser). For targeting human *Ripk1* gene, co-transfection was done with two plasmids, Cas9 plasmid (Addgene #48138) and plasmid expressing sgRNA for human Ripk1 (Invitrogen synthesis). Control cell lines were created by transfection with corresponding Cas9 expressing plasmids without sgRNA. Cells were transfected with electroporation and 72 h after, GFP positive cells were FACS sorted and single clones were screened for gene knockout by western blot for respective proteins. See Key resources table and Supplementary Table S3 for more information.

mTradd gRNA: CGCAACTGGACGATGAGCTG
mRipk1 gRNA: AGGGAACTATTCGCTGGTGA
hRipk1 gRNA: GCTCGGGCGCCATGTAGTAG
mMlkl gRNA: CTGGCAGCAGGAAGATCGAC
mTnfr1 gRNA: CGGACAGTCACTCACCAAGT

RNA interference

All siRNAs were purchased from Qiagen or Dharmacon (product information can be found in supplementary table S3). In brief, transfection of cells was performed in 96 or 384 well plates using RNAiMAX transfection reagent (Thermo Fisher Scientific). Cells were incubated with transfection mix for 18h and medium was replaced. All experiments were done between 48h-72h post transfection.

Bioluminescence-based RIPK1$^{\Delta RHIM\Delta DD}$-HiBiT degradation assay

Protein degradation parameters DC_{50} values (compound concentration at which 50% of RIPK1$^{\Delta RHIM\Delta DD}$-HiBiT protein is degraded) and Dmax (maximal degradation level relative to positive control R1-ICR-5) were determined in HT1080 cells (ATCC) stably expressing Dox-inducible RIPK1$^{\Delta RHIM\Delta DD}$-HiBiT in a bioluminescence-based assay. Compounds were dispensed in 384 well Cell Culture Microplates (Greiner catalogue 781091) using an ECHO550 acoustic dispenser (Beckman Coulter). HT1080-RIPK1$^{\Delta RHIM\Delta DD}$-HiBiT cells were subsequently plated on top of the compounds. Cells were incubated with compounds for 24 h at 37ºC/10%CO2. RIPK1$^{\Delta RHIM\Delta DD}$-HiBiT was detected using the Nano-Glo HiBiT Lytic Detection Kit (Promega catalogue N3030) according to the manufacturer's instructions. The % response at each concentration was calculated by normalizing RIPK1$^{\Delta RHIM\Delta DD}$-HiBiT expression in

the presence of the compound to the appropriate high (DMSO) and low (1.5μM R1-ICR-5) controls. The compound DC_{50} and Dmax values were determined using Dotmatics (Bishops Stortford, UK) software by fitting the normalized data to a sigmoidal four-parameter logistic (removed "fit") equation.

Immunofluorescence

Cytoplasmic RIP1 protein degradation parameters were quantified in an immunofluorescence-based assay using an Opera Phenix Plus High Content Imaging System (Perkin Elmer). Briefly, 40 μL of cells cultured in DMEM-10% FBS (Thermo Fisher Scientific) were plated in 384-well Phenoplates (Perkin Elmer) and treated with R1-ICR-5 or DMSO control. After 20 hours at 37ºC/CO2 incubator, cells were fixed in 2% formaldehyde at room temperature for 15 mins, then washed in PBS (Phosphate Buffered Saline) using a Multidrop Combi (Thermo Fisher Scientific). Fixed cells were permeabilized for 15 mins at room temperature in 1xPBS/0.2% Triton X-100 (Thermo Fisher Scientific #28314), before 1hr blocking in PBS/0.5% BSA (Sigma Aldrich, A2153). After washing with PBS (Multidrop Combi), cells were incubated overnight at 4°C in PBS/BSA with anti-hRIPK1 (Cell Signaling Technology, #73271) or anti-mRIPK1 (Cell Signaling Technology, #3493) primary antibodies, in the presence of DAPI (Thermo Fisher Scientific, D3571) and Phalloidin-Alexa 633 (Thermo Fisher Scientific, A22284). After washing with PBS, cells were incubated for 1 h at room temperature in PBS/BSA plus donkey anti-rabbit Alexa 488 (Thermo Fisher Scientific, A21206). To visualize TRADD fibrillation, $L929^{Dox\text{-}FlagTRADD}$ cells were plated as described above, and protein was induced with 100ng/ml Dox 1h prior to treatment. TRADD was visualized using anti-DYKDDDDK tag (Cell Signaling Technology, #8146) and a Leica SP8 Point Scanning Confocal microscope equipped with a 63X objective. Quantification of TRADD aggregates was performed using Harmony High Content Imaging and Analysis software (Perkin Elmer).

Proximity ligation assay (PLA) and co-localisation assay

$L929^{Flag\text{-}TRADD}$ cells were treated overnight with R1-ICR-5 (1 μM). The next day, cells were treated with Doxycycline (100 ng/ml) for 2h and TNF (10 ng/ml) for 30min. Cells were fixed with 2% paraformaldehyde (Santa Cruz, # sc-281692) for 20 min, permeabilized with 0.5 % Triton x-100 for 5 min and PLA was performed according to the manufacture's protocol, using the NaveniFlex MR (Navinci Diagnostics AB, USA) kit. Primary antibodies against RIPK3 (Cell Signaling Technologies, D8J3L) and FLAG-tag (Cell Signaling Technologies, 8146) were used at a dilution of 1:500 and 1:1000 respectively, and cells were counter-stained with DAPI. Z-stacks of six to nine fields per well were acquired in the ImageXpress Micro Confocal (Molecular Devices) with an CFI Plan Fluor 40x (0.75NA) objective and analyzed with a custom module editor within MetaXpress (Molecular Devices). Each dot on the graph represents the total number of PLA foci (sum intensity projection of the FITC channel) divided by the total number of nuclei (maximum intensity projection of the DAPI channel) per field of a representative experiment of two independent repeats. Representative images of one experiment are shown as an overlay of the sum intensity projection obtained on the FITC channel and the maximum intensity projection obtained on the DAPI channel. Scale bars represent 20 μm.

Caspase activity and cell viability assays

Caspase activity was measured by DEVDase assay and was performed as previously described[101]. In brief, $1.0X10^4$ cells were plated in 96-well plates and after treatment, medium was removed, and plates were placed at -80C for few hours. Next, 20μl of DISC lysis buffer was added to each well and after 20min on ice, 180μl of DEVDase assay mix (add info) was added. Plates were incubated at room temperature for several hours and DEVDase activity was read at 380nM excitation/460nM emission. Cell viability was measured by CellTiter-GLO assay (Promega) and was performed according to the manufacturer's instructions. In brief, cells were plated in 96 well plates and treated with indicated conditions and cell survival was measured using Victor X plate reader (PerkinElmer). Drug concentrations used in both assays: Emricasan (5 μM), RIPK1 inhibitors PK68 or GSK'963 (100 nM), R1-ICR-5 (1 μM) SMAC mimetic (SM164, 100 nM) and TNF (10 ng/ml).

In vitro treatments (Cell death & signaling assays)

To measure cell death, cells were seeded in 96 well plates (#655090, Greiner) or 384 well plates (#781091, Greiner), before indicated treatments for specified times. Hoechst (0.5 µg/ml) and PI (1 µg/ml) were added and the % of dead cells was measured using the Celigo S Cell Imaging Cytometer (Nexcelom Bioscience). Cell death measurement of Naïve $CD4^+$ and $CD8^+$ T cells was performed as previously described[100]. Drug concentrations used: Cycloheximide (25 µg/mL), Doxycycline (100 ng/mL), Emricasan (1-5 µM), Enbrel (50 µg/mL), HOIPIN-8 (30 µM), mIFNβ/γ (100 ng/mL), hIFNβ (25 ng/mL), IKK2 inhibitor (TPCA-1, 250 nM), LPS (0.1-10 µg/mL), MK2 inhibitor (PF3644022, 250 nM), NIK1 inhibitor (NIK-SMI1, 1 µM), Poly(I:C) (10 µg/mL), P38 inhibitor (LY2228820, 250 nM), RIPK1 inhibitors (Nec1, PK68 and GSK'693: 100 nM), RIPK3 inhibitor (GSK'872, 10 µM), RIPK2 PROTAC (1 µM), R1-ICR-3 (1 µM), R1-ICR-5S (Non-VHL binder, 1 µM), R1-ICR-5 (Murine cells, 1 µM; Human cells, 200 nM), TAK1i (5Z-7-Oxozeaenol, 1 µM), TNFα (10 ng/mL), TPL2 inhibitor (Cot inhibitor-2, 1 µM), XIAP degrader-1 (10 µM), and zVAD (20 µM). To analyze TNFR1 and TLR3-induced inflammatory and necroptotic signaling, cells were seeded into 6-well plates overnight, before treatment and subsequent western blot or RT-qPCR analysis, as indicated. Drug concentrations used: Doxycycline (100 ng/mL), Emricasan (1 µM), Enbrel (50 µg/mL), MK2 inhibitor (PF3644022, 500 nM), SMAC mimetic (ASTX660, 1 µM), TNFα (10 ng/mL), Poly(I:C) (10 µg/mL), Riboxxol (10 µg/mL), hIFNβ (25 ng/mL), RIPK2 PROTAC (1 µM), R1-ICR-5 (Murine cells, 1 µM; Human cells, 200 nM).

In vitro irradiation

Cells were plated overnight before irradiation (AGO 250 kV X-ray machine, 1.62 Gy/min, single doses of 4 or 8 Gy). Enbrel (50µg/mL) was added 30 minutes before irradiation. R1-ICR-5 (1 µM) was added 24 hours after irradiation. Doxycycline (Dox)-inducible *shNt, shTrif* (Also known as *Ticam1*) and *shZbp1*-expressing EO771 cells were Dox-induced 36 h before irradiation. Cell death was measured 48 – 72 h after irradiation. To measure DNA damage by immunofluorescence, EO771 cells (2 x 10^3) were seeded overnight in a 96 well plate (#655090, Greiner) and subjected to single doses of irradiation, as indicated. After 30 minutes, cells were washed (PBS) and fixed (4% paraformaldehyde, 10 minutes). Cells were washed three times (PBS), incubated for 1 hour with blocking solution (0.3% Triton X100, 5% normal goat serum, 1% BSA in PBS) and then with α-γ-H2AX overnight at 4°C. Cells were washed three times with PBS and incubated with the α-rabbit secondary antibody and DAPI for 1 hour at room temperature. Cells were washed and imaged by a Zeiss 710 confocal microscope (Zeiss 40X objective). The average γ-H2AX intensity per nucleus was quantified by Fiji software. For bulk RNA-seq, EO771 cells were seeded overnight before exposure to a single fraction of 8 Gy. 48 hours later, total RNA was extracted using RNeasy kit (Qiagen).

RT-qPCR

RNA was extracted from cells using RNeasy (Qiagen) and converted to cDNA using QuantiTec Reverse Transcription Kit (Qiagen), according to manufacturer's instructions. RT-qPCR and data analysis was performed as previously described[102]. For EO771 cells, mRNA was extracted 48 h after irradiation (0, 8 Gy). The relative mRNA expression of indicated genes was measured using Taqman probes (See Key resources table and supplementary table S3 for more details).

Mass Spectrometry

Sample preparation and TMT labelling - For total proteome analysis, U937 cells were treated with DMSO or R1-ICR-3 (100nM) for 6 h by trypsin digestion and TMTpro 15-plex labelling[103]. For total proteome analysis of BMDMs, cells were treated with DMSO or R1-ICR-05 (1µM) for 5 h. Cell lysates were digested[104] and peptides were labelled with TMTpro 12-plex according to manufacturer's instructions. Basic reverse-phase peptide fractionation and LC-MS analysis - The TMTpro labelled peptides were fractionated with high-pH Reversed-Phase (RP) chromatography using the XBridge C18 column (2.1 x 150 mm, 3.5 µm, Waters) on a Dionex UltiMate 3000 HPLC system. LC-MS analysis was performed on a Dionex UltiMate 3000 UHPLC system coupled with the Orbitrap Lumos Mass Spectrometer (Thermo Fisher Scientific). Peptides were loaded onto the Acclaim PepMap 100, 100 µm

× 2 cm C18, 5 µm, trapping column at flow rate 10 µL/min and analyzed with an Acclaim PepMap (75 µm × 50 cm, 2 µm, 100 Å) C18 capillary column connected to a stainless-steel emitter on an EASY-Spray source via a PSS2 adapter (MSWIL). Mobile phase A was 0.1% formic acid and mobile phase B was 80% acetonitrile, 0.1% formic acid. For total proteome analyses, a 95 min gradient 5%-38% B was used. MS scans were acquired in the range of 375-1,500 m/z with mass resolution of 120K, AGC 4×10^5 and max IT 50 ms. Precursors were selected with the top speed mode in 3 sec cycles and isolated for HCD fragmentation with quadrupole isolation width 0.9 Th (IMAC) or 0.7 Th, collision energy at 36% at 50K or 30K resolution. Targeted precursors were dynamically excluded for further fragmentation for 30 seconds or 45 sec with 7 ppm mass tolerance. Database search and protein quantification - The mass spectra were analyzed in Proteome Discoverer 2.4 (Thermo Scientific) with the SequestHT search engine for peptide identification and quantification. The precursor and fragment ion mass tolerances were 20 ppm and 0.02 Da respectively. Spectra were searched for fully tryptic peptides with maximum 2 missed cleavages. TMTpro at N-terminus/K and Carbamidomethyl at C were selected as static modifications. Spectra were searched against reviewed UniProt Mus musculus (BMDMs) or Homo Sapiens (U937 cells) protein entries, peptide confidence was estimated with the Percolator node and peptides were filtered at q-value<0.01 based on target-decoy database search. The reporter ion quantifier node included a TMTpro quantification method with an integration window tolerance of 15 ppm. Only peptides with average reporter signal-to-noise>3 were used for quantification. Differential protein expression analysis was performed using the R package limma (v3.50.1), R version 4.1.0.

Purification of TNFR1 complex I & II

The composition of TNFR1 signaling complex I and -II was analysed as previously described[105,106]. In short, complex I was purified from cells using FLAG-hTNF (800 ng/mL) or STREP-hTNF (1 µg/mL). Cells were lysed in DISC buffer (20 mM Tris-HCl, pH 7.5, 150 mM NaCl, 2 mM EDTA, 1% Triton X-100, 10% glycerol) supplemented with cOmplete protease (Roche) and phosSTOP phosphatase (Sigma) inhibitors, and PR619 DUB inhibitor (2B Scientific, 10 µM). Lysates were harvested and clarified by rotating (20 minutes) then centrifuging (15 minutes, 14,000 rpm) at 4 °C. Untreated control samples were treated with 800ng/mL 3xFLAG-TNF or 1 µg/mL 2xSTREP-TNF, post-lysis. Complex I was purified overnight, by incubating lysates with anti-FLAG M2 (Sigma) or Strep-Tactin (IBA lifesciences) beads. Immunocomplexes were washed with DISC buffer supplemented with PR619 (10 µM), before eluting with 1X SDS sample buffer. For USP2 digestion, after the final wash, beads were additionally washed with DUB reaction buffer (50mM Tris pH 7.5 and 150nM NaCl). 20 µL DUB reaction buffer (50mM Tris pH 7.5 and 150nM NaCl) + 5mM DTT + 2uM USP2) was added to the dried beads and digestion was performed for 1 h at 37°C. Complex II was purified from cell lines harbouring a Dox-inducible FLAG-TRADD transgene, which was induced for 2 h before TE treatment. Complex II was purified from cell lysates, with anti-FLAG M2 beads (Sigma) overnight at 4°C, before washing with lysis buffer supplemented with PR619 DUB inhibitor (10 µM) and eluting with SDS sample buffer. Samples were analysed by SDS-PAGE.

Ubiquitin pulldown (TUBE assay)

Stimulation-induced ubiquitylation of indicated proteins was assessed by total ubiquitin pulldown, using GST-TUBE (Tandem Ubiquitin Binding Entities), as previously described[77]. In brief, after treatments cells were washed with ice cold PBS and lysed with DISC lysis buffer (50mM Tris pH 7.8, 150 mM NaCl, 1 mM EDTA, 1% Triton X-100, and 10% glycerol) supplemented protease and phosphatase inhibitors (as in complex-I/II), 1 mM DTT, PR619 (10 µM) and GST-TUBE (50 µg/ml; 50 µg TUBE/mg protein lysate). Lysates were cleared by centrifugation (4°C, 16000 g, 15 min) and immunocomplexes were purified by overnight rotation at 4 °C, in the presence of 20µL GSH beads (Sigma). Beads were washed four times with TUBE wash buffer (PBS and 1% Triton X-100) supplemented with PR619 (10 µM). To visualize higher order proteins, beads were split in two prior to elution, and incubated with either reducing or non-reducing sample buffer (with or without β-mercaptoethanol, respectively) to enable higher order oligomers to be visualised, by SDS-PAGE.

Immunoprecipitation and immunoblot analysis

Co-purification was conducted as previously described[107]. In brief, cells were lysed in 1% Triton lysis buffer (50mM Tris pH7.5, 150mM NaCl, 1% Triton X-100 and protease/phosphate inhibitors (Roche). Lysates were centrifuged (16000 g, 20 min) and supernatants were incubated with either α-HA or α-FLAG beads (SIGMA). Subsequently, beads were washed three times with IPPG150 wash buffer (0.1% Triton X-100, 50 mM Tris pH 7.5, 150 mM NaCl,). Beads were boiled in Laemmli buffer for 10 min and proteins were resolved by SDS-PAGE.

In vitro binding assay

N-terminal FLAG-tagged murine TRADD was amplified by PCR using pcDNA3-FLAG-*mTradd* as a template and subcloned in frame with chitin binding protein using the NdeI and EcoRI sites of pTYB1 (New England BioLabs Inc.). Transformed *E. Coli* BL21(DE3) cells were induced overnight at 15^0C with 0.1 mM IPTG to express FLAG-mTRADD-CBP fusion protein. FLAG-mTRADD was subsequently isolated by sequential purification using FLAG (M2) agarose and chitin beads followed by Intein-mediated cleavage/elution with Intein Lysis Buffer containing 50 mM DTT. Protein purity was assessed by silver staining and identity confirmed by immunoblotting with both FLAG (M2) mAb and TRADD antibodies (Cell Signaling Technology). mRIPK3 was generated by coupled *in vitro* transcription/translation reactions using HeLa extracts following synthesis of a PCR fragment which included a 5' T7 promoter, IRES and kozak sequence and a 3' poly A tail according to the application notes of the manufacturer's protocol (Thermofisher Inc.). Purified FLAG-mTRADD and mRIPK3 were incubated with either anti-FLAG (M2) conjugated agarose or alternatively, anti-RIPK3 (Cat # 15828, Cell Signaling Technology) and Protein G dynabeads in 30 mM TrisHCl, pH7.4, 150 mM NaCl, 10% glycerol, 1 % Triton X-100 overnight at 4^0C. Beads were washed with 4 x 1 ml buffer and aliquots resolved on 10 % precast TGX gels (Bio-Rad Inc.). Immunoblotting was performed using FLAG (F3165) mAb and rabbit anti-RIPK3 (Cat # 15828, Cell Signaling Technology) combined with either anti-mouse-HRP (veriblot ab131368, Abcam) or clean-blot IP detection reagent (#21230, Thermofisher) respectively. See supplementary Table S3 for primers used in PCR reactions.

Size exclusion chromatography

FLAG-mTRADD (50 ml) expressed and purified from *E. Coli* as described was resolved on a Superdex 200 increase 3.2/300 size-exclusion column in 30 mM TrisHCl, pH7.4, 150 mM NaCl, 10 % glycerol, 1% (w/v) Triton X-100 using an AKTA Pure protein purification system (Cytiva) and 100 ml fractions collected, essentially as described previously[108]. Aliquots from the indicated fractions, denatured in Laemmli sample buffer, were resolved on 18-well Criterion TGX gels and immunoblotted with FLAG (M2) mAb. The column was calibrated using a high molecular weight gel filtration calibration kit (Cytiva # 28403842).

Western blot analysis

Western blot analyses were performed as previously described[77]. Briefly, cells were lysed with DISC lysis buffer (1 M Tris pH 7.8, 5 M NaCl, 0.5 M EDTA, 40% Glycerol and 1% Triton X-100) supplemented with protease inhibitor cocktail and phosphatase inhibitors before clearing by centrifugation and quantification by Pierce™ BCA protein assay kit (ThermoFisher). Whole cell lysates were harvested with 1X SDS sample buffer (6x sample buffer: 3 ml 20% SDS, 4 ml 100% glycerol, 3 ml β-ME and 1 g bromophenol blue). To assess RIPK1 depletion *in vivo*, tumor and skin samples were collected 24 h after intra-tumoral or subcutaneous injection. Single cell suspensions were prepared from tumors as described below and from skin by homogenization, using 2.4mm bead mill tubes (ThermoFisher) and the Precellys evolution tissue homogenizer (Bertin Technologies). Lysates and homogenates were collected with RIPA buffer (10mM Tris(-HCL) pH8, 1mM EDTA, 0.5 mM EGTA, 1 % Triton, 0.1 % Sodium deoxycholate, 0.1 % SDS & 140 nM NaCl) + HALT protease & phosphatase inhibitor cocktail (ThermoFisher) before centrifugation (20000 xg, 20 mins at 4°C). All samples were boiled with Laemmli buffer (100°C, 10 min), then resolved by SDS-PAGE (NuPAGE Novex 4-12% Bis-Tris 1.0 mm gels in MOPS buffer (ThermoFisher)), transferred onto polyvinylidene difluoride (PVDF) membranes, blocked

(5% BSA or milk in TBST) and probed with indicated antibodies (See key resource table). All primary antibodies were diluted in 5% BSA-TBST + 0.01% NaN_3 and secondary antibodies diluted 1:10000 in 5 % non-fat milk-TBST. Densitometry was performed using ImageJ software.

Flow cytometry

Mammary tumors were harvested in ice-cold PBS from mice 13 days after irradiation. Tumors were mechanically dissociated with scissors and enzymatically digested (30 min, 37°C), in PBS containing Trypsin-Versene, 1 mg/ml collagenase type VI (Sigma-Aldrich), 100 µg/ml dispase (Sigma-Aldrich), 1 mg/ml DNase type I (Roche). Tumor suspensions were passed through a cell strainer (70 µm) into PBS (2% FBS & 2 mM EDTA), before centrifugation (1200 rpm, 5 min, 4°C). Pellets were resuspended in PBS-FBS 2% + Fc block (CD16/CD32) for 10 min (4°C), before surface staining (30 min, 4°C). To detect intracellular cytokines and surface CD107a, cells were restimulated in IMDM containing Golgi Plug (BD Biosciences), 100 ng/ml PMA (Thermo Fisher Scientific) and 1 µg/ml ionomycin (Thermo Fisher Scientific) (4 h at 37°C). After, cells were fixed by IC fixation buffer (Thermo Fisher Scientific), permeabilised with permeabilization buffer (Thermo Fisher Scientific) and stained with IFN-γ, TNFα, Granzyme B, Foxp3 and Ki67 antibodies. Flow cytometric analyses were carried out with the LSR II FACSymphony A5 (BD Biosciences) with FACSDiva software. Data were analysed with FlowJo V.10 software. The full list of antibodies used in this study can be found in the key resources table.

In vivo tumor treatments

For tumor treatments, 5 – 6 weeks old female C57BL/6J mice were purchased from Charles River and were enrolled in the study post an acclimatization period of at least one week. Mice were injected in the 4th right mammary fat pad with 1x10^5 EO771 cells in RPMI supplemented with 10% FBS, 5 mM Hepes, penicillin/streptomycin, and containing 50% Matrigel matrix (Corning). Tumor growth was monitored twice a week using a digital caliper, and volumes (0.52 x length x width x width) were expressed in mm^3. Mice were culled before the average tumor size reached 15 mm. Tumor treatment was started when tumors reached an average of 50 – 100 mm^3. Tumors were irradiated with the Small Animal Radiotherapy Research Platform (SARRP, Xstrahl), employing a parallel opposed beam arrangement with a 10 mm x 10 mm collimator for each beam. In all experiments, beams were equally weighted, and the radiation dosage was 4 or 8 Gy, administered in a single fraction. R1-ICR-5 was solubilized in captisol (Ligand's Pharmaceutical) and administered by intra-tumoral injection (40 µg/injection) at indicated intervals (See Fig. 6,7 and Suppl. Fig. S6). Anti-IgG2a, anti-CTLA-4 and anti-PD-1 antibodies were injected intraperitoneally (200µg) at indicated intervals (See Fig. 6 & 7). (Sourced from 2B Scientific, see key resources table). Response rates of treated mice were classified as complete response (tumor free for at least 2 months), partial response (tumor volume drops to <100 mm^3) and progression (no response to treatment). *P* values were calculated using the Chi-square test, comparing progression (those that progressed after treatment) against response (those that showed both complete and partial responses to treatment). To assess immune memory, mice that were tumor free for at least two months (cured mice) were re-challenged together with naïve mice by injecting EO771 in the 4th left mammary fat pad, as described above. To measure RIPK1 depletion by WB (24h after a single injection) and IHC analysis, R1-ICR-5 was injected intra-tumorally on days 0, 2, 4 and 6 and samples were collected 24 hours post final injection. To measure CASP3 cleavage by IHC, EO771 tumors were irradiated and treated with R1-ICR-5 every 3 days as described above. Tumors were harvested 13 days after irradiation and fixed before staining.

Chemical and genetic skin inflammation models

The skin injection experiments were performed as previously described[77]. Briefly, mice were injected subcutaneously in the flank with 100 µL of SM (ASTX660, 3 mM) and E (Emricasan, 1 mM) or TNF (1 µg) and TBK1i (MRT67307, 150 µg), combined with R1-ICR-3 (10 mM), R1-ICR-5 (10 mM) or vehicle. Mice were culled 3 days after the injection and the regions of injections were macroscopically assessed. Hair removal cream was used to remove the fur in the lesion area before taking a skin biopsy. Biopsies were processed as previously reported[77]. Genetically induced skin inflammation models employed

UBC-CreRT^{T2} mice to locally induce loss of *Casp8*$^{fl/fl}$, *Ripk1*$^{fl/fl}$ or *Casp8*$^{fl/fl}$/*Ripk1*$^{fl/fl}$ on the nape, by topical treatment with 4-OHT (250 µg per dose) on d0 and d3. Skin biopsies were harvested on d23 and were processed and analyzed as below.

Immunohistochemistry

For IHC analyses, staining was carried on the Dako Autostainer Link48 platform (Agilent Technologies) with epitope retrieval carried out using the Dako PT Link module at 97°c for 20 minutes using Dako Target Retrieval Solution pH9 (Agilent, K800421-2) for RIPK1 and TRS pH6 (Agilent, K800521-2) for cleaved CASP3, according to manufacturer's instructions. Endogenous peroxidases were blocked using Dako REAL peroxidase block (Agilent, S202386-2) then primary antibody RIPK1 (D94C12, Cell Signaling #3493) was diluted 1/50 and applied (60min at room temperature and detected using Dako rabbit EnVision polymer-HRP (Agilent,K400311-2)). The reaction was visualized using Dako DAB+ (Agilent, K346811-2) and nuclei counterstained using Dako FLEX haematoxylin (Agilent, K800821-2) according to manufacturer's instructions. CASP 3 cleavage was measured with anti-Cleaved Caspase 3 (ASP175) primary antibody (Cell Signaling #9664, clone 5A1E, 1/100 dilution). Detection using Rabbit ImmPRESS polymer-HRP (Vector Laboratories, MP-7401-50).

Quantification and statistical analysis

Survival analyses

For TCGA patient data analysis, RIPK1 DNA copy number and RNA-seq data from ACC, BRCA, CESC, STAD, LIHC, LUSC, SKCM, SARC, and UCEC patients of TCGA were downloaded from cBioPortal (https://www.cbioportal.org/). To analyse the SCAN-B patient data, we obtained RNA-sequencing and patient survival data from the GEO database using the accession ID GSE96058. The R package org.Hs.eg.db (v3.7.0) was utilized to map HGNC gene symbols to EntrezIDs. Survival differences among groups were evaluated using the Kaplan-Meier method, and the p-value was determined using the log-rank test, using the R package survival (v3.5.5).

Gene set enrichment analyses (GSEA)

Using the ConsensusTME R package (v0.0.1.9000) on the SCAN-B dataset, patient groups were categorized by assessing the expression differences of RIPK1 and the levels of NK cell infiltration. Gene Set Enrichment Analysis (GSEA)[109] was then carried out on these groups to investigate the differential expression of immune response gene sets. These gene sets were obtained from the hallmark gene set collection of The Molecular Signatures Database (MSigDB)[110].

Bulk RNA-seq analysis

Total RNA sequencing was performed by Azenta (Genewiz), employing Illumina NovaSeq, 2 x 150 base pairs as sequencing configuration. Samples and genes were clustered using agglomerative hierarchical clustering with '1-Pearson correlation coefficient' as distance measure followed by complete-linkage clustering.

Histopathological assessment of murine skin samples

Histopathological sample analysis was carried out as previously described[77]. Skin sections were scanned at x40 (0.23 µm/pixel) using a NanoZoomer-XR Hamamatsu Photonics (Japan). The analysis of digitized skin samples involved assessment of the vicissitudes in epidermal and dermal region of the skin identifiable on haematoxylin and eosin (H&E) stained samples. First, a Histopathological (multivariate) Lesion Score (HLS) was used to assess the proportion and severity of histopathological changes. This assessment was performed on the entire length of the skin sample (epidermal and immediate dermal level). To increase precision of the assessment, each sample was divided using a grid with equal size of fields of view (FOV) (0.04mm^2/800µm perimeter). Each FOV was assessed for presence of regular epidermis or any pathological changes to regular epidermis and dermis. A final calculation took into account the proportion [%] of given skin lesions within each sample, multiplied by

a power score ranging from 0 to 4. Score 0 was associated with regular epidermis with no changes to any of the strata. Score 1 with thickening of the epidermis represented by any of the strata. Score 2 with epidermal erosion (partial loss of the epidermis), with the stratum basale left intact. Score 3 with ulcer-loss of epidermis, including the stratum basale. Score 4 with deep ulceration of the epidermis and subepidermal dermis. The final score (HLS) indicates the severity following the formula: [(0x % Score 0) + (1× % Score 1) + (2× % Score 2) + (3× % Score 3) + (4x % Score 4)]. The lowest possible HLS is '0' which is equal to 100% of normal/regular epidermis in the whole sample, and a maximum HLS of '400' equal to 100% of deep ulceration.

Statistical analysis

Graphs and statistical analyses were generated and performed using GraphPad Prism V9.4.1. The statistical analysis performed for each data set is described in the corresponding figure legend. Error bars indicate standard deviation (SD). No data were excluded.

References

1 Medzhitov, R. Origin and physiological roles of inflammation. *Nature* **454**, 428-435, doi:10.1038/nature07201 (2008).

2 Pasparakis, M. & Vandenabeele, P. Necroptosis and its role in inflammation. *Nature* **517**, 311-320, doi:10.1038/nature14191 (2015).

3 Rothlin, C. V. & Ghosh, S. Lifting the innate immune barriers to antitumor immunity. *J Immunother Cancer* **8**, doi:10.1136/jitc-2020-000695 (2020).

4 Annibaldi, A. & Meier, P. Checkpoints in TNF-Induced Cell Death: Implications in Inflammation and Cancer. *Trends Mol Med* **24**, 49-65, doi:10.1016/j.molmed.2017.11.002 (2018).

5 Legrand, A. J., Konstantinou, M., Goode, E. F. & Meier, P. The Diversification of Cell Death and Immunity: Memento Mori. *Mol Cell* **76**, 232-242, doi:10.1016/j.molcel.2019.09.006 (2019).

6 Peltzer, N. & Walczak, H. Cell Death and Inflammation - A Vital but Dangerous Liaison. *Trends Immunol* **40**, 387-402, doi:10.1016/j.it.2019.03.006 (2019).

7 Yatim, N., Cullen, S. & Albert, M. L. Dying cells actively regulate adaptive immune responses. *Nat Rev Immunol* **17**, 262-275, doi:10.1038/nri.2017.9 (2017).

8 Liu, L. & Lalaoui, N. 25 years of research put RIPK1 in the clinic. *Seminars in cell & developmental biology* **109**, 86-95, doi:10.1016/j.semcdb.2020.08.007 (2021).

9 Orozco, S. *et al.* RIPK1 both positively and negatively regulates RIPK3 oligomerization and necroptosis. *Cell Death Differ* **21**, 1511-1521, doi:10.1038/cdd.2014.76 (2014).

10 Weinlich, R. & Green, D. R. The two faces of receptor interacting protein kinase-1. *Mol Cell* **56**, 469-480, doi:10.1016/j.molcel.2014.11.001 (2014).

11 Dannappel, M. *et al.* RIPK1 maintains epithelial homeostasis by inhibiting apoptosis and necroptosis. *Nature*, doi:10.1038/nature13608 (2014).

12 Dillon, C. P. *et al.* RIPK1 blocks early postnatal lethality mediated by caspase-8 and RIPK3. *Cell* **157**, 1189-1202, doi:10.1016/j.cell.2014.04.018 (2014).

13 Kelliher, M. A. *et al.* The death domain kinase RIP mediates the TNF-induced NF-kappaB signal. *Immunity.* **8**, 297 (1998).

14 Rickard, J. A. *et al.* RIPK1 regulates RIPK3-MLKL-driven systemic inflammation and emergency hematopoiesis. *Cell* **157**, 1175-1188, doi:10.1016/j.cell.2014.04.019 (2014).

15 Takahashi, N. *et al.* RIPK1 ensures intestinal homeostasis by protecting the epithelium against apoptosis. *Nature* **513**, 95-99, doi:10.1038/nature13706 (2014).

16 Lin, J. *et al.* RIPK1 counteracts ZBP1-mediated necroptosis to inhibit inflammation. *Nature* **540**, 124-128, doi:10.1038/nature20558 (2016).

17 Newton, K. *et al.* RIPK1 inhibits ZBP1-driven necroptosis during development. *Nature* **540**, 129-133, doi:10.1038/nature20559 (2016).

18 Berger, S. B. *et al.* Cutting Edge: RIP1 kinase activity is dispensable for normal development but is a key regulator of inflammation in SHARPIN-deficient mice. *J Immunol* **192**, 5476-5480, doi:10.4049/jimmunol.1400499 (2014).

19 Kondylis, V. *et al.* NEMO Prevents Steatohepatitis and Hepatocellular Carcinoma by Inhibiting RIPK1 Kinase Activity-Mediated Hepatocyte Apoptosis. *Cancer Cell* **28**, 830, doi:10.1016/j.ccell.2015.11.007 (2015).

20 Vlantis, K. *et al.* NEMO Prevents RIP Kinase 1-Mediated Epithelial Cell Death and Chronic Intestinal Inflammation by NF-kappaB-Dependent and -Independent Functions. *Immunity* **44**, 553-567, doi:10.1016/j.immuni.2016.02.020 (2016).
21 Duprez, L. *et al.* RIP kinase-dependent necrosis drives lethal systemic inflammatory response syndrome. *Immunity* **35**, 908-918, doi:S1074-7613(11)00508-5 [pii] 10.1016/j.immuni.2011.09.020 (2011).
22 Polykratis, A. *et al.* A20 prevents inflammasome-dependent arthritis by inhibiting macrophage necroptosis through its ZnF7 ubiquitin-binding domain. *Nat Cell Biol* **21**, 731-742, doi:10.1038/s41556-019-0324-3 (2019).
23 van Loo, G. & Bertrand, M. J. M. Death by TNF: a road to inflammation. *Nat Rev Immunol*, 1-15, doi:10.1038/s41577-022-00792-3 (2022).
24 Garcia-Carbonell, R. *et al.* Elevated A20 promotes TNF-induced and RIPK1-dependent intestinal epithelial cell death. *Proc Natl Acad Sci U S A* **115**, E9192-E9200, doi:10.1073/pnas.1810584115 (2018).
25 Mifflin, L., Ofengeim, D. & Yuan, J. Receptor-interacting protein kinase 1 (RIPK1) as a therapeutic target. *Nat Rev Drug Discov* **19**, 553-571, doi:10.1038/s41573-020-0071-y (2020).
26 Cucolo, L. *et al.* The interferon-stimulated gene RIPK1 regulates cancer cell intrinsic and extrinsic resistance to immune checkpoint blockade. *Immunity* **55**, 671-685 e610, doi:10.1016/j.immuni.2022.03.007 (2022).
27 Kondylis, V., Kumari, S., Vlantis, K. & Pasparakis, M. The interplay of IKK, NF-kappaB and RIPK1 signaling in the regulation of cell death, tissue homeostasis and inflammation. *Immunol Rev* **277**, 113-127, doi:10.1111/imr.12550 (2017).
28 Bertrand, M. J. & Vandenabeele, P. RIP1's function in NF-kappaB activation: from master actor to onlooker. *Cell Death Differ* **17**, 379-380, doi:10.1038/cdd.2009.213 (2010).
29 Xia, Y., Shen, S. & Verma, I. M. NF-kappaB, an active player in human cancers. *Cancer Immunol Res* **2**, 823-830, doi:10.1158/2326-6066.CIR-14-0112 (2014).
30 Betzler, A. C. *et al.* NF-kappaB and Its Role in Checkpoint Control. *Int J Mol Sci* **21**, doi:10.3390/ijms21113949 (2020).
31 Smyth, P., Sessler, T., Scott, C. J. & Longley, D. B. FLIP(L): the pseudo-caspase. *FEBS J* **287**, 4246-4260, doi:10.1111/febs.15260 (2020).
32 Newton, K. *et al.* Cleavage of RIPK1 by caspase-8 is crucial for limiting apoptosis and necroptosis. *Nature* **574**, 428-431, doi:10.1038/s41586-019-1548-x (2019).
33 Oberst, A. *et al.* Catalytic activity of the caspase-8-FLIP(L) complex inhibits RIPK3-dependent necrosis. *Nature* **471**, 363-367, doi:10.1038/nature09852 (2011).
34 O'Donnell, M. A. *et al.* Caspase 8 inhibits programmed necrosis by processing CYLD. *Nat Cell Biol* **13**, 1437-1442, doi:ncb2362 [pii] 10.1038/ncb2362 (2011).
35 Tummers, B. *et al.* Caspase-8-Dependent Inflammatory Responses Are Controlled by Its Adaptor, FADD, and Necroptosis. *Immunity* **52**, 994-1006 e1008, doi:10.1016/j.immuni.2020.04.010 (2020).
36 Tao, P. *et al.* A dominant autoinflammatory disease caused by non-cleavable variants of RIPK1. *Nature* **577**, 109-114, doi:10.1038/s41586-019-1830-y (2020).
37 Schwarzer, R., Jiao, H., Wachsmuth, L., Tresch, A. & Pasparakis, M. FADD and Caspase-8 Regulate Gut Homeostasis and Inflammation by Controlling MLKL- and GSDMD-

Mediated Death of Intestinal Epithelial Cells. *Immunity* **52**, 978-993 e976, doi:10.1016/j.immuni.2020.04.002 (2020).
38 Laurien, L. *et al.* Autophosphorylation at serine 166 regulates RIP kinase 1-mediated cell death and inflammation. *Nature communications* **11**, 1747, doi:10.1038/s41467-020-15466-8 (2020).
39 Lalaoui, N. *et al.* Mutations that prevent caspase cleavage of RIPK1 cause autoinflammatory disease. *Nature* **577**, 103-108, doi:10.1038/s41586-019-1828-5 (2020).
40 Jiao, H. *et al.* Z-nucleic-acid sensing triggers ZBP1-dependent necroptosis and inflammation. *Nature* **580**, 391-395, doi:10.1038/s41586-020-2129-8 (2020).
41 Priem, D. *et al.* A20 protects cells from TNF-induced apoptosis through linear ubiquitin-dependent and -independent mechanisms. *Cell Death Dis* **10**, 692, doi:10.1038/s41419-019-1937-y (2019).
42 Kondylis, V. & Pasparakis, M. RIP Kinases in Liver Cell Death, Inflammation and Cancer. *Trends Mol Med* **25**, 47-63, doi:10.1016/j.molmed.2018.10.007 (2019).
43 Cuchet-Lourenco, D. *et al.* Biallelic RIPK1 mutations in humans cause severe immunodeficiency, arthritis, and intestinal inflammation. *Science* **361**, 810-813, doi:10.1126/science.aar2641 (2018).
44 Vlantis, K. *et al.* NEMO Prevents RIP Kinase 1-Mediated Epithelial Cell Death and Chronic Intestinal Inflammation by NF-kappaB-Dependent and -Independent Functions. *Immunity* **44**, 553-567, doi:10.1016/j.immuni.2016.02.020 (2016).
45 Kaiser, W. J. *et al.* RIP1 suppresses innate immune necrotic as well as apoptotic cell death during mammalian parturition. *Proc Natl Acad Sci U S A* **111**, 7753-7758, doi:10.1073/pnas.1401857111 (2014).
46 Yatim, N. *et al.* RIPK1 and NF-kappaB signaling in dying cells determines cross-priming of CD8(+) T cells. *Science* **350**, 328-334, doi:10.1126/science.aad0395 (2015).
47 Meier, P., Legrand, A. J., Adam, D. & Silke, J. Immunogenic cell death in cancer: targeting necroptosis to induce antitumour immunity. *Nat Rev Cancer*, doi:10.1038/s41568-024-00674-x (2024).
48 Chaouhan, H. S. *et al.* Necroptosis: A Pathogenic Negotiator in Human Diseases. *Int J Mol Sci* **23**, doi:10.3390/ijms232112714 (2022).
49 Tummers, B. & Green, D. R. The evolution of regulated cell death pathways in animals and their evasion by pathogens. *Physiol Rev* **102**, 411-454, doi:10.1152/physrev.00002.2021 (2022).
50 Aaes, T. L. *et al.* Vaccination with Necroptotic Cancer Cells Induces Efficient Anti-tumor Immunity. *Cell reports* **15**, 274-287, doi:10.1016/j.celrep.2016.03.037 (2016).
51 Orozco, S. L. *et al.* RIPK3 Activation Leads to Cytokine Synthesis that Continues after Loss of Cell Membrane Integrity. *Cell Rep* **28**, 2275-2287.e2275, doi:10.1016/j.celrep.2019.07.077 (2019).
52 Snyder, A. G. *et al.* Intratumoral activation of the necroptotic pathway components RIPK1 and RIPK3 potentiates antitumor immunity. *Sci Immunol* **4**, doi:10.1126/sciimmunol.aaw2004 (2019).
53 Workenhe, S. T. *et al.* De novo necroptosis creates an inflammatory environment mediating tumor susceptibility to immune checkpoint inhibitors. *Communications biology* **3**, 645, doi:10.1038/s42003-020-01362-w (2020).

54 Parker, B. S., Rautela, J. & Hertzog, P. J. Antitumour actions of interferons: implications for cancer therapy. *Nat Rev Cancer* **16**, 131-144, doi:10.1038/nrc.2016.14 (2016).
55 Hou, J. *et al.* Discovery of potent necroptosis inhibitors targeting RIPK1 kinase activity for the treatment of inflammatory disorder and cancer metastasis. *Cell Death Dis* **10**, 493, doi:10.1038/s41419-019-1735-6 (2019).
56 Beal, A. M., Bertin, J. & Reilly, M. A. Use of RIP1 Kinase Small-Molecule Inhibitors in Studying Necroptosis. *Methods Mol Biol* **1857**, 109-124, doi:10.1007/978-1-4939-8754-2_11 (2018).
57 Bekes, M., Langley, D. R. & Crews, C. M. PROTAC targeted protein degraders: the past is prologue. *Nat Rev Drug Discov* **21**, 181-200, doi:10.1038/s41573-021-00371-6 (2022).
58 Diehl, C. J. & Ciulli, A. Discovery of small molecule ligands for the von Hippel-Lindau (VHL) E3 ligase and their use as inhibitors and PROTAC degraders. *Chem Soc Rev* **51**, 8216-8257, doi:10.1039/d2cs00387b (2022).
59 Crew, A. P. *et al.* Identification and Characterization of Von Hippel-Lindau-Recruiting Proteolysis Targeting Chimeras (PROTACs) of TANK-Binding Kinase 1. *J Med Chem* **61**, 583-598, doi:10.1021/acs.jmedchem.7b00635 (2018).
60 Meylan, E. *et al.* RIP1 is an essential mediator of Toll-like receptor 3-induced NF-kappa B activation. *Nat Immunol* **5**, 503-507, doi:10.1038/ni1061 (2004).
61 Wong, W. W. *et al.* RIPK1 is not essential for TNFR1-induced activation of NF-kappaB. *Cell Death Differ* **17**, 482-487, doi:cdd2009178 [pii]
10.1038/cdd.2009.178 (2010).
62 Michallet, M. C. *et al.* TRADD protein is an essential component of the RIG-like helicase antiviral pathway. *Immunity* **28**, 651-661, doi:S1074-7613(08)00154-4 [pii]
10.1016/j.immuni.2008.03.013 (2008).
63 Menon, M. B. & Gaestel, M. MK2-TNF-Signaling Comes Full Circle. *Trends Biochem Sci* **43**, 170-179, doi:10.1016/j.tibs.2017.12.002 (2018).
64 Vanlangenakker, N., Bertrand, M. J., Bogaert, P., Vandenabeele, P. & Vanden Berghe, T. TNF-induced necroptosis in L929 cells is tightly regulated by multiple TNFR1 complex I and II members. *Cell Death Dis* **2**, e230, doi:10.1038/cddis.2011.111 (2011).
65 Kearney, C. J., Cullen, S. P., Clancy, D. & Martin, S. J. RIPK1 can function as an inhibitor rather than an initiator of RIPK3-dependent necroptosis. *FEBS J* **281**, 4921-4934, doi:10.1111/febs.13034 (2014).
66 Wang, L., Chang, X., Feng, J., Yu, J. & Chen, G. TRADD Mediates RIPK1-Independent Necroptosis Induced by Tumor Necrosis Factor. *Front Cell Dev Biol* **7**, 393, doi:10.3389/fcell.2019.00393 (2019).
67 Moujalled, D. M. *et al.* TNF can activate RIPK3 and cause programmed necrosis in the absence of RIPK1. *Cell Death Dis* **4**, e465, doi:10.1038/cddis.2012.201 (2013).
68 Li, J. *et al.* The RIP1/RIP3 necrosome forms a functional amyloid signaling complex required for programmed necrosis. *Cell* **150**, 339-350, doi:10.1016/j.cell.2012.06.019 (2012).
69 Dondelinger, Y., Hulpiau, P., Saeys, Y., Bertrand, M. J. & Vandenabeele, P. An evolutionary perspective on the necroptotic pathway. *Trends Cell Biol*, doi:10.1016/j.tcb.2016.06.004 (2016).

70 Ren, J. *et al.* The RIP3-RIP1-NF-kappaB signaling axis is dispensable for necroptotic cells to elicit cross-priming of CD8(+) T cells. *Cell Mol Immunol* **14**, 639-642, doi:10.1038/cmi.2017.31 (2017).
71 Jiao, H. *et al.* ADAR1 averts fatal type I interferon induction by ZBP1. *Nature* **607**, 776-783, doi:10.1038/s41586-022-04878-9 (2022).
72 O'Connell, R. M., Taganov, K. D., Boldin, M. P., Cheng, G. & Baltimore, D. MicroRNA-155 is induced during the macrophage inflammatory response. *Proc Natl Acad Sci U S A* **104**, 1604-1609, doi:10.1073/pnas.0610731104 (2007).
73 Zhang, N., Yuan, W., Fan, J. S. & Lin, Z. Structure of the C-terminal domain of TRADD reveals a novel fold in the death domain superfamily. *Sci Rep* **7**, 7073, doi:10.1038/s41598-017-07348-9 (2017).
74 Park, Y. C. *et al.* A novel mechanism of TRAF signaling revealed by structural and functional analyses of the TRADD-TRAF2 interaction. *Cell* **101**, 777-787, doi:10.1016/s0092-8674(00)80889-2 (2000).
75 Fucikova, J. *et al.* Detection of immunogenic cell death and its relevance for cancer therapy. *Cell Death Dis* **11**, 1013, doi:10.1038/s41419-020-03221-2 (2020).
76 Anderton, H., Rickard, J. A., Varigos, G. A., Lalaoui, N. & Silke, J. Inhibitor of Apoptosis Proteins (IAPs) Limit RIPK1-Mediated Skin Inflammation. *J Invest Dermatol* **137**, 2371-2379, doi:10.1016/j.jid.2017.05.031 (2017).
77 Garcia, L. R. *et al.* Ubiquitylation of MLKL at lysine 219 positively regulates necroptosis-induced tissue injury and pathogen clearance. *Nature communications* **12**, 3364, doi:10.1038/s41467-021-23474-5 (2021).
78 Xu, D. *et al.* TBK1 Suppresses RIPK1-Driven Apoptosis and Inflammation during Development and in Aging. *Cell* **174**, 1477-1491 e1419, doi:10.1016/j.cell.2018.07.041 (2018).
79 Lafont, E. *et al.* TBK1 and IKKepsilon prevent TNF-induced cell death by RIPK1 phosphorylation. *Nat Cell Biol* **20**, 1389-1399, doi:10.1038/s41556-018-0229-6 (2018).
80 Taft, J. *et al.* Human TBK1 deficiency leads to autoinflammation driven by TNF-induced cell death. *Cell* **184**, 4447-4463 e4420, doi:10.1016/j.cell.2021.07.026 (2021).
81 Bonnard, M. *et al.* Deficiency of T2K leads to apoptotic liver degeneration and impaired NF-kappaB-dependent gene transcription. *EMBO J* **19**, 4976-4985, doi:10.1093/emboj/19.18.4976 (2000).
82 Clark, K. *et al.* Novel cross-talk within the IKK family controls innate immunity. *Biochem J* **434**, 93-104, doi:10.1042/BJ20101701 (2011).
83 Green, D. R. Another face of RIPK1. *EMBO Rep* **16**, 674-675, doi:10.15252/embr.201540470 (2015).
84 Clucas, J. & Meier, P. Roles of RIPK1 as a stress sentinel coordinating cell survival and immunogenic cell death. *Nat Rev Mol Cell Biol* **24**, 835-852, doi:10.1038/s41580-023-00623-w (2023).
85 Ea, C. K., Deng, L., Xia, Z. P., Pineda, G. & Chen, Z. J. Activation of IKK by TNFalpha requires site-specific ubiquitination of RIP1 and polyubiquitin binding by NEMO. *Mol Cell* **22**, 245-257, doi:10.1016/j.molcel.2006.03.026 (2006).
86 Upton, J. W., Kaiser, W. J. & Mocarski, E. S. DAI/ZBP1/DLM-1 complexes with RIP3 to mediate virus-induced programmed necrosis that is targeted by murine

cytomegalovirus vIRA. *Cell Host Microbe* **11**, 290-297, doi:S1931-3128(12)00058-3 [pii]
10.1016/j.chom.2012.01.016 (2012).
87 Kaiser, W. J. *et al.* Toll-like receptor 3-mediated necrosis via TRIF, RIP3, and MLKL. *J Biol Chem* **288**, 31268-31279, doi:10.1074/jbc.M113.462341 (2013).
88 Galluzzi, L., Aryankalayil, M. J., Coleman, C. N. & Formenti, S. C. Emerging evidence for adapting radiotherapy to immunotherapy. *Nat Rev Clin Oncol*, doi:10.1038/s41571-023-00782-x (2023).
89 Chen, D. S. & Mellman, I. Oncology meets immunology: the cancer-immunity cycle. *Immunity* **39**, 1-10, doi:10.1016/j.immuni.2013.07.012 (2013).
90 Vredevoogd, D. W. *et al.* Augmenting Immunotherapy Impact by Lowering Tumor TNF Cytotoxicity Threshold. *Cell* **178**, 585-599 e515, doi:10.1016/j.cell.2019.06.014 (2019).
91 Kearney, C. J. *et al.* Tumor immune evasion arises through loss of TNF sensitivity. *Sci Immunol* **3**, doi:10.1126/sciimmunol.aar3451 (2018).
92 Manguso, R. T. *et al.* In vivo CRISPR screening identifies Ptpn2 as a cancer immunotherapy target. *Nature* **547**, 413-418, doi:10.1038/nature23270 (2017).
93 Baskar, R., Lee, K. A., Yeo, R. & Yeoh, K. W. Cancer and radiation therapy: current advances and future directions. *Int J Med Sci* **9**, 193-199, doi:10.7150/ijms.3635 (2012).
94 Bianchini, G., Balko, J. M., Mayer, I. A., Sanders, M. E. & Gianni, L. Triple-negative breast cancer: challenges and opportunities of a heterogeneous disease. *Nat Rev Clin Oncol* **13**, 674-690, doi:10.1038/nrclinonc.2016.66 (2016).
95 Morad, G., Helmink, B. A., Sharma, P. & Wargo, J. A. Hallmarks of response, resistance, and toxicity to immune checkpoint blockade. *Cell* **184**, 5309-5337, doi:10.1016/j.cell.2021.09.020 (2021).
96 Prado-Acosta, M. *et al.* Inhibition of RIP1 improves immune reconstitution and reduces GVHD mortality while preserving graft-versus-leukemia effects. *Sci Transl Med* **15**, eadf8366, doi:10.1126/scitranslmed.adf8366 (2023).
97 Jumper, J. *et al.* Highly accurate protein structure prediction with AlphaFold. *Nature* **596**, 583-589, doi:10.1038/s41586-021-03819-2 (2021).
98 Perez-Riverol, Y. *et al.* The PRIDE database resources in 2022: a hub for mass spectrometry-based proteomics evidences. *Nucleic Acids Res* **50**, D543-D552, doi:10.1093/nar/gkab1038 (2022).
99 Cotsiki, M. *et al.* Simian virus 40 large T antigen targets the spindle assembly checkpoint protein Bub1. *Proc Natl Acad Sci U S A* **101**, 947-952, doi:10.1073/pnas.0308006100 (2004).
100 Blanchett, S., Dondelinger, Y., Barbarulo, A., Bertrand, M. J. M. & Seddon, B. Phosphorylation of RIPK1 serine 25 mediates IKK dependent control of extrinsic cell death in T cells. *Front Immunol* **13**, 1067164, doi:10.3389/fimmu.2022.1067164 (2022).
101 Jaco, I. *et al.* MK2 Phosphorylates RIPK1 to Prevent TNF-Induced Cell Death. *Mol Cell* **66**, 698-710 e695, doi:10.1016/j.molcel.2017.05.003 (2017).
102 Feltham, R. *et al.* Mind Bomb Regulates Cell Death during TNF Signaling by Suppressing RIPK1's Cytotoxic Potential. *Cell Rep* **23**, 470-484, doi:10.1016/j.celrep.2018.03.054 (2018).

103 Sialana, F. J. *et al.* SimPLIT: Simplified Sample Preparation for Large-Scale Isobaric Tagging Proteomics. *J Proteome Res* **21**, 1842-1856, doi:10.1021/acs.jproteome.2c00092 (2022).
104 Cutler, J. A. *et al.* Integrative phosphoproteome and interactome analysis of the role of Ubash3b in BCR-ABL signaling. *Leukemia* **34**, 301-305, doi:10.1038/s41375-019-0535-4 (2020).
105 Ciuffa, R. *et al.* Novel biochemical, structural, and systems insights into inflammatory signaling revealed by contextual interaction proteomics. *Proc Natl Acad Sci U S A* **119**, e2117175119, doi:10.1073/pnas.2117175119 (2022).
106 Annibaldi, A. *et al.* Ubiquitin-Mediated Regulation of RIPK1 Kinase Activity Independent of IKK and MK2. *Mol Cell* **69**, 566-580 e565, doi:10.1016/j.molcel.2018.01.027 (2018).
107 Tenev, T. *et al.* The Ripoptosome, a signaling platform that assembles in response to genotoxic stress and loss of IAPs. *Mol Cell* **43**, 432-448, doi:S1097-2765(11)00420-5 [pii]
10.1016/j.molcel.2011.06.006 (2011).
108 Cain, K. *et al.* Apaf-1 oligomerizes into biologically active approximately 700-kDa and inactive approximately 1.4-MDa apoptosome complexes. *J Biol Chem* **275**, 6067-6070 (2000).
109 Mootha, V. K. *et al.* PGC-1alpha-responsive genes involved in oxidative phosphorylation are coordinately downregulated in human diabetes. *Nat Genet* **34**, 267-273, doi:10.1038/ng1180 (2003).
110 Liberzon, A. *et al.* The Molecular Signatures Database (MSigDB) hallmark gene set collection. *Cell Syst* **1**, 417-425, doi:10.1016/j.cels.2015.12.004 (2015).

KEY RESOURCES TABLE (Please see below)

REAGENT or RESOURCE	SOURCE	IDENTIFIER
Antibodies		
α-cleaved-caspase-3	Cell Signaling Technology	Cat #9664S
α-phospho-ERK1/2	Cell Signaling Technology	Cat#9101S
α-FLAG	Cell Signaling Technology	Cat#8146
α-γH2AX	Cell Signaling Technology	Cat#9718P
α-IKKβ	Cell Signaling Technology	Cat#8943S
α-phospho-IKK α/β	Cell Signaling Technology	Cat#2697S
α-ISG15	Cell Signaling Technology	Cat#2743
α-MK2	Cell Signaling Technology	Cat#3042
α-phospho-MK2	Cell Signaling Technology	Cat#3007
α-p38	Cell Signaling Technology	Cat#9212
α-phospho-p38	Cell Signaling Technology	Cat#4511
α-p65	Cell Signaling Technology	Cat#8242s
α-phospho-p65	Cell Signaling Technology	Cat#3033
α-TRADD	Cell Signaling Technology	Cat#3694S
α-TRAF2	Cell Signaling Technology	Cat#4724S
α-phospho-mRIPK3 T231/S232	Cell Signaling Technology	Cat#91702
α-mouse RIPK1 N-terminal	Cell Signaling Technology	Cat#3493
α-human RIPK1 N-terminal	Cell Signaling Technology	Cat#73271
α-mouse RIPK2	Cell Signaling Technology	Cat#4142S
α-mouse RIPK2	Cell Signaling Technology	Cat#4928
α-mouse RIPK3	Cell Signaling Technology	Cat#15828
α-human RIPK3	Cell Signaling Technology	Cat#13526S
α-TrkA	Cell Signaling Technology	Cat#2505S
α-B-raf	Santa Cruz Biotechnology	Cat#sc-5284
α-IkBa	Santa Cruz Biotechnology	Cat#sc-371

α-Ubiquitin	Santa Cruz Biotechnology	Cat#sc-8017
α-phospho- MLKL S345	Abcam	Cat#ab196436
α−TNFR1	Abcam	Cat#19139
α-RIPK1	BD Bioscience	Cat#610459
α-RIPK2	BD Bioscience	Cat#612348
α-MLKL	Millipore	Cat#MABC604
α-ZBP1	Adipogen	Cat#AG-20B0010-C100
α-FADD	Assay designs	Cat#AAM-212
α-HOIP	Bethyl laboratories	Cat#A303-560A
α-Sharpin	Proteintech	Cat#14626-1-AP
α-ERK1/2	Gift from Prof. Chris Marshall	N/A
α-cIAP1	Enzo	Cat#ALX-803-335-C100
α-mouse IgG (H+L)-HRP	Jackson Immuno Research	Cat #115-035- 003
α-rabbit IgG (H+L)-HRP	Jackson Immuno Research	Cat#111-035-003
α-rat IgG (H+L)-HRP	Jackson Immuno Research	Cat#112-035-003
Phalloidin Alexa 633	Thermo Fisher Scientific	Cat#A22284
Alexa 488 α-rabbit secondary antibody	Thermo Fisher Scientific	Cat#A-11034
DAPI	Sigma Aldrich	Cat#10236276001
Alexa 488 α-rabbit secondary antibody	Thermo Fisher Scientific	Cat#A21206
α-IgG2a (*in vivo*)	2B scientific	Cat#BE0085
α-DYKDDDDK tag	Thermo Fisher Scientific	Cat#8146
α-CTLA-4 (*in vivo*)	2B scientific	Cat#BE0164
α-PD-1 (*in vivo*)	2B scientific	Cat#BE0146

α-mouse CD107a-BUV395	BD	Cat#565533; Clone#1D4B
α-mouse CD107a- PE	Biolegend	Cat#121611; Clone#1D4B
α-mouse CD44-BUV395	BD	Cat#740215; Clone#IM7
α-mouse CD25-BV650	Biolegend	Cat#102037; Clone#PC61
α-mouse CD4-BV496	BD	Cat#741050; Clone#RM4-4
α-mouse MHCII-PE-Dazzle-594	Biolegend	Cat#107647; Clone#M5/114.15.2
α-mouse CD3-BUV563	BD	Cat#741319; Clone#17A2
α-mouse TCRδ-BUV615	BD	Cat#751183; Clone#GL3
α-mouse TCRδ- PerCpCy5.5	Biolegend	Cat#118117; Clone#GL3
α-mouse CD11c-BUV615	BD	Cat#751222; Clone#N418
α-mouse CD11c-PECy7	Biolegend	Cat#117317; Clone#N418
α-mouse Singlec-F-AF488	Biolegend	Cat#55523; Clone#S17007L
α-mouse Singlec-F-BV605	BD	Cat#121612; Clone#E50-2440
α-mouse CD69-PECy7	Biolegend	Cat#104511; Clone#H1.2F3
α-mouse CD69-BV785	Biolegend	Cat#740388; Clone# H1.2F3
α-mouse CD19- BUV661	BD	Cat#612971; Clone#1D3
α-mouse NK1.10BUV737	BD	Cat#741715; Clone#PK136
α-mouse NK1.1-PECy5	Biolegend	Cat#108715; Clone#PK136
α-mouse CD45-BUV805	BD	Cat#748370; Clone#30F11
α -mouse F4/80-BV650	Biolegend	Cat#123149; Clone#BM8

α-mouse FoxP3-eFlour450	Thermo Fisher Scientific	Cat#17-5773-82; Clone#FJK-16s
α-mouse Ly6G-BV510	Biolegend	Cat#127633; Clone#1A8
α-mouse CD62L-PECy5	Biolegend	Cat#104410; Clone#MEL-14
α-mouse CD8α-BV570	Biolegend	Cat#100739; Clone#53-6.7
α-mouse Ly6C-AF700	Biolegend	Cat#128023; Clone#HK1.4
α-mouse CD11b-BV750	Biolegend	Cat#101267; Clone#M1/70
α-mouse TNFα-APC	Biolegend	Cat#506307; Clone#MP6-XT22
α-mouse Grzmb-AF647	Biolegend	Cat#515405; Clone#GB11
α-mouse IFNγ-AF488	Biolegend	Cat#505815; Clone#HM61.2
α-mouse TCRβ-PerCP-Cy5	Biolegend	Cat#109228; Clone#H57-597
α-mouse CD8α-BUV395	BD Biosciences	Cat#563786; Clone#53-6.7
α-mouse CD4-BV650	Biolegend	Cat#100555; Clone#RM4-5
α-mouse CD44-BV785	Biolegend	Cat#103059; Clone#IM7
α-mouse CD25-EF450	Thermo Fisher Scientific	Cat#48-0251-82; Clone#PC61-5
LIVE/DEAD™ Fixable Near-IR	Thermo Fisher Scientific	Cat#L34976
α-FLAG tag	Cell Singalling Technology	Cat#8146
α-mouse HRP	Abcam	Cat #ab131368
Mouse Fc Block (CD16/CD32)	BD Biosciences	Cat #553141
Bacterial and virus strains		
BL21(DE3) *E. Coli*	New England Bioscience	Cat #C2527
One Shot TOP10 *E. Coli*	Thermo Fisher Scientific	Cat #C404010
Biological samples		

Chemicals, peptides, and recombinant proteins		
Propidium Iodide	Sigma-Aldrich	Cat#P4864
Hoechst-33342, Trihydrochloride, Trihydrate	Thermo Fisher Scientific	Cat#H3570
Glutathione Sepharose 4B beads	GE Healthcare	Cat#17075601
Recombinant mouse M-CSF	Peprotech	Cat#300-25
Gentle Collagenase/Hyaluronidase	Stemcell Technology	Cat#07919
RIPK1 inhibitor GlaxoSmithKline GSK'963	Stratech Scientific	Cat#HY-103028A; CAS#:2049868-46-2
RIPK1 inhibitor (PK68)	Insight Bio	Cat#HY-128348; CAS#:2173556-69-7
RIPK3 inhibitor GlaxoSmithKline GSK'872	Stratech Scientific	Cat#S8465; CAS: 1346546-69-7
Necrostatin-1s	MedChemExpress	Cat#HY-103028A; CAS#: 4311-88-0
RIPK2 PROTAC degrader 2	Cambridge Bioscience	Cat#HY-111866-10 mg; CAS#1801547-16-9
SM-164	Caltag Medsystems	Cat#TAR-T12932L; CAS#957135-43-2
ASTX660	Insight Bio	Cat#HY-109565; CAS#1799328-86-1
Recombinant human TNFa	Enzo	Cat#ALX-522-008-C050
Recombinant mouse TNFa	Enzo	Cat# ALX-522-009-C050
Emricasan, pan-caspase inhibitor	Medkoo	Cat#510230; CAS#254750-02-2
Z-VAD-FMK, pan-caspase inhibitor	Apex Bio	Cat#A1902; CAS #187389-52-2
Bortezomib, proteasome inhibitor	Stratech	Cat#S1013; CAS#179324-69-7
VH298, VHL inhibitor	Abcam	Cat#ab230370
Human recombinant INFβ	Peprotech	Cat#300-02BC
Murine recombinant INFβ	Biomol	Cat#RP0487M
Murine recombinant IFNγ	Peprotech	Cat#315-05
Poly(I:C) HMW	Invivogen	Cat#tlr-pic; CAS#31852-29-6
Riboxxol	Riboxx	Cat#A-00102; CAS#63231-63-0
LPS EK Ultrapure	Invivogen	Cat#tlrl-peklps
Enbrel (Etanercept)	Cambridge Bio	Cat#HY-108847-10
5Z-7-Oxozeaenol, TAK1 inhibitor	Bio-techne	Cat#3604
BX795, TBK1/IKKε inhibitor	Invivogen	Cat#tlrl-bx7-2; CAS#1472611-45-2
p38 inhibitor (Ralimetinib LY2228820 dimesylate)	Selleckchem	Cat#862507-23-1; CAS#862507-23-1
PF-3644022 (MK2 inhibitor)	Bio-Techne	Cat#HY-107427; CAS #1276121-88-0
TPCA-1 (IKK2 inhibitor)	Sigma-Aldrich	Cat#T1452; CAS#507475-17-4

NIK SMI1 (NIK inhibitor)	Stratech	Cat#S8941-SEL; CAS#1660114-31-7
Cycloheximide	Tocris	Cat#0970-100; CAS#66-81-9
HOIPIN-8 (HOIP inhibitor)	Axon MedChem	Cat#2972; CAS#2519537-69-8
Tpl2 kinase inhibitor	Insight biotechnology	Cat#HY-12358; CAS#871307-18-5
XIAP degrader	Insight biotechnology	Cat#HY-115865
DL-Dithiothreitol (DTT)	Sigma-Aldrich	Cat#10708984001; CAS#3483-12-3
PR-619 (DUB inhibitor)	2BScientific	Cat#SI-9619-0005
Recombinant human USP2 Catalytic domain protein	Bio-Techne, R&D	Cat#E504050
Anti-FLAG M2 affinity agarose beads	Sigma-Aldrich	Cat#A2220
Strep-Tactin Sepharose resin beads	IBA lifesciences	Cat#2-1201-025
Lenti-X concentrator	Clontech Takara	Cat#621231
Polybrene	Merk	Cat#TR-1003-G
Lipofectamine RNAiMAX Transfection Reagent	Thermo Fisher Scientific	Cat#13778150
Blasticidin	Invivogen	Cat#ant-bl-05
Collagenase type VI	Sigma Aldrich	Cat#7919
Tryton X-100	Thermo Fisher Scientific	Cat#28314
PR-619 DUB inhibitor	2B Scientific	Cat# SI-9619-0005
PhosSTOP easypack	Sigma Aldrich	Cat#4906837001
Complete protease inhibitor cocktail	Roche	Cat# 11836153001
GSH beads	Sigma Aldrich	Cat#GE17-0756-01
Protein G beads	Sigma Aldrich	Cat#P3296
Clean-Blot IP Detection Reagent (HRP)	Thermo Fisher Scientific	Cat#21230
Dispase	Sigma Aldrich	Cat#D4693-1G
DNase type I	Sigma Aldrich	Cat#DN25
Corning Matrigel GFR	SLS	N/A
Ionomycin from Streptomyces Conglobatus	Sigma Aldrich	Cat#I9657
MRT3767, TBK1i	Sigma Aldrich	Cat#SML0702
HALT Protease and Phosphatase Inhibitor Cocktail	Thermo Fisher Scientific	Cat#78447
Dako REAL peroxidase block	Agilent	Cat#S202386-2
Dako rabbit EnVision polymer-HRP	Agilent	Cat#K400311-2
Dako DAB+	Agilent	Cat#K346811-2
Dako FLEX Haematoxylin	Agilent	Cat#K800821-2
Rabbit ImmPRESS polymer-HRP	Vector Laboratories	Cat#MP-7401-50

Dako Target Retrival Solution	Agilent	Cat#K800421-2
Target retrieval solution (TRS)	Agilent	Cat#K800521-2
Critical commercial assays		
Effectene Transfection Kit	Qiagen	Cat#301427
Nano-Glo HiBiT Lytic Detection KitP	Promega	Cat#N3030
NaveniFlex MR	Bethyl Laboratories	Cat#NF.MR.100
CellTiter-GLO	Promega	Cat#G9681
RNeasy RNA extraction kit	Qiagen	Cat#74106
QuantiTec Reverse Transcription kit	Qiagen	Cat#205314
Pierce™ BCA protein assay kit	Thermo Fisher Scientific	Cat#23227
Deposited data		
Bulk RNA-seq (Sham Vs RT-treated EO771 cells)	Sequence read archive	ID: PRJNA1094427
Mass spectrometry: Human and mouse whole proteome analysis	PRIDE	ID: PXD043560
TCGA Pan-cancer analyses	cBioPortal	N/A
SCAN-B TNBC patient data	GEO Database	ID: GSE96058
GSEA analyses (hallmark gene set collection)	The Molecular Signatures Database (MSigDB)	N/A
Raw western blots and images data from this paper	Mendeley	DOI: 10.17632/822syk52yw.1
Experimental models: Cell lines		
HEK293T	ATCC	Cat#CRL-3216
HT1080	ATCC	Cat#CCL-121
U937	ATCC	Cat#CRL-3253
HT29	ATCC	Cat#HTB-38
MDA-MB-231	ATCC	Cat#CRM-HTB-26
MDA-MB-361	ATCC	Cat#HTB-27
MDA-MB-468	ATCC	Cat#HTB-132
HaCaT	ATCC	Cat#PCS-200-011
LLC	ATCC	Cat#CL-101
L929	ATCC	Cat#CRL-2148
THP-1	ATCC	Cat#TIB-202
EMT6	ATCC	Cat#CRL-2755
Lim1215	Laboratory of Prof. Chris Marshall	N/A
A431	ATCC	Cat#CRL-1555

F3II	Laboratory of Prof. Daniel Alonso	N/A
D2A1	Laboratory of Prof. Clare Isacke	N/A
Kym-1	Laboratory of Prof. John Silke	N/A
Immortalized MDFs	Charles River (Cells generated in house)	N/A
MCA-205	Sigma Aldrich	Cat#SCC-173
EO771	CH3 Biosystems	Cat#94A001
MC38	Kerafast	Cat#ENH204-FP
Wildtype BMDMs and Lung fibroblasts (C57BL/6)	Charles River (Cells generated in house)	N/A
Spata2$^{-/-}$ BMDMs (C57BL/6)	Laboratory of Prof. Mads Gyrd-Hansen's	N/A
Trif$^{-/-}$ BMDMs (C57BL/6) (*Ticam1*$^{-/-}$)	Laboratory of Prof. Manolis Pasparakis	N/A
Zbp1$^{-/-}$ BMDMs (C57BL/6)	Laboratory of Prof. Manolis Pasparakis	N/A
Trif$^{-/-}$*Zbp1*$^{-/-}$ BMDMs and LFs (C57BL/6) (*Ticam1*$^{-/-}$*Zbp1*$^{-/-}$)	Laboratory of Prof. Manolis Pasparakis	N/A
L929 Tradd$^{-/-}$	This Manuscript	N/A
L929 *Tradd*$^{-/-}$ reconstituted with TRADD WT	This Manuscript	N/A
L929 *Tradd*$^{-/-}$ reconstituted with TRADD DD-only	This Manuscript	N/A
L929 *Tradd*$^{-/-}$ reconstituted with TRADD Y16A/F18A	This Manuscript	N/A
L929*Tradd*$^{-/-}$ reconstituted with TRADD C239S	This Manuscript	N/A
L929 *Tradd*$^{-/-}$ reconstituted with TRADD Call>S	This Manuscript	N/A
L929 GFP-RIPK1ΔKDΔRHIM	This Manuscript	N/A
L929 GFP-RIPK1 DD-only	This Manuscript	N/A
E0771 GFP-RIPK1ΔKDΔRHIM	This Manuscript	N/A
E0771 GFP-RIPK1 DD-only	This Manuscript	N/A
293T-*Ripk1*$^{-/-}$	This Manuscript	N/A
E0771-*Ripk1*$^{-/-}$	This Manuscript	N/A
E0771-*Tnfr1*$^{-/-}$	This Manuscript	N/A
E0771-*Mlkl*$^{-/-}$	This Manuscript	N/A
Experimental models: Organisms/strains		
C57BL/6-*Mlkl*$^{-/-}$	Laboratory of Prof. Henning Walczak	N/A
C57BL/6-*Casp8*$^{-/-}$*Ripk3*$^{-/-}$	Laboratory of Prof. Henning Walczak	N/A
C57BL/6-*Casp8*^{tm1Hed}*/J*	The Jackson Laboratory	RRID:IMSR_JAX:027002
C57BL/6.Cg-*Ndor1*$^{Tg(UBC-cre/ERT2)1Ejb}$/1J	The Jackson Laboratory	RRID:IMSR_JAX:007001
C57BL/6-*Tnfrsf1a*^{tm1Imx}/J	The Jackson Laboratory	RRID:IMSR_JAX:003242

C57BL/6-*Ifnar1*$^{tm1.2Ees}$/J	The Jackson Laboratory	RRID:IMSR_JAX:028288
C57BL/6-*Ripk1*$^{fl/fl}$	Laboratory of Prof. Manolis Pasparakis	N/A
Oligonucleotides		
SMART vector inducible non-targeting (*Nt*) shRNA	Dharmacon	VSC11502
SMART vector inducible *Ripk1* shRNA	Dharmacon	V3SM11253-237881699
SMART vector inducible *Trif* shRNA (*Ticam1*)	Dharmacon	V3SM11253-235355483
SMART vector inducible *Zbp1* shRNA	Dharmacon	V3SM11253-235538171
See Table S2 for PCR primers, Taqman probes, siRNAs & CRISPR gRNAs		
Recombinant DNA		
pTRIBZ	This Manuscript	N/A
pTIBZ-Cre	This Manuscript	N/A
pTIBZ-N2xFLAG-m*Tradd*-WT	This Manuscript	N/A
pTIBZ-N2xFLAG-m*Tradd*-DD	This Manuscript	N/A
pTIBZ-N2xFLAG-m*Tradd*-Y16A/F18A	This Manuscript	N/A
pTIBZ-N2xFLAG-m*Tradd*-Call>S	This Manuscript	N/A
pTIBZ-N2xFLAG-m*Tradd*-C239S	This Manuscript	N/A
pMA-RQ-N2xFLAG-m*Tradd*-WT	This Manuscript	Synthetic, Invitrogen
pMA-RQ-N2xFLAG-m*Tradd*-DD	This Manuscript	Synthetic, Invitrogen
pMA-RQ-N2xFLAG-m*Tradd*-Y16A/F18A	This Manuscript	Synthetic, Invitrogen
pMA-RQ-N2xFLAG-m*Tradd*-Call>S	This Manuscript	Synthetic, Invitrogen
pMA-RQ-N2xFLAG-m*Tradd*-C239S	This Manuscript	Synthetic, Invitrogen
pTIBZ-m*Ripk3*-WT	This Manuscript	N/A
pTIBZ-m*Ripk3*-RHIMm	This Manuscript	N/A
pTIBZ-EGFP-m*Ripk1* ΔKDΔRHIM	This Manuscript	N/A
pTIBZ-EGFP-m*Ripk1* DD-only	This Manuscript	N/A
pMA-RQ-m*Ripk1* ΔKDΔRHIM	This Manuscript	Synthetic, Invitrogen
pMA-RQ-m*Ripk1* DD-only	This Manuscript	Synthetic, Invitrogen
pTRIPZ	Open Biosystems	Cat#RHS4696
pTIPZ-h*Ripk1* ΔRHIMΔDD-HiBiT	This Manuscript	N/A
pTYB1	New England BioLabs Inc.	Cat#N6701
pTYB1-FLAG-m*Tradd* WT	This Manuscript	N/A
pT7CFE1-CHis	ThermoFisher	88860
T7CFE-m*Ripk3*	This Manuscript	N/A
pcDNA3.1	Invitrogen	Cat#V79520
pcDNA3-GFP-2xHA/2xStrep	This Manuscript	N/A
pcDNA3.5-N2xHA-m*Ripk1*	This Manuscript	N/A
pcDNA3-N3xHA-m*Zbp1*	This Manuscript	N/A
pcDNA3-N3xHA-m*Ripk3*	This Manuscript	N/A
pcDNA3-m*Trif*-C3xHA (*Ticam1*)	This Manuscript	N/A
pcDNA3-N2xFLAG-m*Tradd*	This Manuscript	N/A
pLC-EGFP	Gift from B. Bornhauser	Addgene Cat# 75159
pLC-Cherry	Gift from B. Bornhauser	Addgene Cat# 75161
pSpCas9(BB)-2A-GFP	Addgene	48138
pLC-EGFP-m*Tradd* gRNA (CGCAACTGGACGATGAGCTG)	This Manuscript	N/A

pLC-EGFP-m*Tnfr1* gRNA (CGGACAGTCACTCACCAAGT)	This Manuscript	N/A
pLC-*Mlkl* gRNA-CGM25 (CTGGCAGCAGGAAGATCGAC)	This Manuscript	N/A
pLC-*Ripk1* gRNA-CGM19 (AGGGAACTATTCGCTGGTGA)	This Manuscript	N/A
pMA-h*Ripk1*-gRNA (GCTCGGGCGCCATGTAGTAG)	This Manuscript	Synthetic, Invitrogen
psPAX2	Addgene	Cat# 12260
pMD2.G	Addgene	Cat# 12259
pBABE SV40 (Δ89-93)	Gift from Parmjit Jat (Cotsiki et al, 2004)	https://doi.org/10.1073/pnas.0308006100
Software and algorithms		
Dotmatics	Dotmatics	N/A
Harmony High Content Analysis Software	Perkin Elmer	N/A
ImageLab (v6.1.0)	Bio-Rad	N/A
GraphPad Prism (v10.2.1) (339)	Dotmatics	N/A
Adobe Illustrator (v28.0) (2024)	Adobe	N/A
R studio package (v4.3.0)	Limma	N/A
Fiji (v2.9.0)	ImageJ	N/A
FlowJo (v.10)	BD Biosciences	N/A
FACSDIVA software (v6.1.3)	BD Biosciences	N/A
Other		

Figure

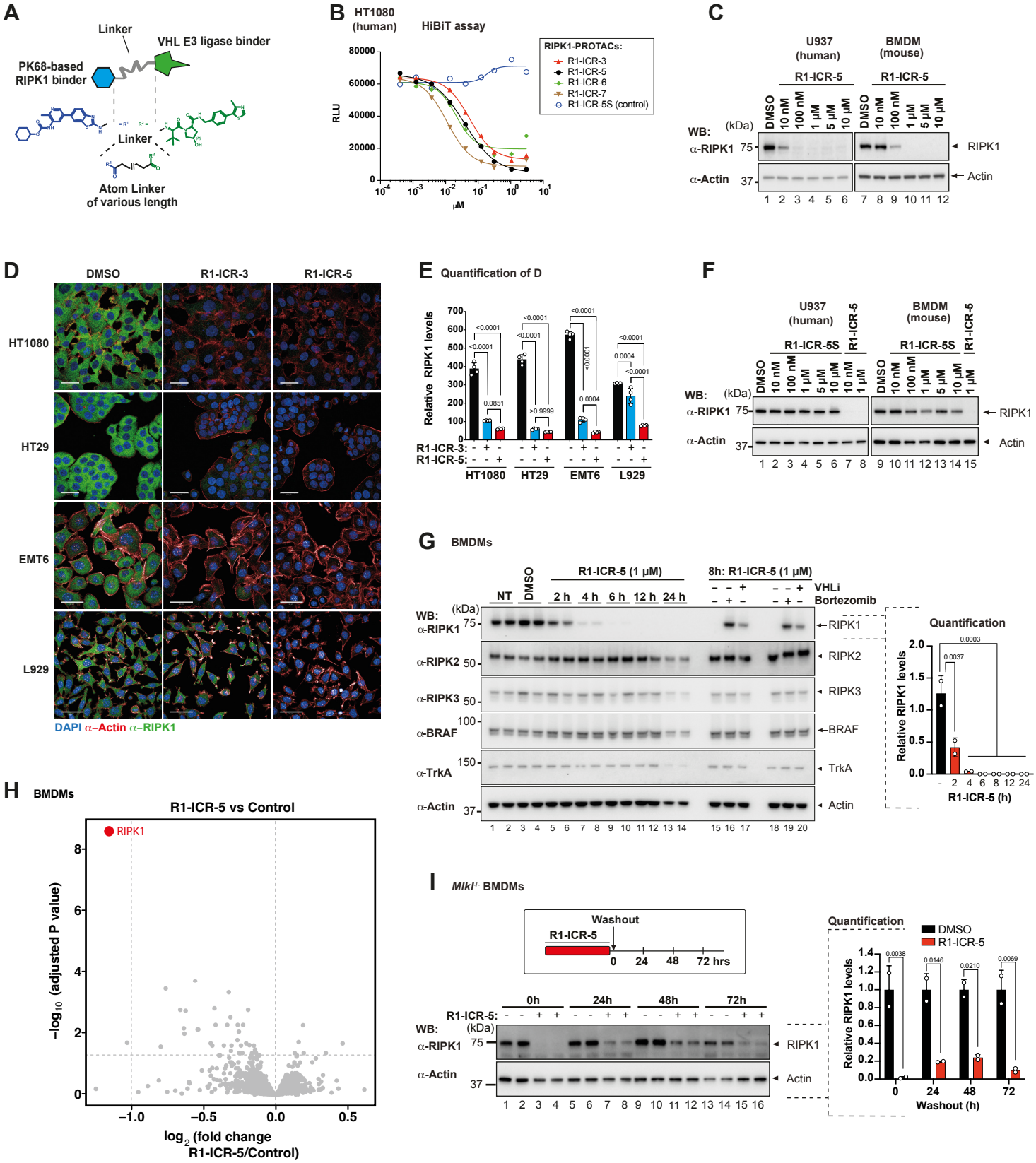

Figure 1

Figure

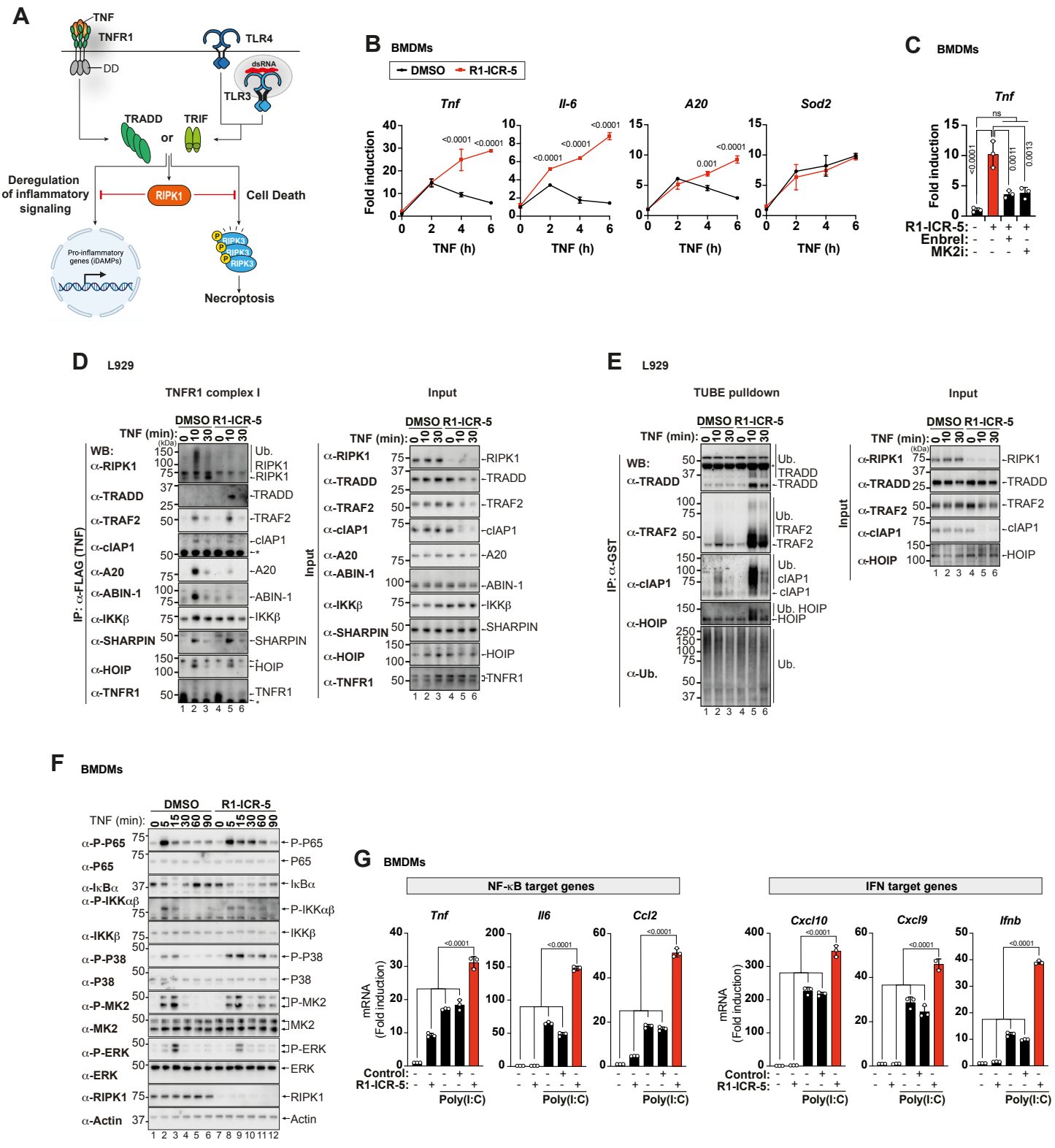

Figure 2

Figure

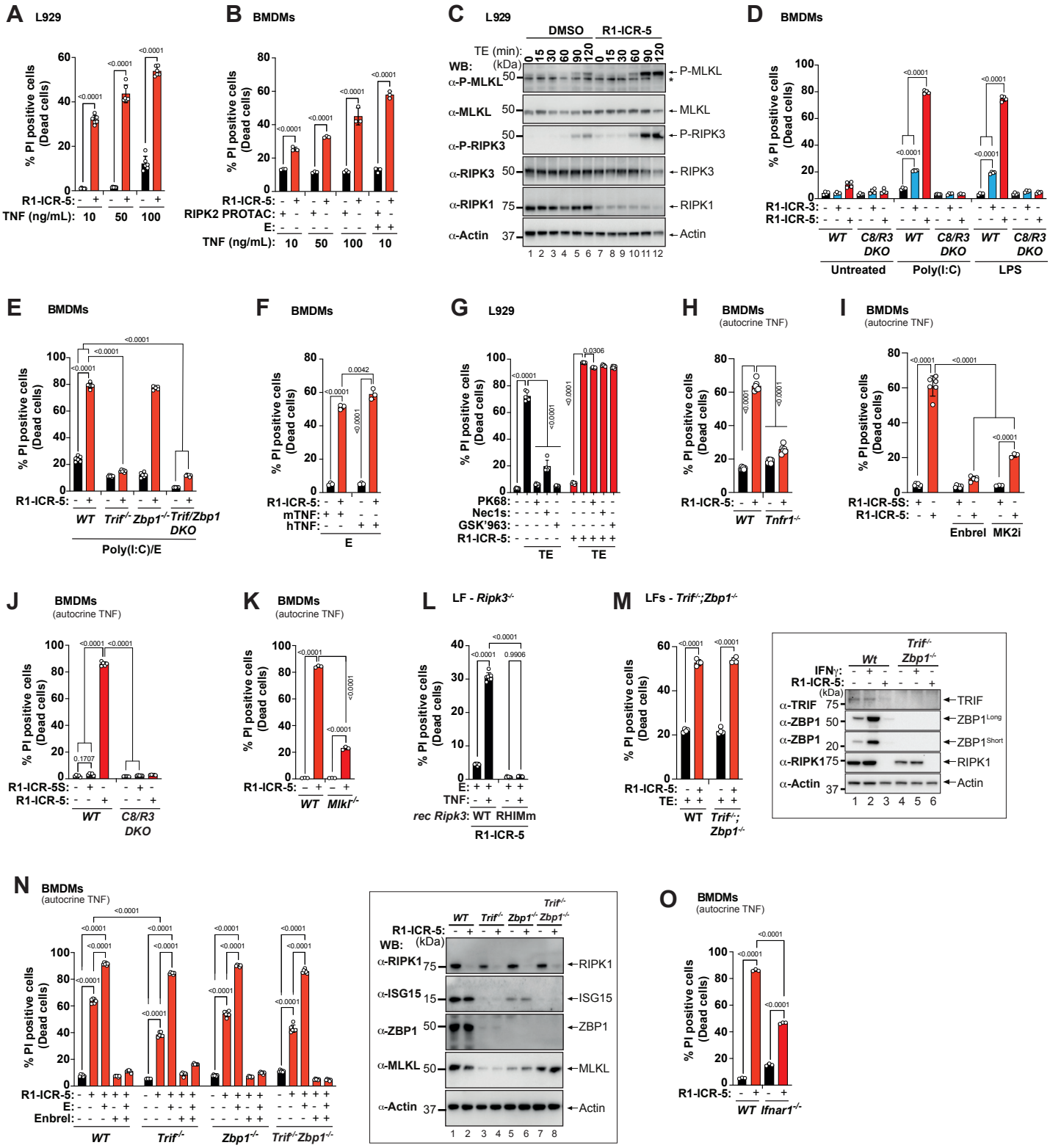

Figure 3

Figure

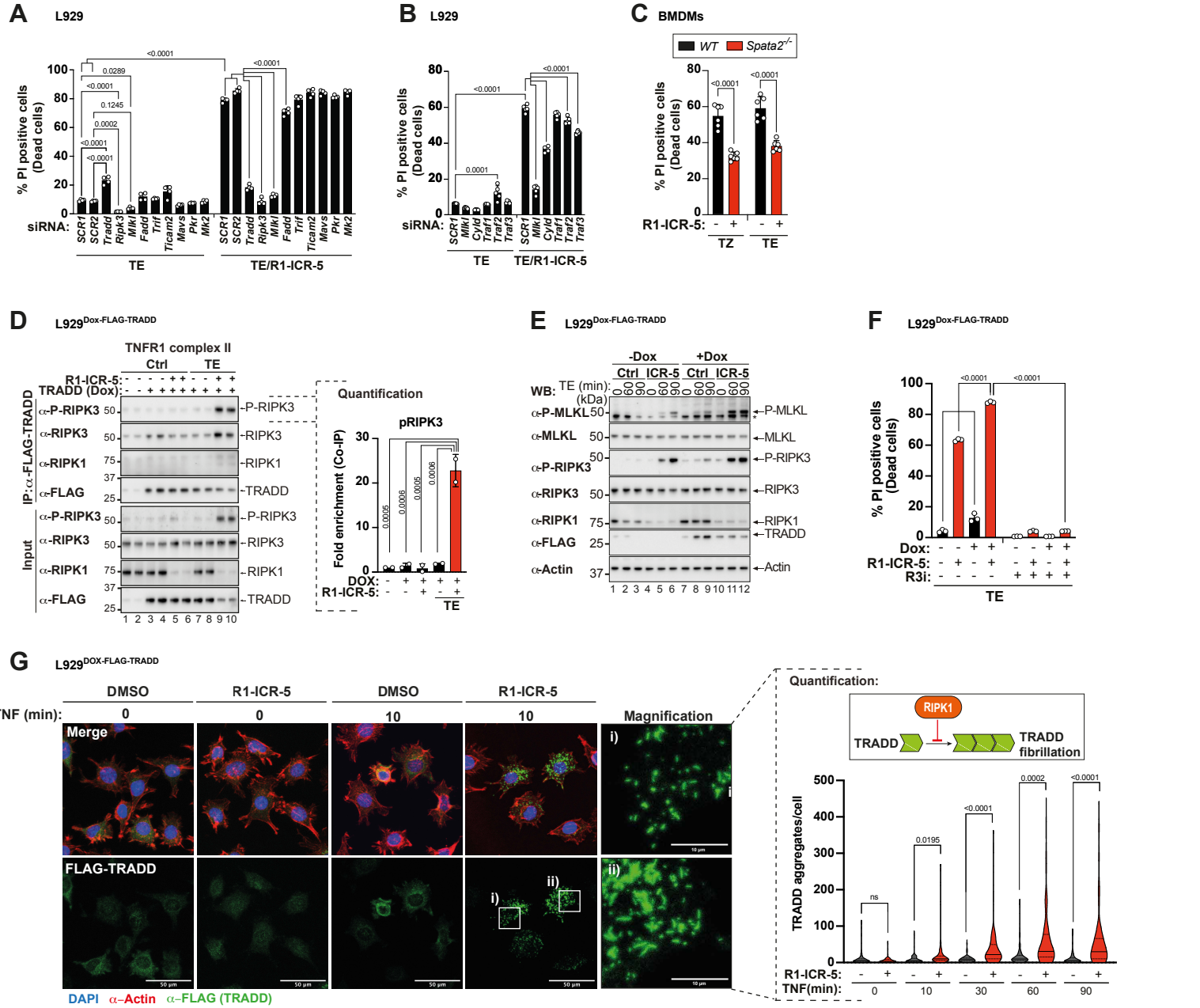

Figure 4

Figure

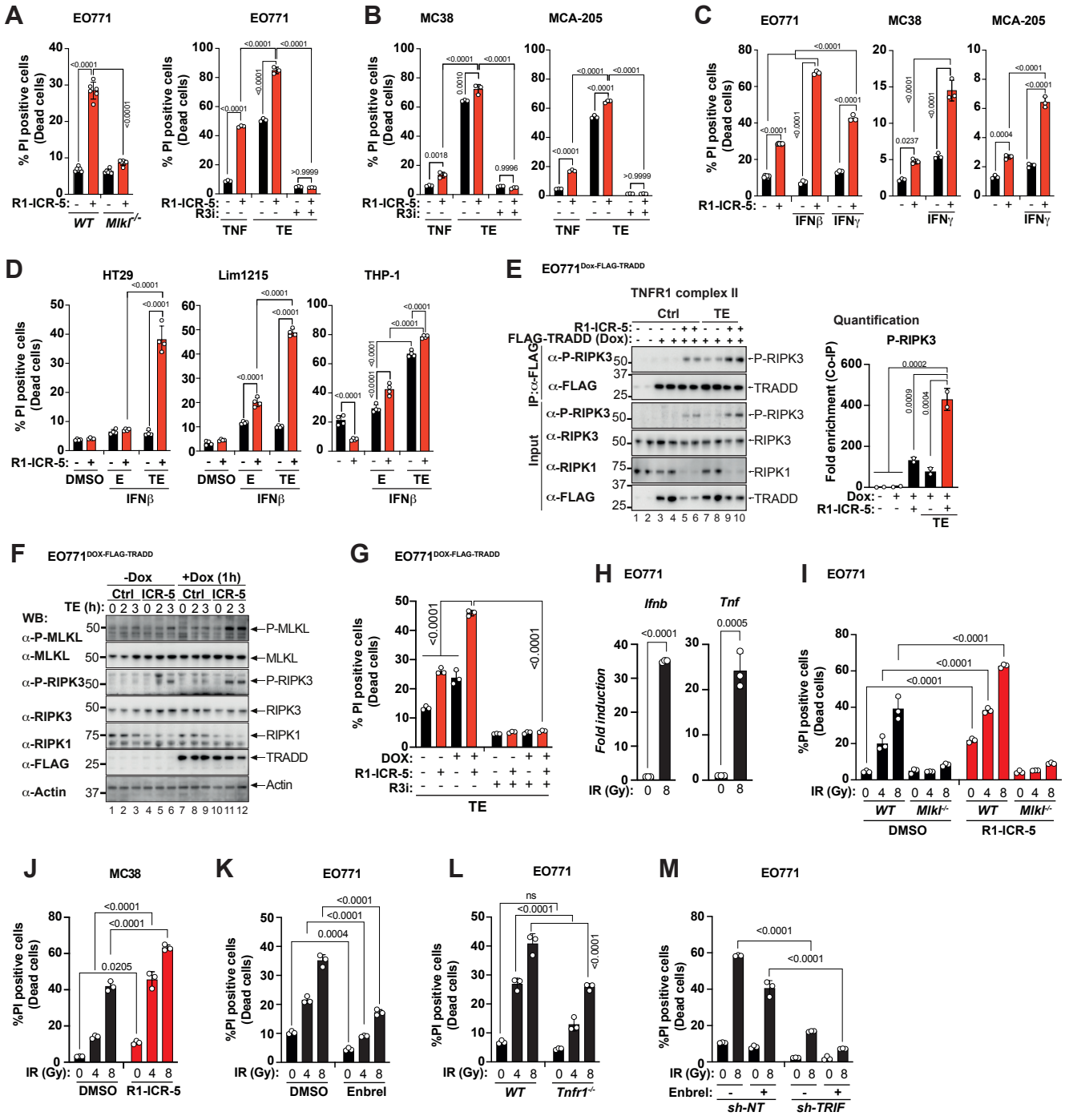

Figure 5

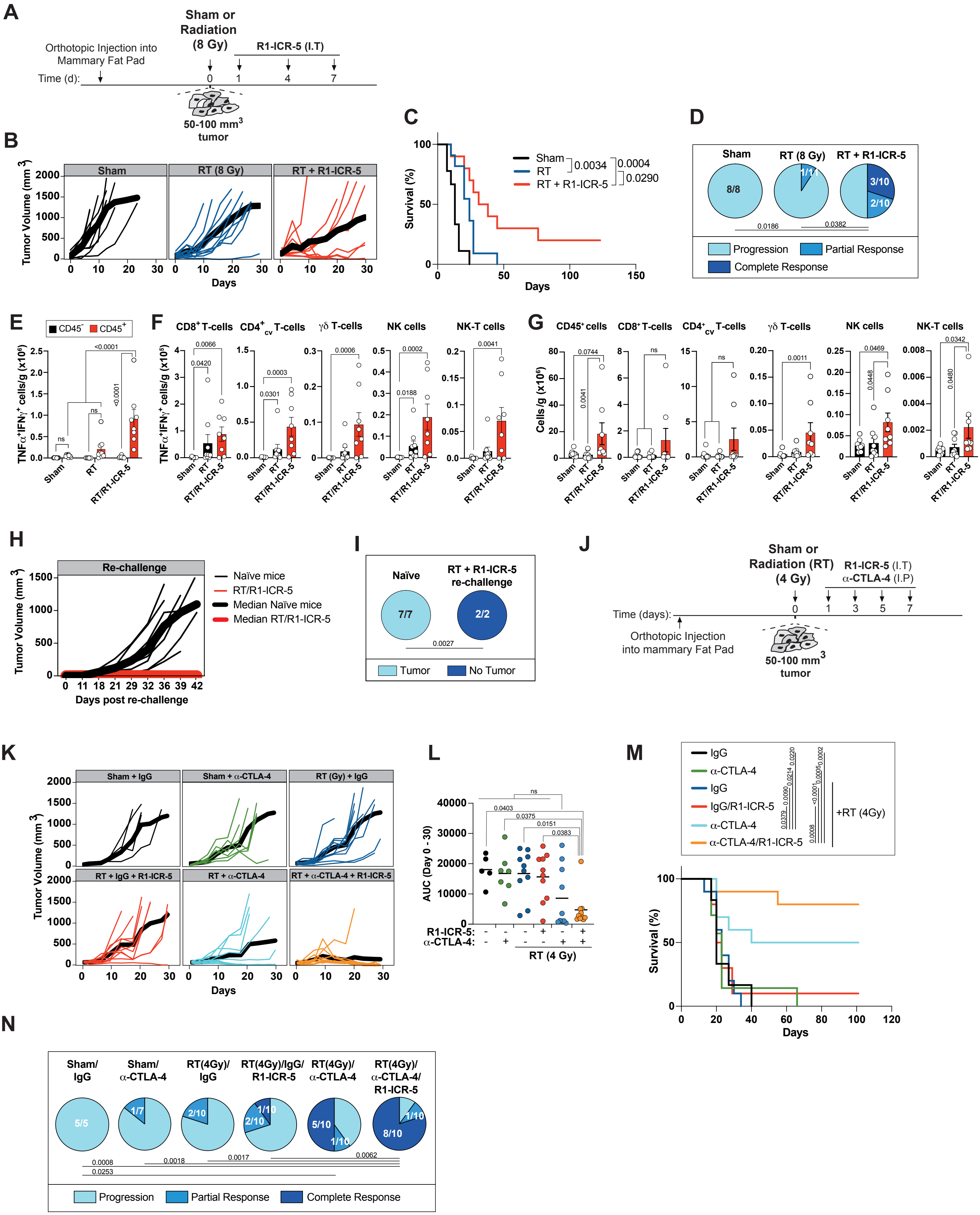
A
Orthopic Injection into Mammary Fat Pad
Sham or Radiation (8 Gy)
R1-ICR-5 (I.T)
Time (d):
0
1
4
7
50-100 mm^3 tumor
B
Sham
RT (8 Gy)
RT + R1-ICR-5
Tumor Volume (mm^3)
Days
C
Survival (%)
Sham
RT
RT + R1-ICR-5
0.0034
0.0004
0.0290
Days
D
Sham
RT (8 Gy)
RT + R1-ICR-5
8/8
1/11
3/10
2/10
0.0186
0.0382
Progression
Partial Response
Complete Response
E
CD45$^-$
CD45$^+$
TNFα$^+$IFNγ$^+$ cells/g (x10^6)
<0.0001
ns
ns
<0.0001
Sham
RT
RT/R1-ICR-5
F
CD8$^+$ T-cells
CD4$^+_{cv}$ T-cells
γδ T-cells
NK cells
NK-T cells
TNFα$^+$IFNγ$^+$ cells/g (x10^5)
0.0066
0.0420
0.0003
0.0301
0.0006
0.0002
0.0188
0.0041
G
CD45$^+$ cells
CD8$^+$ T-cells
CD4$^+_{cv}$ T-cells
γδ T-cells
NK cells
NK-T cells
Cells /g (x10^6)
0.0744
0.0041
ns
ns
0.0011
0.0469
0.0448
0.0342
0.0480
H
Re-challenge
Tumor Volume (mm^3)
Naïve mice
RT/R1-ICR-5
Median Naïve mice
Median RT/R1-ICR-5
Days post re-challenge
I
Naïve
RT + R1-ICR-5 re-challenge
7/7
2/2
0.0027
Tumor
No Tumor
J
Sham or Radiation (RT) (4 Gy)
R1-ICR-5 (I.T)
α-CTLA-4 (I.P)
Time (days):
0
1
3
5
7
Orthopic Injection into mammary Fat Pad
50-100 mm^3 tumor
K
Sham + IgG
Sham + α-CTLA-4
RT (Gy) + IgG
RT + IgG + R1-ICR-5
RT + α-CTLA-4
RT + α-CTLA-4 + R1-ICR-5
Tumor Volume (mm^3)
Days
L
AUC (Day 0 - 30)
ns
0.0403
0.0375
0.0151
0.0383
R1-ICR-5:
α-CTLA-4:
RT (4 Gy)
M
IgG
α-CTLA-4
IgG
IgG/R1-ICR-5
α-CTLA-4
α-CTLA-4/R1-ICR-5
+RT (4Gy)
0.0220
0.0214
0.0090
0.0379
0.0002
0.0005
<0.0001
0.0008
Survival (%)
Days
N
Sham/ IgG
Sham/ α-CTLA-4
RT(4Gy)/ IgG
RT(4Gy)/IgG/ R1-ICR-5
RT(4Gy)/ α-CTLA-4
RT(4Gy)/ α-CTLA-4/ R1-ICR-5
5/5
1/7
2/10
1/10
2/10
5/10
1/10
1/10
8/10
0.0008
0.0253
0.0018
0.0017
0.0062
Progression
Partial Response
Complete Response

Figure 6

Figure

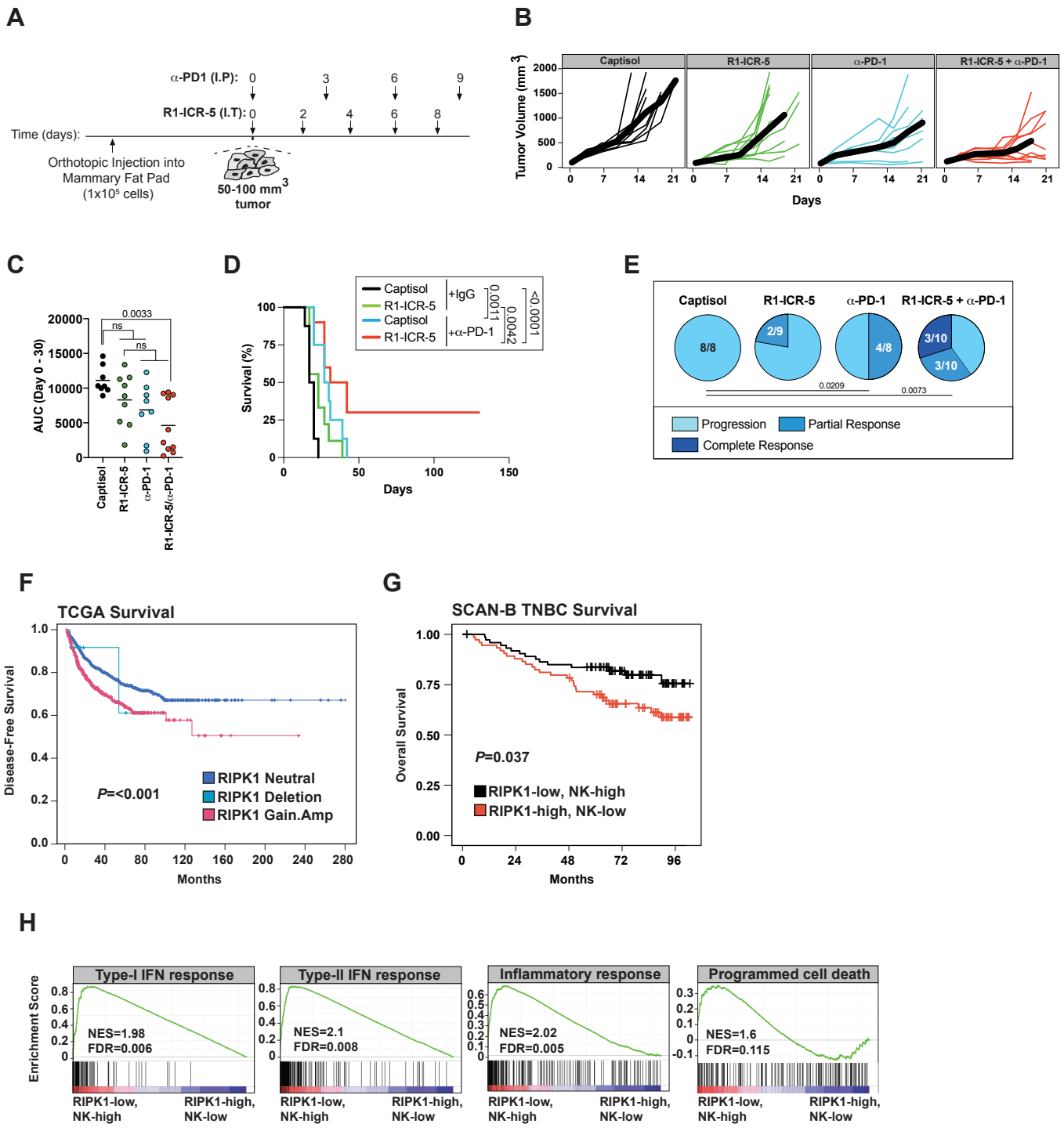

Figure 7

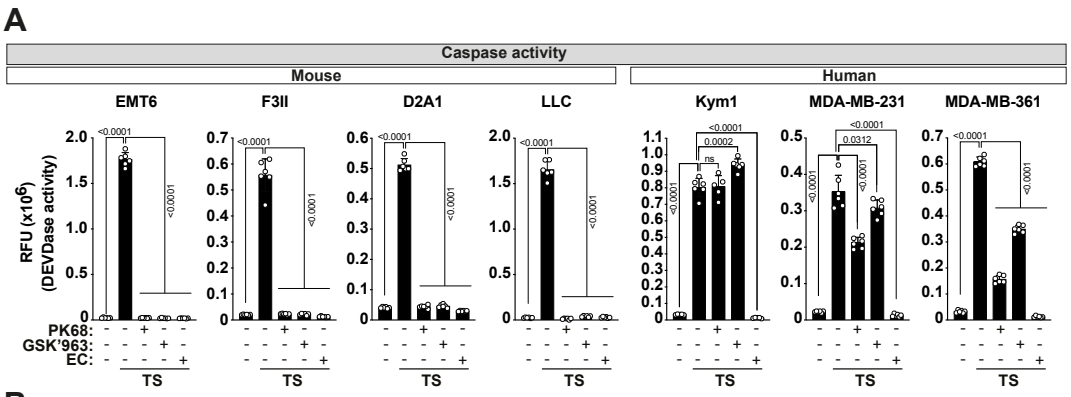

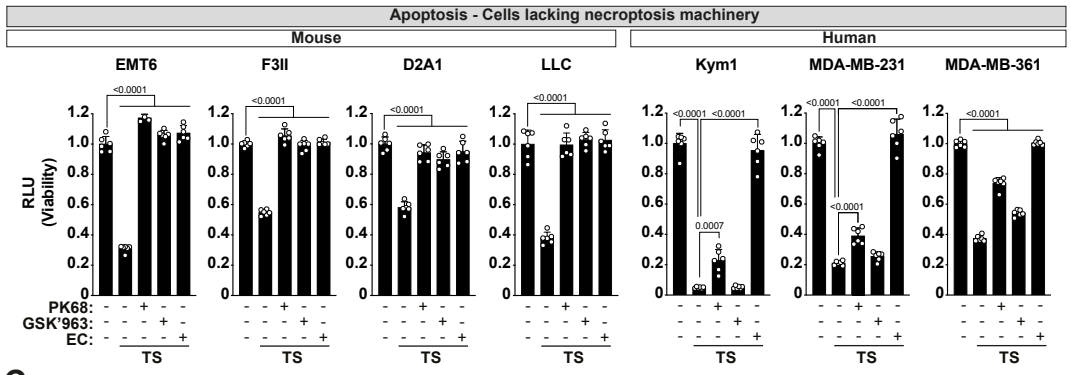

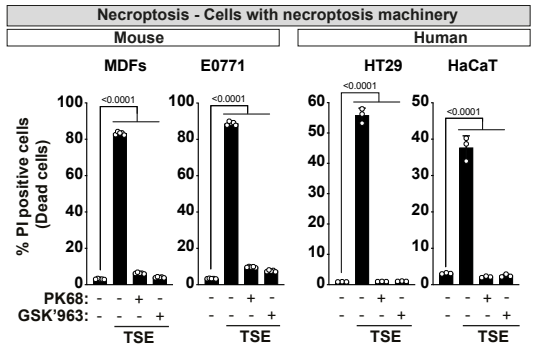

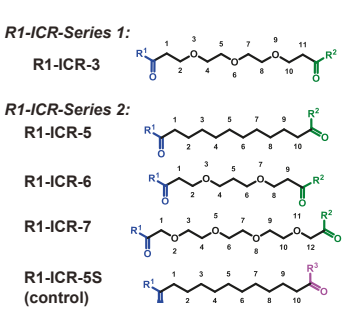

Protac	DC_{50}(mM)	D_{max}
R1-ICR-3	0.11	85
R1-ICR-5	0.05	101
R1-ICR-6	0.04	84
R1-ICR-7	0.02	92
R1-ICR-5S	n/a	-3

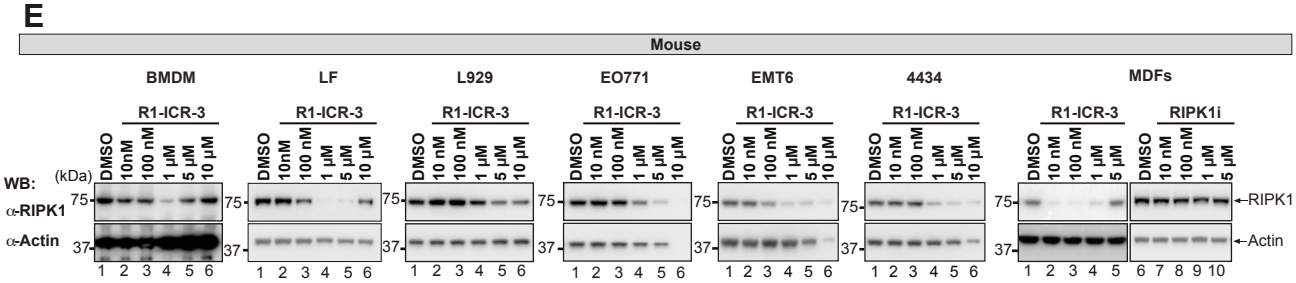

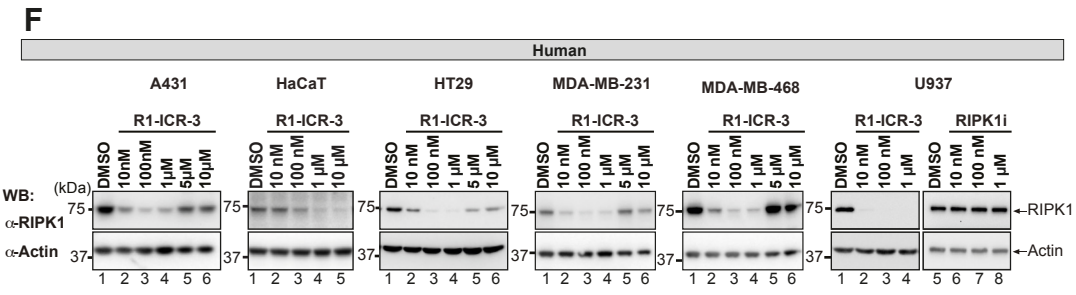

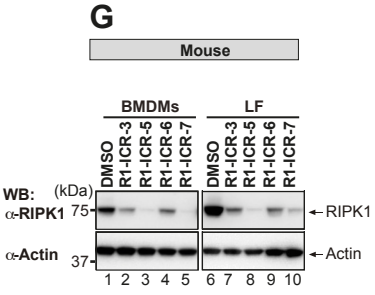

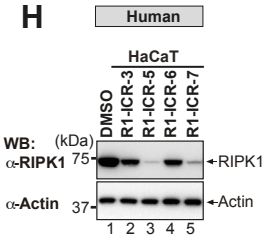

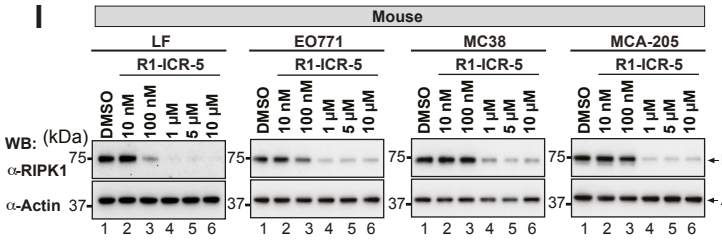

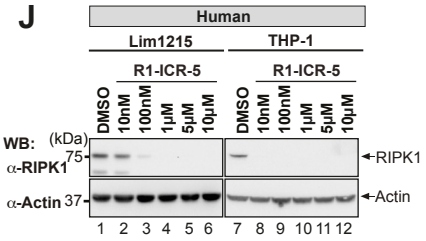

Suppl Figure S1

Suppl Fig S1. Development of selective RIPK1 PROTAC degraders

(A) Caspase activity assay of the indicated cell lines. Cells were treated with TNF and Smac mimetic (SM164) in the presence or absence of the caspase inhibitor Emricasan (E), RIPK1i (PK68 and GSK'963) and caspase activity was assayed with Ac-DEVD-AMC.

(B) Viability assay of the indicated cells lines. Cells were treated as in (a), and viability was measured using CTG viability assay.

(C) Quantification of PI^+ cells treated with TSE in the presence or absence of RIPK1 inhibitors PK68 and GSK'963, respectively.

(D) Schematic diagram depicting the linker of RIPK1-specific VHL-based degraders. Values for half-maximal degradation concentration (DC_{50}, mM) and maximal degradation efficiency (D_{max}) are provided. R1-ICR-5S is a control molecule has inverted stereochemistry at the proline 4-position (R3), to preclude VHL binding.

(E-J) A range of mouse and human cell lines were treated for 24 h (E,F) or 6 h (G-J) with different concentrations of the indicated PROTACs or RIPK1i (PK68). RIPK1 degradation was analysed by western blot.

Data show mean ± SD and are representative of $\geq$2 independent biological repeats. *P* values were calculated using (A-C) one-way ANOVA with Bonferroni's multiple comparison test.

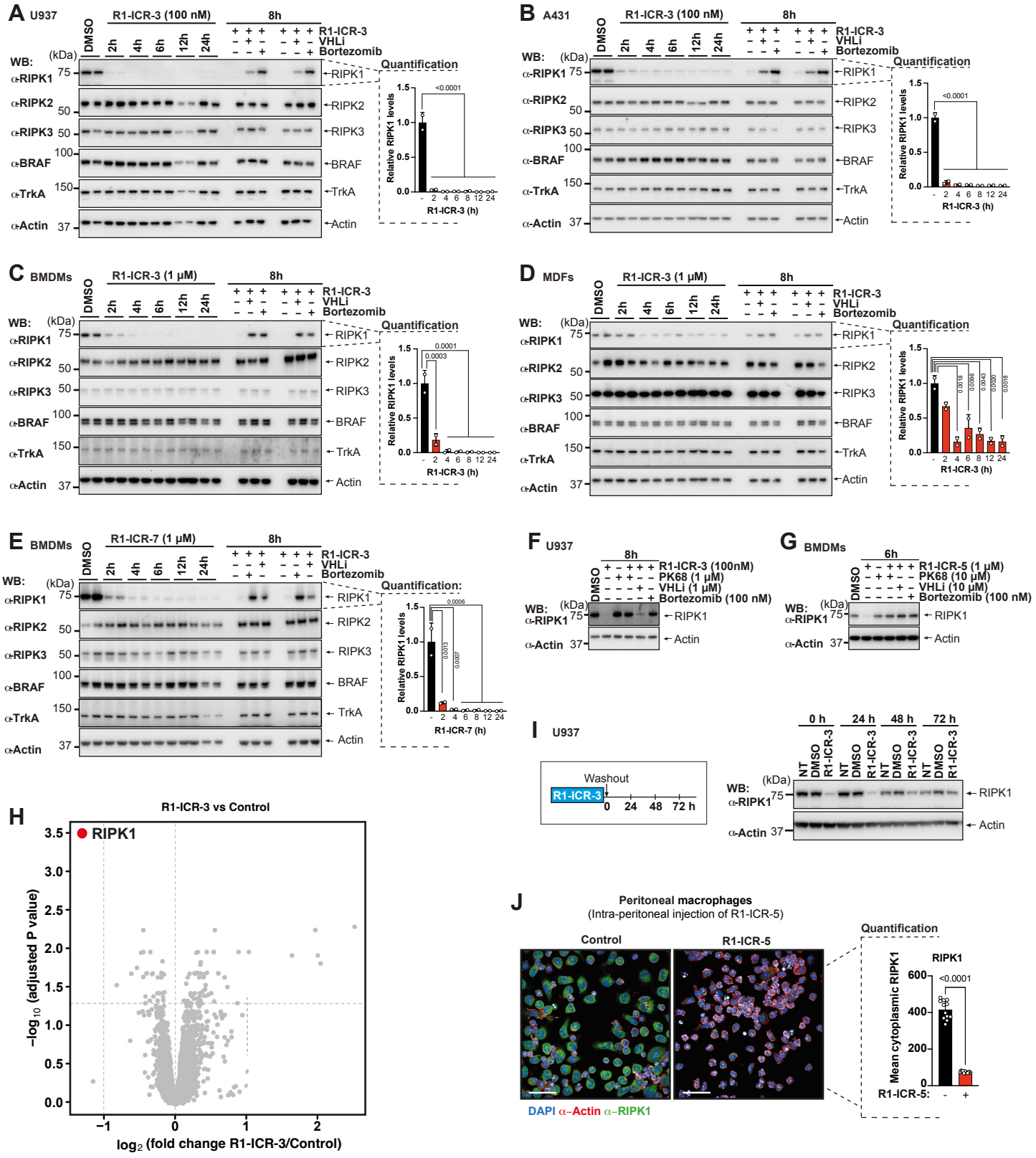

Suppl Figure S2

Suppl Fig S2. RIPK1 PROTACs acutely and specifically degrade human and mouse RIPK1

(A-E) The indicated cells were treated with RIPK1 PROTACs as indicated, in the presence and absence of PK68, VHL inhibitor (VH298) or proteasome inhibitor (Bortezomib). Protein degradation was analysed by western blot and densitometry.

(F,G) U937 or BMDMs were pre-treated for 1 h with indicated concentrations of RIPK1i (PK68), VHLi (VH298) or proteasome inhibitor (Bortezomib/PS341), before PROTAC treatment (F, 8 h R1-ICR-3; G, 6 h R1-ICR-5). Protein degradation was analyzed by western blot.

(H) Volcano plot depicting changes in the whole proteome of U937 cells, left untreated or treated with R1-ICR-3 for 6 h. Log_2 fold change and $-log_{10}$ adjusted P values are shown along the x- and y-axis, respectively. P values were adjusted using the Benjamin-Hochberg procedure.

(I) U937 cells were treated with R1-ICR-3 for 24 h, followed by washout. RIPK1 protein re-synthesis was analyzed by western blot.

(J) R1-ICR-5 depletes RIPK1 in peritoneal macrophages *in vivo*. WT mice were injected intraperitoneally with R1-ICR-5. 6 h post-treatment, peritoneal macrophages were isolated and analyzed by IF. Mice per treatment group: Control (n=3) and R1-ICR-5 **(**n=4). Quantification represents one mouse per condition.

Number of mice (J) per treatment group, n = 3 for control**,** n = 4 for R1-ICR-5. Quantification is one animal per condition.

Data show mean ± SD. Data represent ≥2 independent experiments. *P* values were calculated using (A-E) one-way ANOVA with Bonferroni‘s multiple comparison test, (H) adjusted *p* values (Benjamin-Hochberg procedure) and (J) by unpaired t-test.

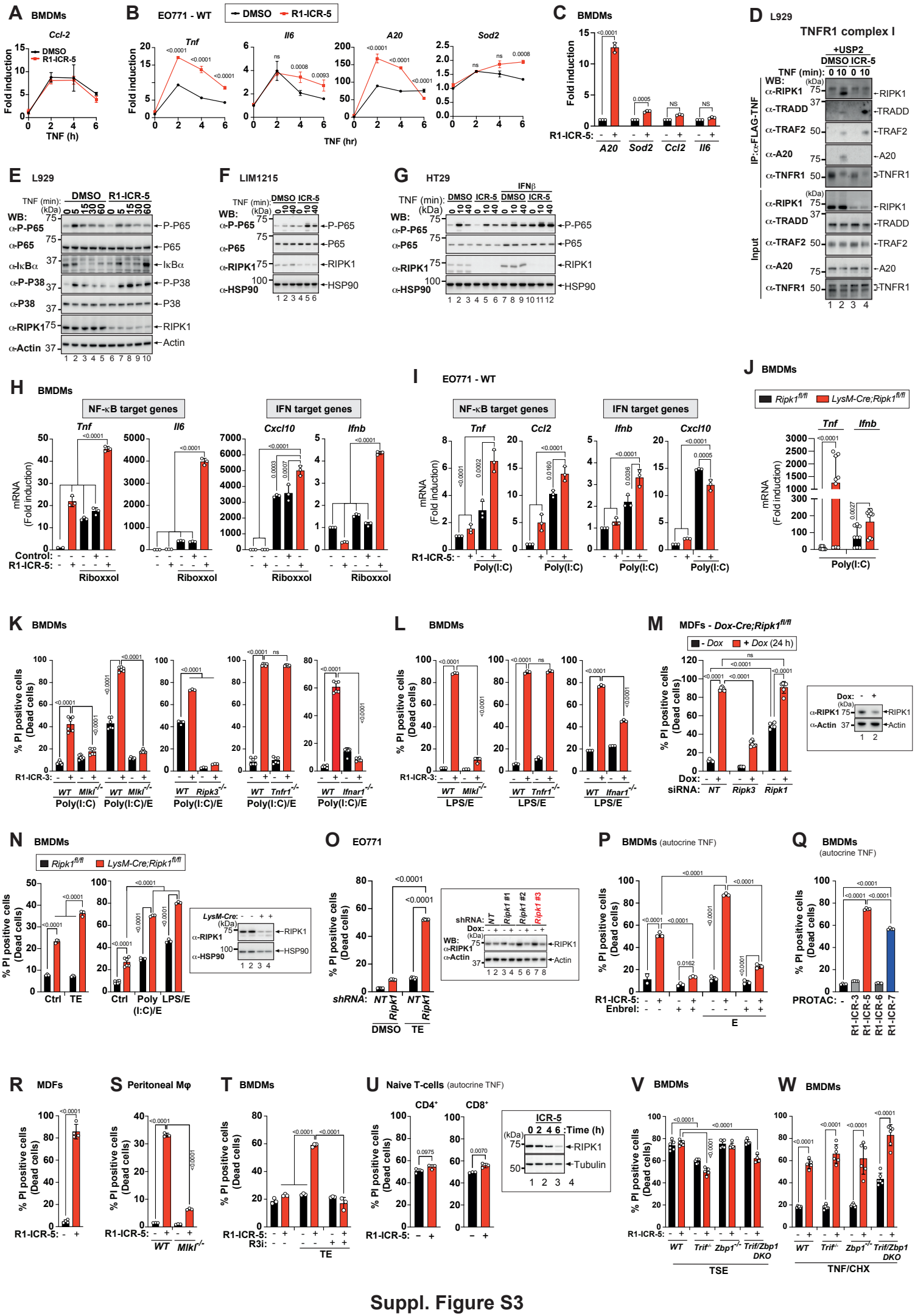

Suppl. Figure S3

Suppl Fig S3. Acute RIPK1 degradation deregulates innate immune signaling and cell death

(A-C) Relative mRNA expression of NF-κB target genes in the indicated cell types, pre-treated with DMSO or R1-ICR-5 4 h, followed by TNF treatment. (C) Cells were treated with DMSO or R1-ICR-5 for 8 h. Graphs show mean ± SD, n = 3 independent biological replicates.

(D) L929 cells were treated with DMSO or R1-ICR-5 (ICR-5) overnight and TNFR1 signaling complex I isolated. Subsequently, ubiquitin adducts were cleaved by USP2 digestion. Western blot analyses were performed using indicated antibodies.

(E) Western blot analysis of L929 cells, pre-treated with DMSO or R1-ICR-5 overnight, followed by TNF stimulation for the indicated time points. Data represent 2 independent experiments.

(F,G) The indicated cells were pre-treated with DMSO or R1-ICR-5 (ICR-5), followed by TNF for indicated time points. (G) HT29 were left untreated or pre-incubated (before DMSO or R1-ICR-5 treatment) with IFNβ overnight.

(H-J) Relative mRNA expression of NF-κB or IFN target genes. The indicated cell types were pre-treated with DMSO and R1-ICR-5 for 4 h, followed by 4 h treatment with the respective TLR3 agonists (H, Riboxxol and I & J, Poly(I:C)). (J) BMDMs from 3 biological replicates were run in triplicates.

(K,L) Quantification of PI+ of the indicated BMDMs. Cells were pre-treated with DMSO or R1-ICR-3 for 5 h, before treatment with the indicated agents.

(M-O) Acute, genetic removal of RIPK1 phenocopies the effect of R1-ICR-5. (M) Dox-*Cre*;*Ripk1*$^{fl/fl}$ MDFs were treated with the indicated siRNA oligos. Subsequently, cells were left untreated or exposed to Dox to induce Cre that drives deletion of RIPK1. *Ripk1*-depletion was validated by western blot analysis (24 h Dox). (N) Quantification of PI$^+$ *Ripk1*$^{fl/fl}$;*LysM-Cre* BMDMs. The indicated cells were treated for 6 h as indicated. RIPK1 depletion was confirmed by western blot analysis. (O) Quantification of PI$^+$ EO771 cells stably expressing Dox-inducible *shRNA* constructs (*shNt* or *shRipk1*#3). Cells were incubated with Dox for 72 h, before treatment with DMSO or TE. *Ripk1* knockdown was assessed by western blot analysis.

(P-S) Quantification of PI$^+$ of the indicated cell types. Cells were treated as indicated, for 24 h.

(T) Quantification of PI$^+$ BMDMs, pre-treated with R1-ICR-5 for 4 h, before cells were incubated with the indicated reagents. TNF, in the presence and absence of RIPK3 inhibitor (7h).

(U) Quantification of PI$^+$ of Naïve CD4$^+$ and CD8$^+$ T-cells. Cells were treated with R1-ICR-5 for 24 h. RIPK1 degradation was analyzed by western blot.

(V,W) Quantification of PI^+ of the indicated cells, pre-treated with DMSO or R1-ICR-5 for 4 h. Subsequently, cells were treated as indicated.

Data show mean ± SD. Data represent ≥2 independent experiments. *P* values were calculated using (H,L,Q-S) one-way ANOVA with Bonferroni‘s multiple comparison test or (A-C,J,K-P,T,V,W) two-way ANOVA with Sidak‘s multiple comparison test and (U) unpaired t-test.

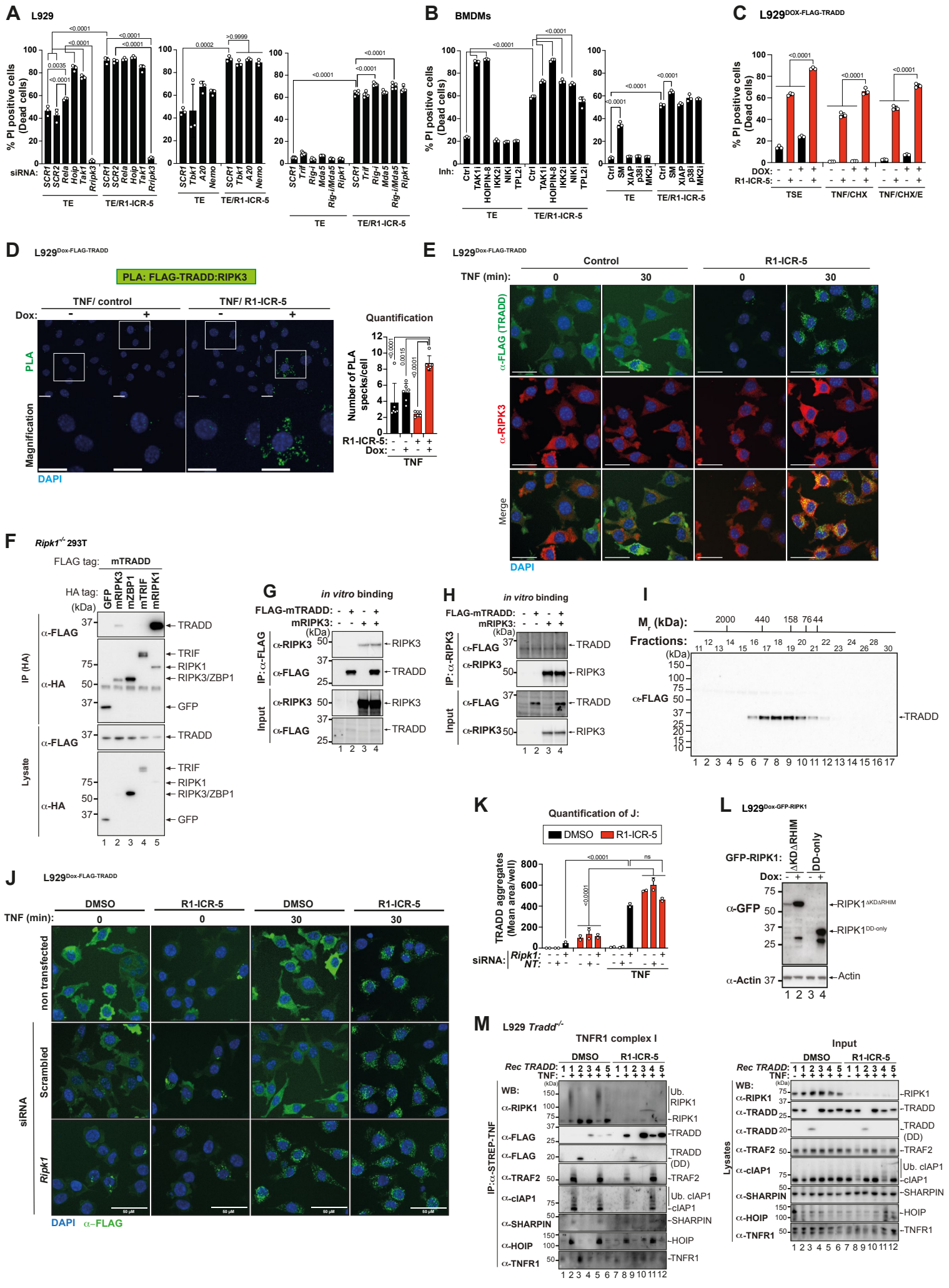

Suppl. Figure S4

Suppl Fig S4. RIPK1 impedes TNF-induced TRADD fibrillation and non-canonical necroptosis

(A) Quantification of PI^+ L929 cells. Cells were treated with the indicated siRNA oligos for 48 h. Subsequently, cells were treated with DMSO or R1-ICR-5 for 24 h, and exposed to TE.

(B) Quantification of PI^+ BMDMs, pre-treated with DMSO or R1-ICR-5 for 4.5 h. Subsequently, cells were treated with the indicated inhibitors 45 min, before treatment TE.

(C) Quantification of PI^+ $L929^{Dox\text{-}Flag\text{-}TRADD}$. Cells were pre-treated with DMSO or R1-ICR-5 for 18 h, followed by 1 h induction of FLAG-TRADD (Dox). Subsequently, cells were treated with the indicated reagents.

(D) *In situ* PLA detection of RIPK3 and FLAG-TRADD in $L929^{Dox\text{-}FLAG\text{-}TRADD}$ cells. Cells were treated with DMSO or R1-ICR-5 overnight, and subsequently incubated with Dox for 2 h. Cells were then treated with TNF for 30 min. The number of PLA speckles/cell was quantified (~253 cells per condition). Scale bar = 20 μm.

(E) Colocalization of TRADD and RIPK3 using confocal microscopy. $L929^{Dox\text{-}Flag\text{-}TRADD}$ cells were treated with DMSO or R1-ICR-5 overnight, followed by 2 h induction of TRADD (Dox) in the presence of E. Subsequently, cells were treated with TNF.

(F) Binding assay in *Ripk1*$^{-/-}$ 293T cells. The indicated HA-tagged proteins or FLAG-mTRADD were co-expressed in *Ripk1*$^{-/-}$ 293T cells. Lysates were subject to anti-HA immunoprecipitation, and interaction with individual HA-tagged proteins and FLAG-mTRADD was assessed by western blot.

(G,H) *In vitro* binding assay. The interaction of recombinant FLAG-mTRADD and purified mRIPK3 was assessed by (G) anti-FLAG or (H) anti-RIPK3 IP, after co-incubation *in vitro*. Immunocomplexes were analysed by western blot.

(I) Purified FLAG-mTRADD used in (G,H) was subject to size-exclusion chromatography and analysed by western blot.

(J) Confocal microscopy of TRADD fibrils. $L929^{Dox\text{-}FLAG\text{-}TRADD}$ cells were transfected with NT or *Ripk1* oligos and cells left for 48 h. Subsequently, cells were treated with DMSO or R1-ICR-5 overnight, before TRADD was induced (Dox) for 1 h Dox. Cells were then stimulated with TNF for the indicated time point. Data are technical replicates and are representative of two independent experiments.

(K) Quantification of (J). The average TRADD aggregate area/well was quantified (~200 cells/condition).

(L) Western blot analysis confirming the Dox-induced expression of the indicated RIPK1 transgenes.

(M) Evaluation of the TNFR1 signaling complex I, in reconstituted L929 *Tradd*$^{-/-}$ cells, reconstituted with various *Tradd* transgenes. Cells were incubated with DMSO or R1-ICR-5 overnight, before Dox-induced expression (2 h) of the indicated *Tradd* transgenes (see Fig 4i): 1) *WT*, 2) *DD-only*, 3) *Y16A/F18A* (TRAF-binding mutant), 4) *C293S* and 5) *Call>S*. Cells were treated with or without 2xSTREP-TNF and immunocomplexes were analysed by western blot.

Data show mean ± SD and are representative of ≥2 independent biological repeats. *P* values were calculated using (A-C,K) two-way ANOVA (Sidak's multiple comparison test) or (D) one-way ANOVA (Bonferroni's multiple comparison test).

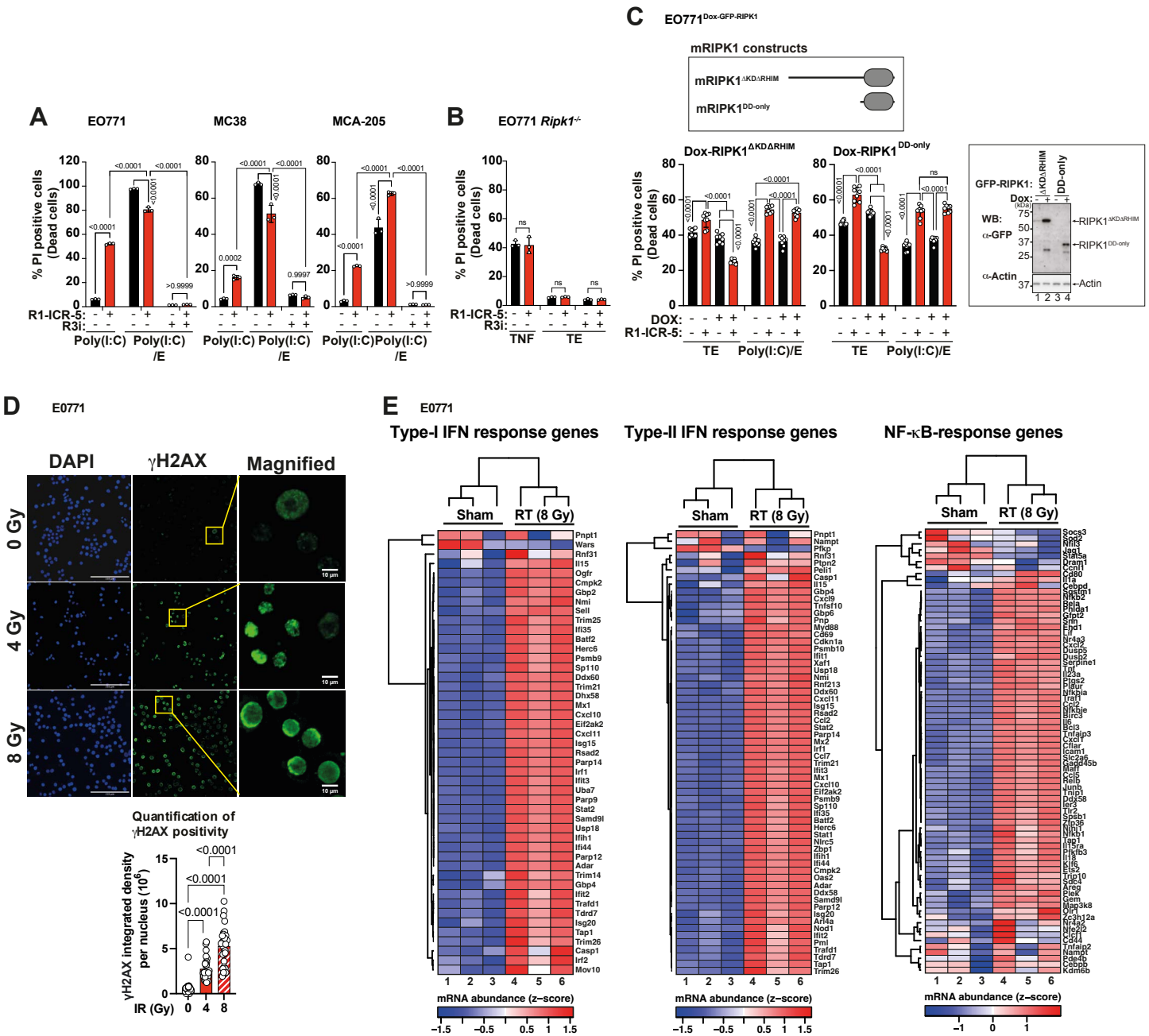

Suppl. Figure S5

Suppl Fig S5. RIPK1 dampens innate immunity in cancer

(A) Quantification of PI^+ cancer cells. Cells were pre-treated with DMSO or R1-ICR-5 for 4 h, before treatment with the indicated reagents (EO771, 24 h; MCA-205/MC38, 48 h).

(B) Quantification of PI^+ of the RIPK1 deficient EO771 cancer cells. Cells were pre-treated with DMSO or R1-ICR-5, before treatment as indicated, for 20 h.

(C) Quantification of PI^+ EO771 cells stably expression Dox-regulatable GFP-RIPK1 transgenes. Cells were co-treated with Dox and DMSO or R1-ICR-5 for 4 h, before treatment as indicated (4.5 h). Expression of the indicated RIPK1 constructs was validated by western blot analysis (6 h Dox).

(D) Irradiation (IR)-induced γ-H2AX in EO771 cells. Representative confocal images following exposure to a single fraction IR (0, 4 or 8 Gy). DNA damage was detected by IF (gH2AX integrated density/nuclei). Scale bars (150 µm).

(E) Heat maps showing relative mRNA expression of IFNα-(left), IFNγ-(middle) and NFκB-(right) responsive genes (Bulk RNA-seq). mRNA abundance z-scores are shown.

(F,G) Exposure to irradiation (8 Gy) induces IFN and NF-κB responsive genes in a TRIF-dependent manner in the indicated cell types. (F) Cells were irradiated in the presence of Dox.

(H) Quantification of PI^+ cells, stably expressing the indicated Dox-inducible shRNA constructs. Cells were irradiated and treated with Dox to induce the respective transgenes.

Data show mean ± SD and are representative of $\geq$2 independent biological repeats. *P* values were calculated using (A-C,G,H) two-way ANOVA (Sidak's multiple comparison test), (D) one-way ANOVA (Bonferroni multiple comparison test) and (F) unpaired T-test.

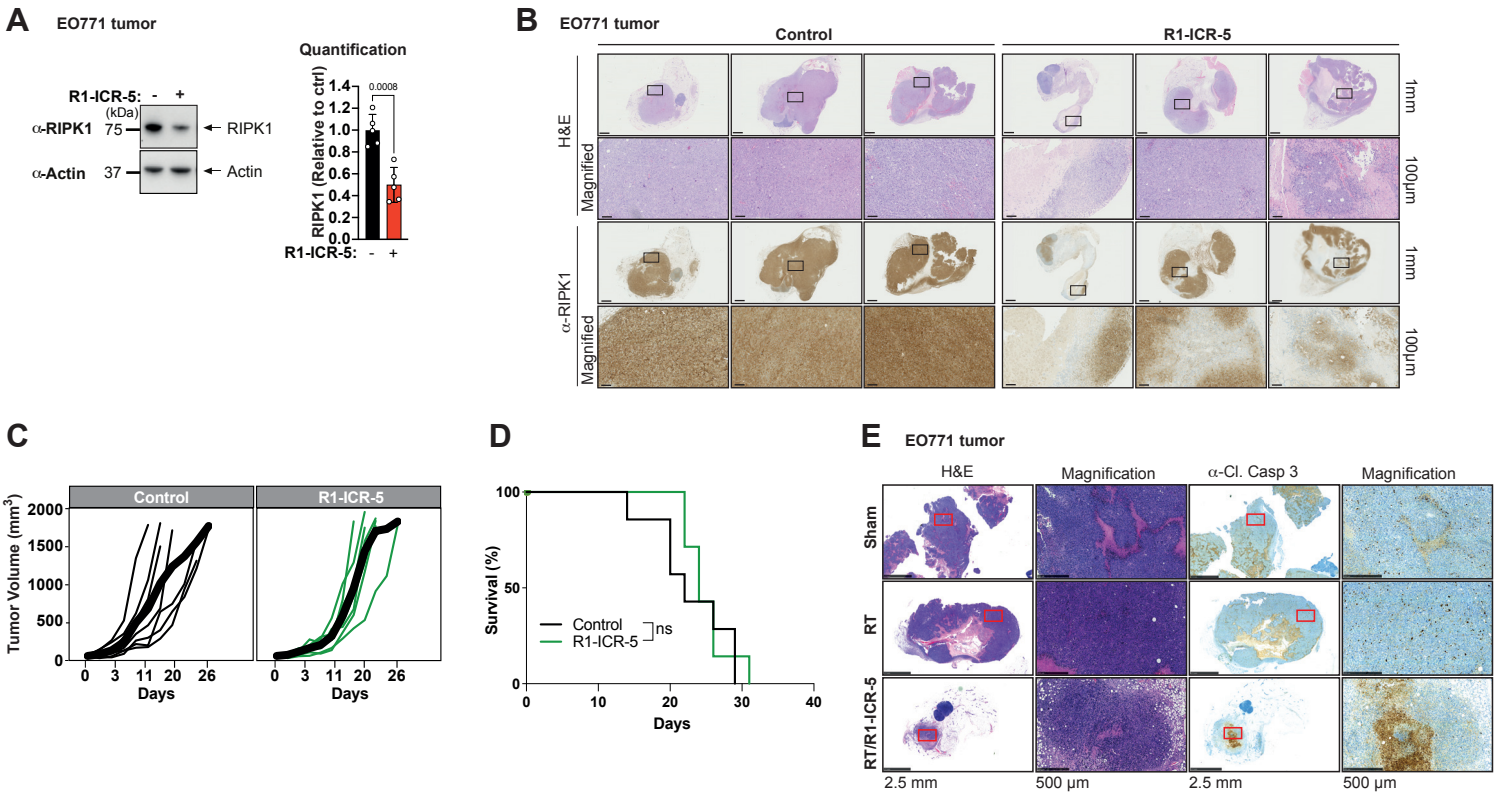

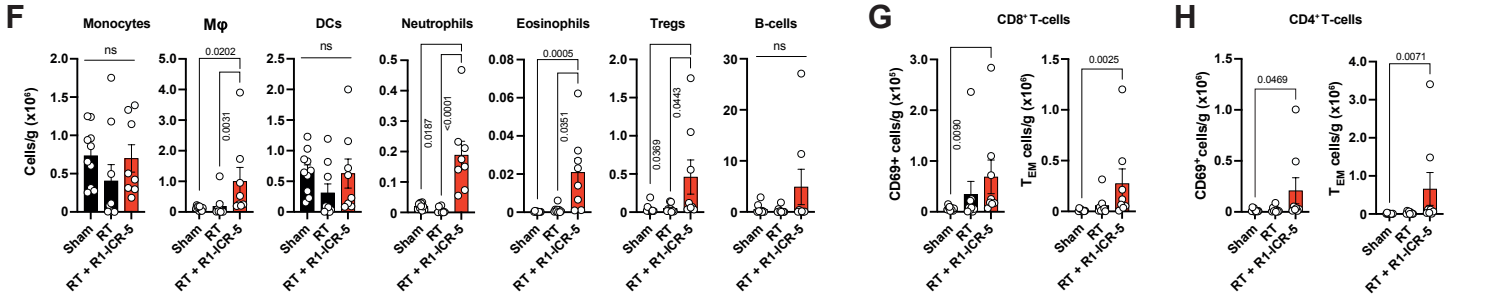

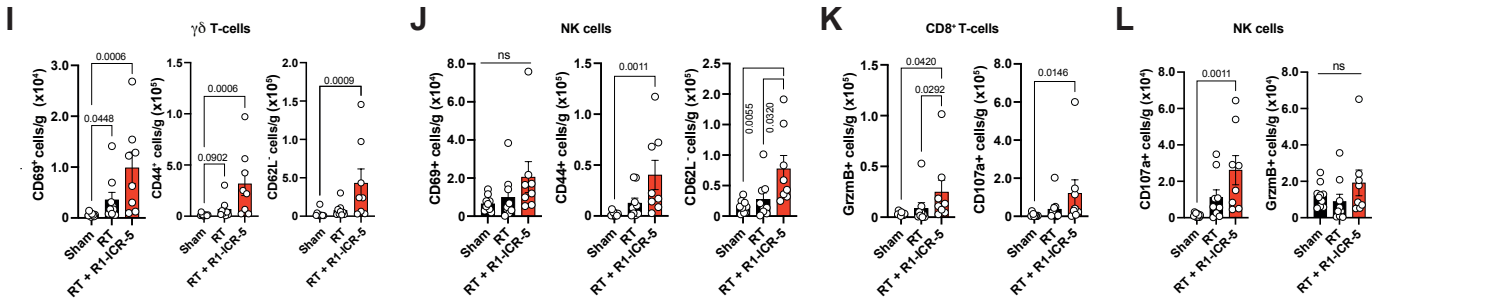

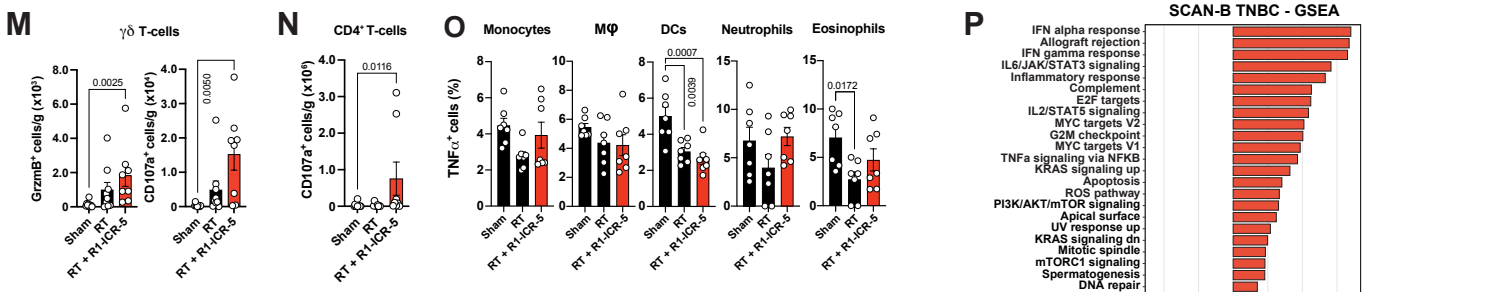

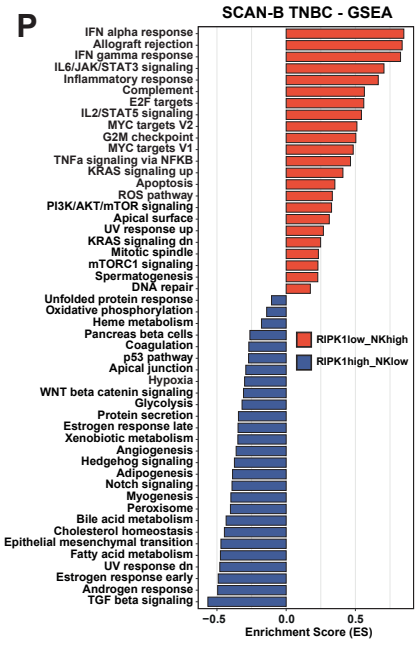

Suppl. Figure S6

Suppl Fig S6. RIPK1 dampens the immunostimulatory effects of RT

(A) Representative image of western blot (left) from a tumor of a tumor-bearing mouse, harvested 24 h after intra-tumoral injection of vehicle control or R1-ICR-5. Quantification of RIPK1 levels (right) relative to control (n=5 tumors per group).

(B) Representative images of H&E and RIPK1 staining of EO771 tumors, injected with vehicle control or R1-ICR-5 once every two days, for a total of four injections. 24h after the last injection, tumors were fixed and analyzed. (n=3 tumors per group).

(C) Tumor growth curves of EO771 tumor-bearing mice, treated with RIPK1 PROTAC (see treatment regimen in Fig 6A). Curves are representative of one biological replicate. Treated mice: IgG (n=7) and R1-ICR-5 (n=7).

(D) Survival curves of EO771 tumor bearing mice, treated in (c).

(E) Representative images of H&E and cleaved Casp3 (clCasp3) staining of EO771 tumors (see treatment regimen in Fig 6A). Treated tumors were harvested on d13 post-RT and fixed before analysis. (n=3 tumors per group).

(F-N) Flow cytometry analysis of E0771 tumors, treated as in (see Fig. 6a-g), and harvested at d13. All plots represent the number of indicated cell populations per gram of treated tumors. (F) Total number of indicated cell types, (G-J) number of $CD69^+$, $CD44^+$, $CD62L^-$ or $CD44^+CD62L^-$ (T-effector memory, T_{EM}) lymphocytes, (K-N) number of $GrzmB^+$ or $CD107a^+$ lymphocytes. Data are representative of two independent experiments.

(O) Proportion of $TNF\alpha^+$ cells across different myeloid populations in the tumor. Mice were treated as in (F), with an additional I.T. injection of R1-ICR-5 on d10.

(P) MSigDB Hallmark Gene set collection identified by GSEA to be differentially expressed in the RNAseq data from SCAN-B Triple-negative Breast Cancer (TNBC) patients categorized as RIPK1-low, NK-high versus RIPK1-high, NK-low. FDR, False discovery rate *q*-value; NES, Normalized enrichment score.

Data show mean ± SD. *P* values were calculated using (A) one-way ANOVA (Bonferroni's multiple comparison test), (C) Logrank (Mantel-Cox) and (F-O) Kruskal Wallis test.

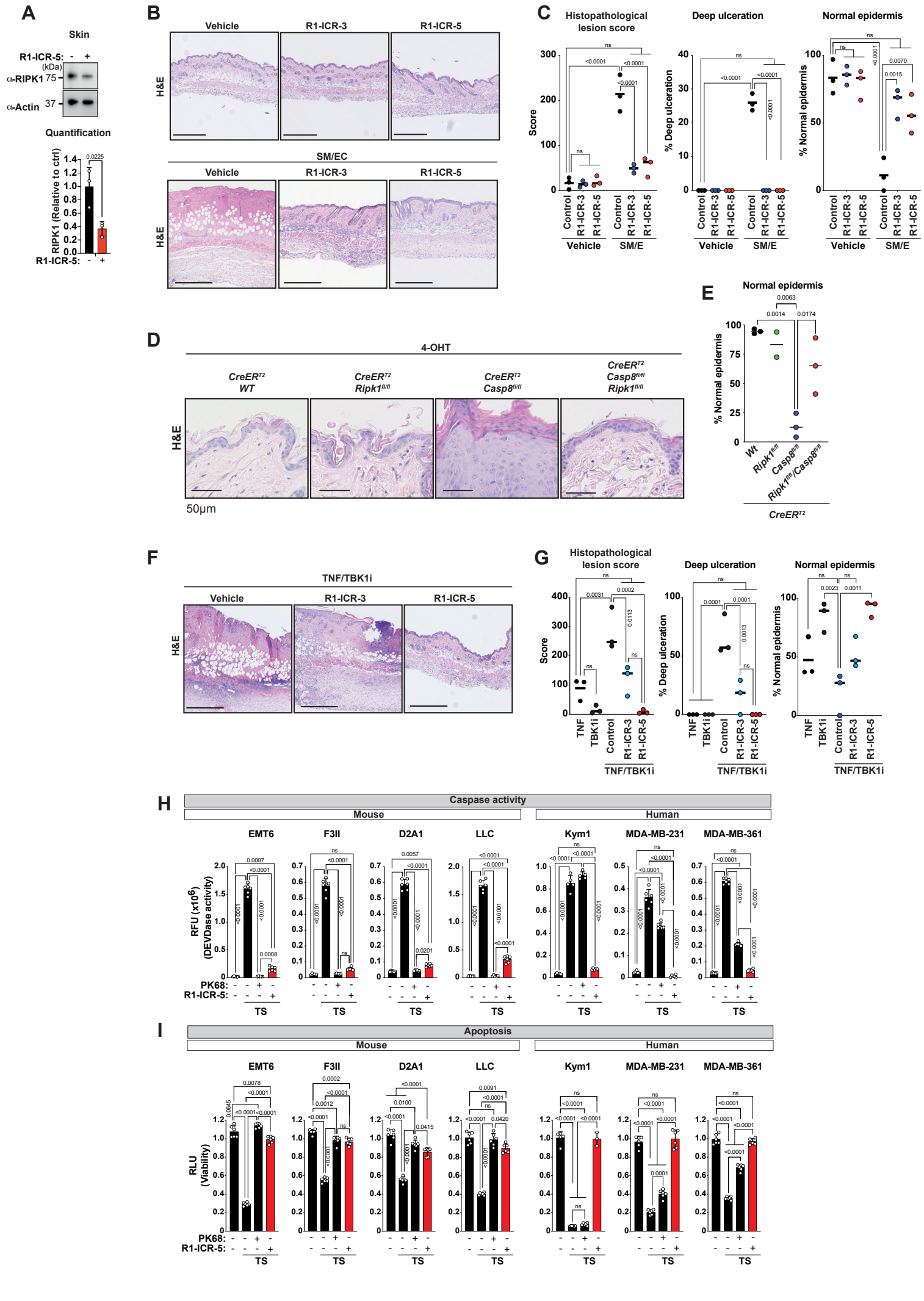

Suppl. Figure S7

Suppl Fig S7. PROTAC-mediated depletion of RIPK1 suppresses RIPK1-driven skin inflammation

(A) Representative image of western blot analysis (left) of skin extract from mice, 24h after sub-cutaneous injection with vehicle control or R1-ICR-5. Quantification of RIPK1 levels (right) relative to control (n=3 per group).

(B) Representative images of skin and H&E staining of skin sections, from mice 72 h after sub-cutaneous injection with vehicle control, R1-ICR-3 or R1-ICR-5, alone or in combination with SMAC mimetic (SM) and Emricasan (E) (n=3 per group). Scale bars 250 μm.

(C) A final histopathological multivariate lesion score (HLS) of mice treated as described in (B). (n=3 per group).

(D) Representative image of skin and H&E staining of skin sections from CreER^{T2} WT (n=3), CreER^{T2} *Ripk1*$^{fl/fl}$ (n=2), *CreER*^{T2}*Casp8*$^{fl/fl}$ (n=3), and *CreER*^{T2}*Ripk1*$^{fl/fl}$, *Casp8*$^{fl/fl}$ (n=3), treated topically with 4-OHT twice with three days interval, and analysed 20 days later.

(E) A final HLS of mice treated as described in (d).

(F) Representative images and H&E staining of skin lesions from mice, 72 h after sub-cutaneous injection with TNF and TBK1i (MRT67307) or vehicle control, in combination with R1-ICR-3 or R1-ICR-5. Scale bars 250 μm. (n=3 per group).

(G) A final HLS of mice treated as described in (f). (n=3 per group).

(H) Caspase activity assay of the indicated cell lines. Cells were treated with TNF and SM in the presence or absence of RIPK1 inhibitor (PK68) or R1-ICR-5. Caspase activity was assayed with Ac-DEVD-AMC.

(I) Viability assay of the indicated cells lines, treated as in (H). Viability was measured using CTG viability assay.

Data show mean ± SD and are representative of two independent biological repeats. *P* values were calculated using (A,C,E,G-I) one-way ANOVA (Bonferroni ‘s multiple comparison test).

Gene	DMSO			R1-ICR-5			DMSO/Poly(I:C)			R1-ICR-5/Poly(I:C)		
Tnf	1.098254	1.003857	0.897889	1.052586	1.035509	1.078397	1.696067	1.861885	2.080208	1.937306	1.995858	1.877158
Ccl2	0.859751	1.039683	1.100566	1.072019	1.04391	1.125151	1.478839	1.371644	1.584851	1.464427	1.659208	1.315584
Cxcl10	1.078556	1.019875	0.901569	0.832727	0.848472	0.783294	1.685744	1.622606	1.24873	1.425515	1.393841	1.403266
Ifnb	0.928169	1.140741	0.931089	0.895586	1.084202	1.183682	1.874823	2.310956	1.861437	1.962381	1.976274	2.179393

Supplementary Table S1. Assessing the impact of *Ripk1*-KO on TLR3 signalling (EO771 *Ripk1*$^{-/-}$). Relative mRNA expression (fold-induction) of NF-κB or IFN target genes, with respect to DMSO-treated samples. EO771 (*Ripk1*$^{-/-}$) were pre-treated with DMSO and R1-ICR-5 for 4 h, followed by 4 h treatment with Poly(I:C) (10ug/mL). All comparisons were non-significant (One-way ANOVA with Bonferroni's test for multiple comparisons). Data show ±SD and are representative of 3 independent experiments.

TNF (h)	DMSO			R1-ICR-5		
0	1	1	1	1.264407	1.196707	1.200389
2	0.633846	1.401334	1.597694	1.793844	1.111126	1.868752
4	1.501239	1.57555	2.123387	1.521671	1.949893	1.219987
6	0.992573	1.081018	1.381006	1.441785	1.214866	2.065303
0	1	1	1	1.204018	1.029739	1.127887
2	1.267564	1.414627	1.31961	1.640126	1.513743	1.724681
4	1.482537	1.432935	1.42413	1.124329	1.238473	1.214596
6	1.439029	1.315062	1.386467	1.395631	1.23063	1.199107
0	1	1	1	1.09209	0.877207	1.092765
2	0.876036	0.781752	0.853683	1.20192	1.242927	1.269845
4	1.231437	1.242337	1.255399	1.124381	1.047295	1.320433
6	0.873732	0.898656	0.962436	1.244443	1.203456	1.21589
0	1	1	1	2.243683	2.663073	2.85554
2	**9.131134**	**8.529802**	**9.212474**	**11.640793**	**11.595726**	**11.972024**
4	**5.553227**	**6.373558**	**5.412436**	**2.996883**	**2.906638**	**2.876145**
6	5.89181	5.824122	5.964438	5.518107	5.39517	5.396725

Supplementary Table S2. Assessing the impact of *Ripk1*-KO on TNF-induced signalling (EO771 *Ripk1*$^{-/-}$). Relative mRNA expression (Fold-induction) of NF-κB or MAPK target genes, with respect to DMSO-treated samples (0 h). EO771 (*Ripk1*$^{-/-}$) were pre-treated with DMSO and R1-ICR-5 (1 uM) for 4 h, followed by 0, 2, 4 or 6 h treatment with mTNF (10ng/mL). **Row 1-4, (*Il6* mRNA); 5-8, (*Tnf* mRNA); 9-12, (*Sod2* mRNA); 13-16, (A20/*Tnfaip3* mRNA).** Significant comparisons are **highlighted in bold** (Two-way ANOVA with Sidak's test for multiple comparisons). Data show ±SD and are representative of 2 independent experiments.

Supplementary Table S3: Oligonucleotides, siRNA and RT-qPCR used in this study (All reagents were used for mouse). Further information available from the lead contact, upon request.

Taqman probes (RT-qPCR)		
Reagent or resource	**Source**	**Identifier**
Actb (Mm00607939_s1)	Thermo Fisher	Cat#4331182
Cxcl9 (Mm00434946_m1)	Thermo Fisher	Cat#4331182
Cxcl10 (Mm00445235_m1)	Thermo Fisher	Cat#4331182
Ifnb1 (Mm00439546_s1)	Thermo Fisher	Cat#4331182
Tnf (Mm00443258_m1)	Thermo Fisher	Cat#4331182
Ccl2 (Mm00441242_m1)	Thermo Fisher	Cat#4331182
Il6 (Mm01210732_g1)	Thermo Fisher	Cat#4331182
A20 (Tnfaip3, Mm00437121_m)	Thermo Fisher	Cat#4331182
Oligos for PCR		
Reagent or resource	**Source**	**Identifier**
pTYB1-mTRADD forward	Invitrogen	GATATACATATGGACTACAAGGACGACGACGACAAGGGCG
pTYB1-mTRADD reverse	Invitrogen	CTCGAGGAATTCGGCCAGGCCGCCATCCGGC
pT7CFE-mRIPK3 forward	Invitrogen	GATGATAATATGGCCACCACCCATATGTCTTCTGTCAAGTTA
pT7CFE- mRIPK3 reverse	Invitrogen	TTTTTTTTTTTTTTTTTTTTTCTACTTGTGGAAGGGCTGCCA
hRIPK1ΔRHIMΔDD 1st/2nd PCR forward	Invitrogen	ACCGGTACCATGCAACCAGACATGTCCTTG
hRIPK1ΔRHIMΔDD 1st PCR reverse	Invitrogen	CAGCCGCTCACGCTGCCTATAGATTCATCTGTTGGTGGCAA
hRIPK1ΔRHIMΔDD 2nd PCR reverse	Invitrogen	CTCGAGCTAGCTGATCTTCTTGAACAGTCTCCAGCCGCTCACGCTGCC
Oligos for CRISPR		
Reagent or resource	**Source**	**Identifier**
pLC-EGFP-*mTradd* gRNA forward	Invitrogen	CACCG**CGCAACTGGACGATGAGCTG**
pLC-EGFP-*mTradd* gRNA reverse	Invitrogen	AAAC**CAGCTCATCGTCCAGTTGCG**C
pLC-EGFP-*mTnfr1* gRNA forward	Invitrogen	caccgCGGACAGTCACTCACCAAGT
pLC-EGFP- *mTnfr1* gRNA reverse	Invitrogen	aaacACTTGGTGAGTGACTGTCCGc
pLC-EGFP-*mMlkl* gRNA forward	Invitrogen	caccgCTGGCAGCAGGAAGATCGAC
pLC-EGFP- *mMlkl* gRNA reverse	Invitrogen	aaacGTCGATCTTCCTGCTGCCAGc
pLC-EGFP-*mRipk1* gRNA forward	Invitrogen	caccgAGGGAACTATTCGCTGGTGA
pLC-EGFP- *mRipk1* gRNA reverse	Invitrogen	aaacTCACCAGCGAATAGTTCCCTc
pMA-h*Ripk1* gRNA	Invitrogen (Synthetic)	GCTCGGGCGCCATGTAGTAG
siRNAs		
Reagent or resource	**Source**	**Identifier**

siRNA Control 1 (SCR1) AllStars Neg Control	Qiagen	1027281
siRNA Control 2 (SCR2) On target plus Non-targeting siRNA-1	Dharmacon (On target plus)	D-001810-01-05
siRNA *Mlkl*	Dharmacon (On target plus SMART pool)	L-061420-00-0005
siRNA *Traf1*	Qiagen Flexitube GeneSolution	GS22029
siRNA *Traf2*	Qiagen Flexitube GeneSolution	GS22030
siRNA *Traf3*	Qiagen Flexitube GeneSolution	GS22031
siRNA *Cyld*	Qiagen Flexitube GeneSolution	GS74256
siRNA *Tradd*	Qiagen Flexitube GeneSolution	GS71609
siRNA *Fadd*	Dharmacon (On target plus SMART pool)	L-040488-00-0005
siRNA *Ripk3*	Dharmacon (On target plus SMART pool)	L-049919-00-0005
siRNA *Trif (Ticam1)*	Dharmacon (On target plus SMART pool)	L-055987-00-0005
siRNA *Mavs*	Qiagen Flexitube GeneSolution	GS228607
siRNA *Pkr*	Qiagen Flexitube GeneSolution	GS19106
siRNA *Ticam2*	Qiagen Flexitube GeneSolution	GS225471
siRNA *Mk2*	Qiagen Flexitube GeneSolution	GS17164
siRNA *Rig-i*	Dharmacon (On target plus SMART pool)	L-065328-00-0005
siRNA *Mda5*	Qiagen Flexitube GeneSolution	GS71586
siRNA *Ripk1*	Qiagen Flexitube GeneSolution	GS19766
siRAN *Rela*	Dharmacon (On target plus SMART pool)	L-040776-00-0005
siRNA *Hoip* (*Rnf31*)	Dharmacon (On target plus SMART pool)	L-055122-01-0005
siRNA *Tak1*	Dharmacon (On target plus SMART pool)	L-040718-00-0005
siRNA *Tbk1*	Qiagen Flexitube GeneSolution	GS56480
siRNA *A20 (Tnfaip3)*	Dharmacon (On target plus SMART pool)	L-058907-02-0005
siRNA *Nemo (Ikbkg)*	Dharmacon (On target plus SMART pool)	L-040796-00-0005

Suppl. Data S1. **Flow cytometry gating strategy:** Gating strategy used for flow cytometric analyses. 1) NK cells, 2) B-cells, 3) $CD8^+$ T-cells, 4) $CD4^+$cv T-cells, 5) Regulatory T-cells, 6) γδ T-cells, 7) NK T-cells, 8) Dendritic cells, 9) Monocytes, 10) Neutrophils, 11) Macrophages and 12) Eosinophils.

Population #	Immune population
1	NK cells
2	B cells
3	$CD8^+$ T-cells
4	$CD4^+_{cv}$ T-cells
5	T-reg cells
6	γδ T-cells
7	NK T-cells
8	Dendritic cells (DCs)
9	Monocytes
10	Neutrophils
11	Macrophages
12	Eosinophils

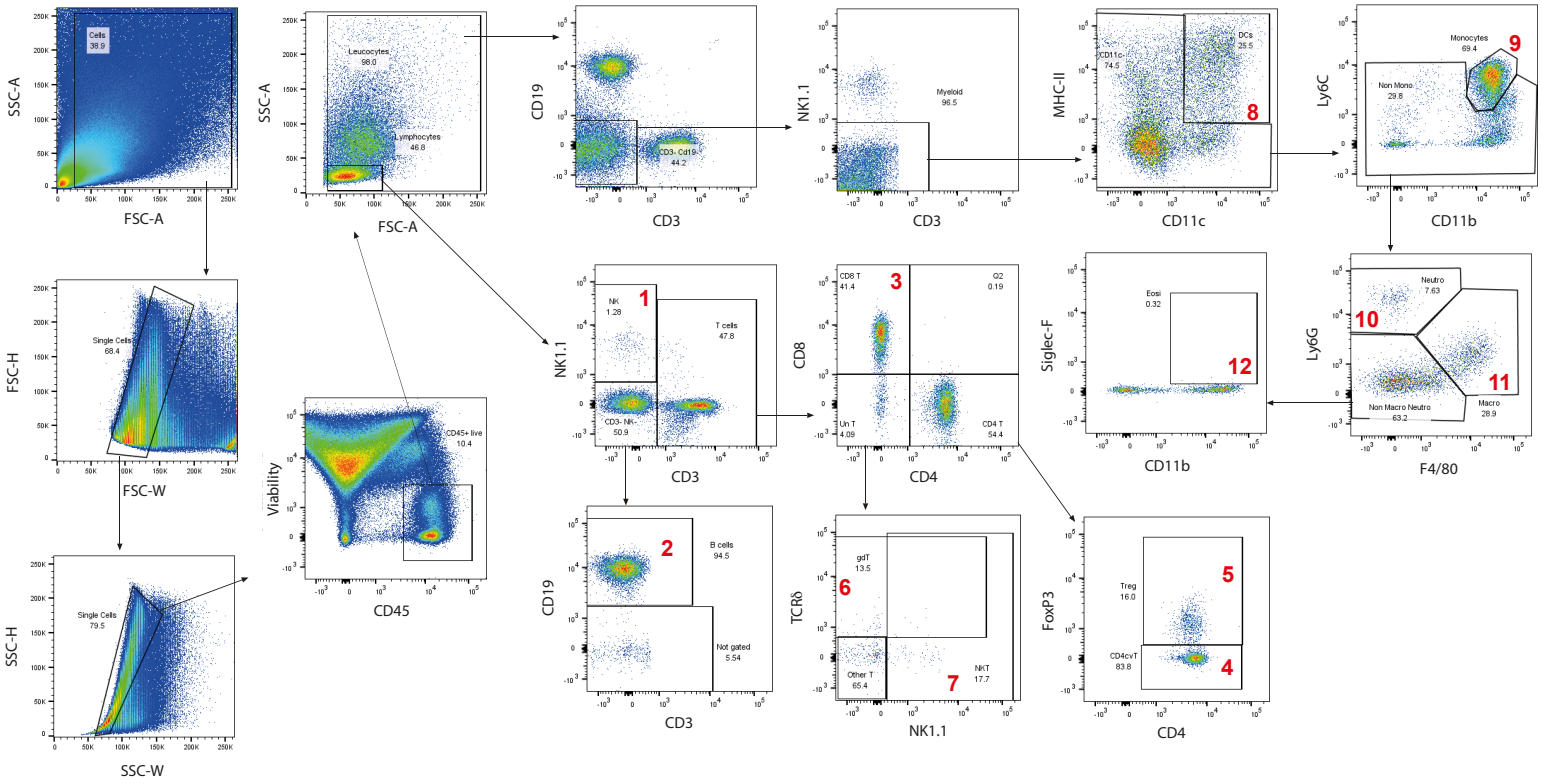

Suppl. Data S1